Investigation of the response of a CALIFA demonstrator and development of an APD test stand

Charakterisierung des CALIFA-Demonstrators und Entwicklung eines APD Teststandes
Zur Erlangung des Grades eines Doktors der Naturwissenschaften (Dr. rer. nat.)
genehmigte Dissertation von Han-Bum Rhee aus Seoul (Südkorea)
2018 — Darmstadt — D 17

1. Gutachten: Prof. Dr. Thorsten Kröll
2. Gutachten: Prof. Dr. Joachim Enders

TECHNISCHE
UNIVERSITÄT
DARMSTADT

Fachbereich Physik
Institut für Kernphysik
AG Kröll

Investigation of the response of a CALIFA demonstrator and development of an APD test stand
Charakterisierung des CALIFA-Demonstrators und Entwicklung eines APD Teststandes

Genehmigte Dissertation von Han-Bum Rhee aus Seoul (Südkorea)

1. Gutachten: Prof. Dr. Thorsten Kröll
2. Gutachten: Prof. Dr. Joachim Enders

Tag der Einreichung: 17.Mai.2018
Tag der Prüfung: 18.June.2018

Darmstadt — D 17

Bitte zitieren Sie dieses Dokument als:
URN: urn:nbn:de:tuda-tuprints-87088
URL: http://tuprints.ulb.tu-darmstadt.de/8708

Dieses Dokument wird bereitgestellt von tuprints,
E-Publishing-Service der TU Darmstadt
http://tuprints.ulb.tu-darmstadt.de
tuprints@ulb.tu-darmstadt.de

Die Veröffentlichung steht unter folgender Creative Commons Lizenz:
Namensnennung – Keine kommerzielle Nutzung – Keine Bearbeitung 4.0 International
http://creativecommons.org/licenses/by-nc-nd/4.0

Erklärung zur Dissertation

Hiermit versichere ich, die vorliegende Dissertation ohne Hilfe Dritter nur mit den angegebenen Quellen und Hilfsmitteln angefertigt zu haben. Alle Stellen, die aus Quellen entnommen wurden, sind als solche kenntlich gemacht. Diese Arbeit hat in gleicher oder ähnlicher Form noch keiner Prüfungsbehörde vorgelegen.

Darmstadt, den 17.Mai.2018

(H.Rhee)

Abstract

The R^3B experiment is a part of the future FAIR project at GSI. It will be used to study reactions with relativistic radioactive beams (R^3B). The setup will be placed in the high-energy branch of the Super-FRS. It aims to cover various physics programs. The CALIFA is a spectrometer and a calorimeter. It will surround the central target and detect high-energetic γ-rays and light charged particles. The CALIFA group made a DEMONSTRATOR to do a systematic study before a mounting together a complete detection system. It is a first step of the set-up and has been used at the first experiment in CAVE C of GSI. The main parts of the DEMONSTRATOR are called PETAL, which is a group of 64 crystals in a holding carbon fiber structure.

For the first part of this thesis, I have tested a PETAL in the laboratory of the institute of nuclear physics (IKP), TU Darmstadt and also gone over the analysis framework (R3BRoot) by comparing the results of previous studies [R3B11; R3B15] and my simulation. The basic properties of the detection unit, the event reconstruction and particle identification have been checked. In addition, the measurement programs have been simulated to be compared to the data. R3BRoot, which is an analysis and simulation toolkit of the R^3B experiment, was used. Several measurements were done, for which different sources were used: an AmBe source (γ-rays, fast neutrons), thermalized neutrons (high-energy γ-rays via capture process) and muons from cosmic-rays.

The second part of this thesis is devoted to the development of a quality assurance test stand for the CALIFA APDs. A part of CALIFA employs CsI(Tl) crystals coupled with APDs as a detection unit. Every single APD has to be tested before it is assembled with the CsI(Tl) crystal. I have designed and tested the Q.A. test stand for the APDs. The main idea of the test stand is to provide controlled conditions and a testing signal for the APDs and to measure the variance of the output. As a result, it will provide information to characterize the individual units. This data will be used to compensate temperature-related gain shifts during the measurement.

Zusammenfassung

Das R^3B Experiment ist ein Teil des zukünftigen FAIR Projekts an der GSI. Es wird verwendet werden, um Reaktionen mit relativistischen radioaktiven Strahlen zu untersuchen. Der Aufbau wird am Hochenergiearm des Super-FRS liegen. Das Ziel ist, es verschiedene Physikprogramme mit diesem Aufbau zu ermöglichen. Daher ist CALIFA sowohl als Spektrometer als auch als Kalorimeter konzipiert. Es wird das zentrale Target umschließen und hochenergetische Gammastrahlung und leichte geladene Teilchen detektieren. Die CALIFA-Kollaboration fertigte zunächst einen DEMONSTRATOR an, um eine systematische Untersuchung vor der Montage des kompletten Detektorsystems durchzuführen. Es ist der erste Schritt hin zum vollständigen Aufbau und wurde bereits im ersten Experiment im CAVE C der GSI verwendet. Der Hauptteil des DEMONSTRATORs trägt die Bezeichnung PETAL, und bezeichnet eine Gruppe von 64 Kristallen, welche sich in einer Karbonfaserummantelung befinden.

Als ersten Teil meiner Thesis habe ich das PETAL im Labor des IKP der TU Darmstadt getestet. Außerdem habe ich das Analyseframework (R3BRoot) dazu genutzt, die Ergebnisse aus früheren Studien [R3B11; R3B15] und meiner Simulation zu vergleichen. Die grundlegenden Eigenschaften des Detektorsystems, die Eventrekonstruktion und die Teilchenidentifikation wurden überprüft. Zusätzlich wurden die durchgeführten Messungen simuliert und mit den experimentellen Daten verglichen. Das Analyse- und Simulationstoolkit R3BRoot wurde hierzu verwendet. Mehrere Messungen wurden ausgeführt, für welche verschiedene radioaktive Quellen verwendet wurden: eine AmBe-Quelle (Gammastrahlung, schnelle Neutronen), thermische Neutronen (hochenergetische Gammastrahlung mittels Einfangsprozessen) und aus der Höhenstrahlung stammende Myonen.

Der zweite Teil dieser Arbeit bestand in der Entwicklung eines Qualitätssicherungsteststandes für die CALIFA APDs. Dies war notwendig, da ein Teil von CALIFA mit APDs gekoppelte CsI(Tl) Kristalle als Detektionseinheit verwendet. Jede einzelne APD musste getestet werden, bevor diese mit dem CsI(Tl) Kristall verbunden werden konnte. Dieser Teststand wurde von mir entworfen und getestet. Die Hauptidee des Teststandes besteht darin kontrollierbare Bedingungen und ein Testsignal für die APDs bereitzustellen und die Varianz der Ausgabe zu bestimmen. Als Ergebnis wurden so Informationen über die einzelnen Einheiten erhalten. Diese Daten werden verwendet, um temperaturabhängige Verstärkungsverschiebungen während eines Experiments ausgleichen zu können.

Contents

1 Introduction

The **F**acility for **A**ntiproton and **I**on **R**esearch (FAIR) is the future accelerator facility at the GSI [Hen+01]. FAIR will be one of the largest accelerators, with around 1000 meters circumference of the accelerator ring. Around 3000 scientists from about 50 countries will be involved in the basic research. It will produce a primary beam of an energy up to 15 A·GeV with accelerated particles ranging from proton to uranium. Various research fields can use this facility and can be grouped in four groups: APPA physics (Atomic, Plasma Physics and Applications), Nuclear Matter Physics, NUSTAR physics (Nuclear Structure, Astrophysics and Reactions) and Physics with High Energy Antiprotons. FAIR will provide some answers to the fundamental question of the evolution of the universe and the structure of matter.
The **R**eactions with **R**elativistic and **R**adioactive **B**eams (R^3B) experiment is a part of the FAIR facility and in the NUSTAR physics group [Aum+14]. It will be placed in the high-energy branch of the **Super**-conducting **FR**agment **S**eparator (Super-FRS). R^3B is a versatile and multi-purpose detection set-up. It consists of **GSI L**arge **A**cceptance **D**ipole (GLAD), **New L**arge-**A**rea **N**eutron **D**etector (NeuLAND), R^3B-Si-Tracker, **CAL**orimeter for **I**n **F**light detection of γ-rays and light charged p**A**rticles (CALIFA), and in-beam tracking detectors (Fig. 1.1).

The GLAD magnet has a high field integral of 5 Tm. NeuLAND enables the study of neutron rich systems and multi-neutron correlations. The Silicon tracker offers precise tracking and vertex reconstruction by detecting two protons in the case of quasi-free scattering. It aims to investigate a wide variety of scattering experiments from heavy-ion induced electromagnetic excitation, and knock-out reactions to light-ion (in)elastic and quasi-free scattering in inverse kinematics. Through these studies, it will provide the answer to nuclear many-body problems.
For these works, good calorimetric properties with high-resolution are required. CALIFA will have to fulfill these requirements. Quasi-free scattering (QFS) reactions [JM66] with protons have been used as an outstanding experimental tool. The reaction is described as ${}^{A}Z(p,2p)^{A\text{-}1}Z$. QFS reaction studies can be used to investigate the single particle structure in nuclei. For this reaction, the energy of the incoming particle needs to be of medium energy (between 100 MeV to 1 GeV) to knock out a bound nucleon. It is assumed that the reaction does not involve further interactions between incident and outgoing particles. So, two protons from the knockout reaction can be detected in the forward direction with an angular correlation. The opening angle of two particles is between 80° to 90° in the lab frame.

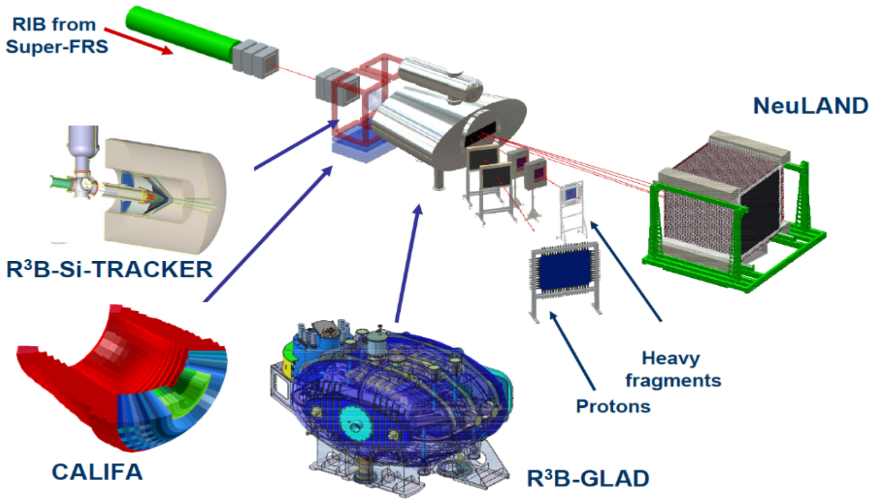

Fig. 1.1: The complete R^3B detector set-up [R3B15].

To analyse this, the momentum vector of the outgoing nucleons and γs from the de-excitation of the recoil nucleus are required. The new experiment setup (R^3B) at FAIR meets these requirements. R^3B does QFS in inverse kinematics, hence nuclei on protons. The γs will be emitted by beamlike nucleus. For the study of QFS high-energy light charged particles with prompt γ-ray de-excitation of the residual fragment need to be detected. The capability of the particle identification and the distinction of γ-ray cascades are a key part of the CALIFA. Another example are knockout reactions, such as (p,np) reactions. They usually use light nuclei targets with a heavy nuclei beam. In this case not only protons and neutrons need to be detected, but also γ-rays from the de-excitation of the fragment. For the case of Coulomb excitation, γ-spectroscopy is used to determine (n,γ) and (p,γ) cross sections.
As first objective of this work, CALIFA's capabilities are checked through several programs in the laboratory in TU Darmstadt. The highly segmented structure of the detector will cause that γ-rays deposit their energy in more than one crystal. Moreover, in the high multiplicity events, each γ-ray has to be reconstructed separately. For this, a reconstruction algorithm is required. This will be tested using high-energy γ-rays. Also, (n,X) reactions occur in the measurement caused by fast neutrons. They can be used to check the capability of the detector to identify particles.

The CALIFA barrel consists of CsI(Tl) crystals, which are individually read out with APDs. The second objective of this work is the development of a quality assurance test stand for the APDs. A part of CALIFA, the demonstrator consisting of petals with 64 crystals each, is under construction. The single detection units have to be checked and characterized. For the APDs, a dedicated test stand was designed and used to characterize 155 APDs.

2 CALIFA

In this chapter information on CALIFA is given. At the beginning, an overview over CALIFA is presented. Later, the main components of the electronics of CALIFA are discussed. Also, R3BRoot, which is the analysis and simulation tool for the R3B experiment, is explained.

2.1 CALIFA

The CALIFA is the calorimeter and the spectrometer of R^3B. It surrounds the R^3B reaction target and will be a key part in the R^3B experiment. It will surround a central target and aims to detect a wide energetic range of γ-rays (100 keV < E_γ < 30 MeV) and light charged particles up to 700 AMeV. These particles and γ-rays are therefore Lorentz boosted. The γ-rays are Doppler shifted Doppler broadening includes the opening angle. So, CALIFA will be highly segmented with a optimized angular aperture and length of crystals corresponding to each polar angle region.

Geometry

CALIFA consists of two sections, which are divided by their angular range; a 'Forward EndCap' covering from the beam pipe limit to 43° [R3B15] and a cylindrical 'Barrel' covering an angular range from 43.2 to 140.3° [R3B11]. The CALIFA barrel employs CsI(Tl) crystals coupled with Avalanche Photo Diodes (APD) as detecting units. The design consists of 1952 detecting units. The structure of the CALIFA barrel provides the angular resolution necessary to overcome limitations imposed by the Doppler broadening at high beam energies approaching 1 AGeV.

The Endcap divided into iPhos and CEPA Phoswiches. The iPhos sector inherits the same detection units as the Barrel and will cover the polar angle range from 19° to 43°. The part of CALIFA at the most forward angles is based on the phoswich concept, which is called CEPA. It consists of 7 cm $LaBr_3$ coupled with 8 cm $LaCl_3$ crystals. Photo tubes with special metal package (Hamamatsu R7600U-200) have been chosen as a readout device. The CEPA will cover the polar angle range from 7° to 18°.

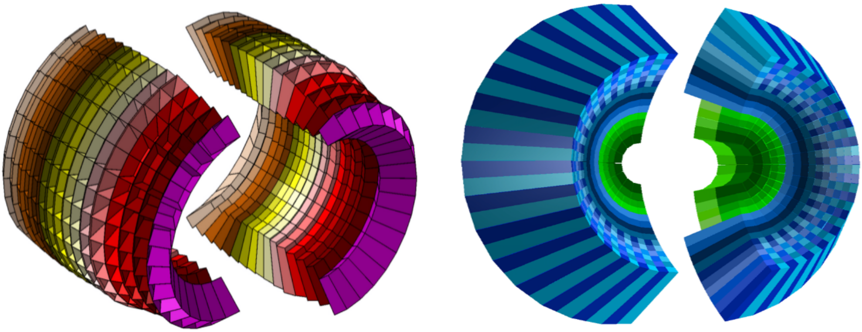

Fig. 2.1: Schematic view of the CALIFA barrel (left) [R3B11] and endcap (right) [R3B15]. The endcap is divided into iPhos and CEPA Phoswiches.

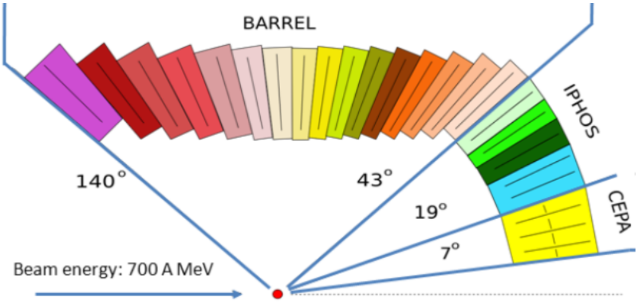

Fig. 2.2: Schematic representation of the CALIFA detector profile [R3B11].

Multi-purpose detector

The variety of physics programs of the R^3B experiment demands CALIFA to be a versatile detector array. Among its functions, it will be used as:

- high-resolution spectrometer
- γ-ray calorimeter

High-resolution spectrometer: As a high-resolution spectrometer it aims to detect γ-rays from relatively low energy up to several MeV with low multiplicity (2-3). In this case, the energy resolution will be required to be $\Delta E/E < 6$ % for 1 MeV γ-rays to distinguish γ-ray cascades coming from the de-excitation of light exotic nuclei. Knock-out reactions or (p,2p) reaction with light, radioactive beams are a typical physics example.

γ-ray calorimeter: In this case CALIFA is required to detect γ-rays with energies up to 10 MeV. It is associated to very fragmented decays, such as high-multiplicity events. The total γ-rays absorption, γ-ray sum energy and γ-ray multiplicity will arise as key parameters. The energy resolution of each unit will be a less significant parameter. Typical physics are reactions with pygmy- or giant- resonance decay.

The most challenging task of CALIFA is providing good calorimetric properties with high-resolution to study reactions, such as quasi-free scattering (i.e (p,2p),(p,pn)...). In this case, high-energy light charged particles have to be detected with prompt γ-ray de-excitation of the residual fragment. These processes will be measured with a good energy resolution over a huge dynamic range.

2.2 Detection unit of the CALIFA barrel

2.2.1 CsI(Tl)

The main concept of the CALIFA barrel is to provide a granular structure to ensure the reduction of Doppler broadening. During the selection of a scintillation crystal, the light output, the intrinsic resolution of the material and a relatively low price have to be considered. Furthermore, the availability of larger quantities arises in the consideration. The CALIFA group has chosen CsI(Tl) as a scintillator of the barrel area. It has a high mass number and can be stored long-term without encapsulation as long as two conditions are controlled: humidity and temperature. The energy resolution of a CsI(Tl) coupled with an APD obtained with a ^{137}Cs source is 4.42 % [Gas+08]. In addition, it has two decay constants. It can be used for particle distinction between protons and γ-rays and neutrons and γ-rays (section 6.5).

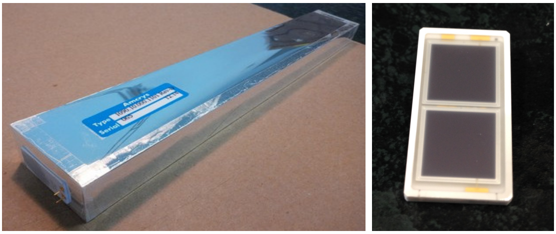

Fig. 2.3: Detection unit of CALIFA barrel: CsI(Tl) crystal wrapped with ESR film (left). Hamamatsu S12102 APD (right)

The crystals have a frustum shape and are arranged with cylindrical symmetry around the beam line. Additionally, their longitudinal axis is slightly tilted with respect to the polar angle. This leads to a reduction of empty space and an efficient use of the material within the active area, thus reducing the amount of γ-rays escaping through the space between the crystals. In case of the (p,2p) QFS reaction, the scintillator will detect protons in forward part of the CALIFA barrel. Most of the high-energy protons will hit the Endcap. In this polar angle area the proton energy is expected to be $\sim$320 MeV (polar angle: 43°). A detailed study has been done with the simulation package to decide the structure of the detection system. Thereby, the length of the crystals are calculated to 220 mm to stop the protons falling into each angle area.
When using long crystals, the light attenuation and optical focusing [Bea+94] have to be controlled. The deviation of light output for crystal relates with the distance between the interaction position and the photo-sensor. The CALIFA group has tested 100 mm length of CsI(Tl) and reported it has a initial deviation in light output, $\Delta L \leq 8\%$ [R3B11]. To improve this deviation, the crystals have an applied lapping with Al_2O_3. As a result, the longest shape of crystals for CALIFA barrel (220 mm) has a ΔL less than 8%. After lapping crystals, the additional reflecting layer is demanded to maximize the absolute light output. The Enhanced Specular Reflector (ESR) film was tested in another project [Ph.+04] and has therefore been chosen.

2.2.2 APD

The other part of the detecting units was determined through several previous related studies [R3B11]. Photomultipliers and silicon photo diodes were studied as candidates for photosensors also. Avalanche photodiodes (APDs) were chosen as photosensors for the CALIFA barrel. They meet the requirements of the CALIFA

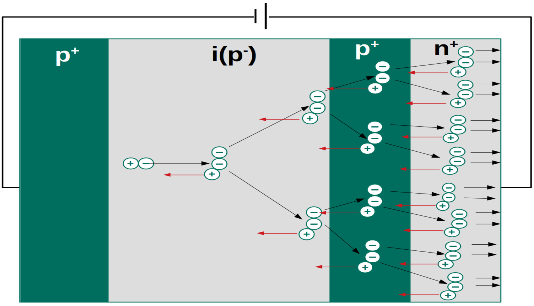

Fig. 2.4: The operational principle of the avalanche photodiode.

barrel and provide a compact geometry and insensibility to the magnetic fringe field from the GLAD. Because CALIFA will be placed next to the GLAD magnet (see Fig. 1.1). An APD provides an internal gain and can therefore give a signal which is significantly larger relative to the electronic noise. Figure 2.4 shows the operational principle of the APD [Her16]. The internal gain of an APD is due to impact ionization of lattice atoms by in the high-field section of the depletion region. Photo-generated charge carriers diffuse into avalanche region creating additional charge carriers.
The APD multiplication factor M is given by

$$M = \frac{1}{1 - \int_0^L \alpha(x) \mathrm{d}x} \tag{2.1}$$

where L is the space-charge boundary for electrons, and α is the multiplication coefficient for electrons (and holes).
APDs have a quantum efficiency of 75∼85%, internal gain of 40∼50 and linear light response in the CsI(Tl) emission spectrum.
APD gain, dark current and the electronic noise of the APD depend on temperature. This effect has been explored for APDs working at the nominal bias voltage V_{nom}. The gain-temperature dependence is displayed in Fig. 2.5.

2.3 Electronics

One branch of modern digital data acquisition is developing digital pulse shape analysis (PSA). This basic concept is also used for the R^3B DAQ system. The DAQ

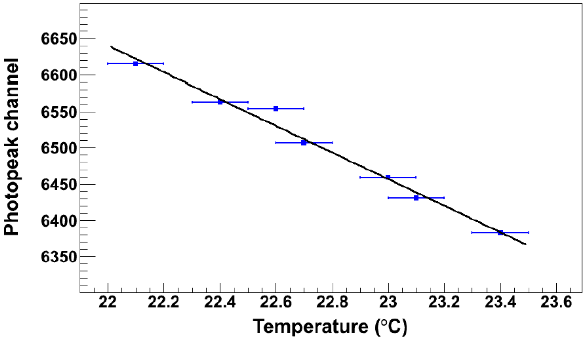

Fig. 2.5: Measured gain-temperature dependence for a Hamamatsu S8664-1010 APD [R3B11].

is based on the Multi Branch System (MBS) [Kur00] and the GOSIP protocol. This section will focus on FEBEX3b, exploder and preamplifier, which are actually used during the measurement.

FEBEX 3

The **F**ront **E**nd **B**oard with optical link **EX**tension (FEBEX 3) is a 16 channel pipeline ADC. The FEBEX board was developed in the CSEE department of GSI. It features 16 differential analog inputs, 16 differential LVDS I/Os (max. 8 outputs) and a serial multi-gigabit connections to the backplane over a PCI Express connector.
The ADC sampling rate is 50 MHz at a resolution of 14 bit. FEBEX3 contains a trigger logic, timestamp logic and an external clock input to a high precision PLL synthesizer. The board size is 100 mm × 160 mm [Rus+13]. The FEBEX boards are designed to work with globally triggered DAQ systems by accepting user defined trigger windows. The complete control and readout logic is implemented in a Lattice FPGA.
The interface, implemented in the FEBEX board, is designed to work with the MBS data acquisition system [Kur00]. Through the MBS system, via an optical interface, the user has full control over all components of FEBEX. FEBEX 3 has two data buffers, each of them takes 8000 samples (160 μs) [Kur16]. It provides a nearly dead-time free system [Mü91].

EXPLODER

The exploder is an interface between different I/O combinations (on daughter boards) and multi gigabit fiber optical links. The main and daughter boards are connected over two high speed, high density connectors. The exploder is the trigger logic box of FEBEX 3. It can provide a trigger signal for the DAQ system: either external- or internal-trigger. The external trigger mode works with an externally provided signal. The daughter boards start reading data with this signal. Whereas, the internal trigger makes a trigger signal itself. When the single channel on daughter board has a signal, which fulfills the trigger condition, the other channels on same board start reading data with this signal.

Preamplifier

The Mesytec MPRB-16 is the preamplifier of the CALIFA barrel. It is a 16 channel charge-sensitive preamplifier with an integrated bias voltage generator. The device is remotely controllable via the Mesytec control bus, which allows to adjust the 16 bias voltages individually for each channel in 100 mV steps, up to 600 V. This preamplifier can select the sensitivity range for the detecting energy range: low-sensitivity (30 pC, for high energy range) and high-sensitivity (3 pC, for low energy range). It contains one temperature sensor and can be used for temperature compensation to adjust the bias voltage to keep the gain stable. It applies one compensation value to one premaplifier. To be accurate with the temperature compensation, each APDs is required to be characterized. Mesytec provided a special edition of the MPRB-16, which has two MPRB-16 in one housing (MPRB-32).

2.4 CALIFA demonstrator

The CALIFA demonstrator was built to serve as a reference for systematic studies of its elements and structures. It is based on a collection of grouped crystals, so called 'PETALs', with a geometry and dimensions corresponding to the furthest forward elements of the BARREL. One PETAL is made of 16 Carbon Fiber (CF) structures, which is the envelope for 4 crystals, with 2 (azimuthal) × 8 (polar) alveoli. It can contain up to 64 crystals. The PETAL has additionally a box-envelope, necessary to isolate the unit and to hold the alveoli. Fig. 2.6 shows the design of a PETAL assembly. The CF-structure is held at the upper-inner part of the walls by the same piece with flaps as for CALIFA; and along the outer sides with panel-like pieces (semi-transparent in the drawing) which make an envelope of the PETAL. The overall dimensions of the PETAL are about 59 cm (length) × 27 cm (width) × 37 cm (height) [Cas+14]. One PETAL is connected to two MPRB-32 preamplifiers and subsequently 4 FEBEX boards, which have 16 channels each. The CALIFA PETALs

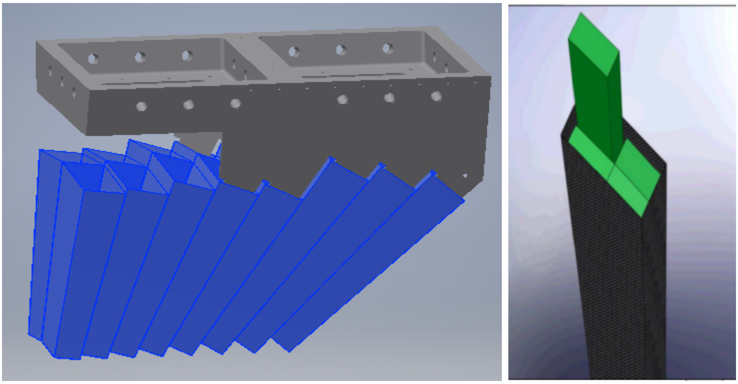

Fig. 2.6: Design of a PETAL assembly. The PETAL has 2 × 8 alveoli, which are made of carbon fiber, and are accommodated in an aluminum box. Right: Schematic view of an alveolus including 4 crystals.

were already used for in beam experiments at the Bronowice Cyclotron Centre (CCB) in Krakow, Poland [Pie+16], Lisbon, Portugal and GSI.

2.5 R3BRoot

R3BRoot [Ber11] is the simulation and analysis framework for the R^3B experiment. It is based on the FairRoot [Ber+08] base library which is common to many experiments at FAIR. The FairRoot base library provides

- a common data structure for simulation and analysis based on Root Trees,
- a common geometry description based on the Root Geometry Modeler,
- an interface to different Monte Carlo engines using the Root Virtual Monte Carlo package [Bru+03],
- Detector base class handling initialization, geometry construction, hit processing (stepping action), etc.,
- geometry input readers supporting ASCII, Root and STEP (CAD) formats
- a runtime database for geometry and parameter handling, and

- a fast simulation base services based on Virtual Monte Carlo [Bru+03] and the Root Tasks library

Particularly, the R3BRoot code is an instance of the FAIRRoot framework developed for the description, simulation and data analysis of the R^3B setup and experiments. The parts needed for the R^3B experiment simulation are: detector geometry, magnetic field maps, detectors hit registration, dedicated physics lists and dedicated event generators. [Ber11]. The framework provides a data structure based on Root trees and steers with Root macro commands.
The R3BRoot code, which will be used for the simulation and the data analysis, has a detailed structure of the CALIFA detector. The geometrical description includes the detailed volume of CsI crystals, the wrapping cover and the carbon fiber alveoli.

3 Theoretical background

This chapter will describe the theoretical background of this work. In the laboratory, several campaigns have been done. Here, the relevant physics processes are explained.

3.1 Fundamental properties

Basic properties of scintillators

Scintillators are undoubtedly one of the most widely used particle detection devices in nuclear and particle physics. They are used coupled with an amplifying device, such as a photomultiplier or a photo-diode, which converts its own scintillation light into an electric signal. A scintillator has three functions:

- conversion of particle energy to internal excitation,
- the conversion of the excitation of the transparent material to light, and
- transport of light to a photo sensor.

Various properties on the detected particles can be obtained from the signal of a scintillator. Among its features the most outstanding are: sensitivity to energy, fast time response and pulse shape discrimination. The scintillator is luminescent. When the material is exposed to any form of energy, luminescent materials absorb energy and re-emit it as visible light. This re-emission can be distinguished by response time:

- fluorescence: $t < 10^{-8}$ s,
- phosphorescence or afterglow: t is in the order of 10^{-6}s to hours.

The latter case happens because of the reemission being delayed by a metastable excited state [Leo12].

The scintillator's signal shows in general a simple exponential decay (see Fig. 3.1). This signal has to be considered as an overlapping of usually two components [Kra15]:

$$N(t) = A \cdot \exp\left(\frac{-t}{\tau_f}\right) + B \cdot \exp\left(\frac{-t}{\tau_s}\right), \tag{3.1}$$

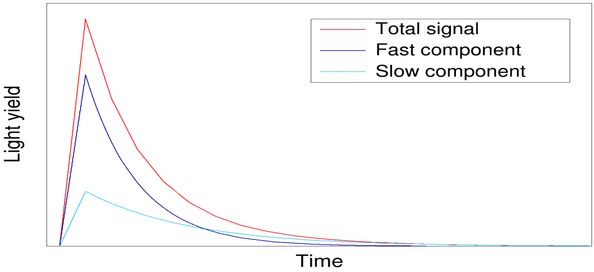

Fig. 3.1: Light yield of a scintillator with two decay constants. The red line shows the total signal of the scintillator, the blue line corresponds to the fast component and the cyan line to the slow component.

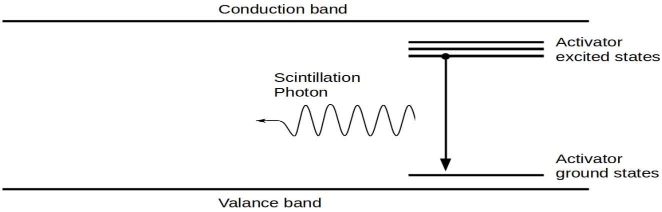

Fig. 3.2: The energy band structure of an activated inorganic scintillator.

τ_f,τ_s are the lifetimes of the fast and slow decay components, respectively.
Each component shows a different behavior for different types of incident particles. The decomposition of the components gives a hint to identify the particle detected by the scintillator. Details will be described in section 6.5.
The scintiallators are categorized by their materials, i.e inorganic or organic. Each categorized scintillator has a different scintillation mechanism.
CsI(Tl) is in an inorganic scintillator. The scintillation mechanism depends on the structure of the crystal lattice. CsI(Tl) consists of a pure CsI crystal and a small amount of additional Tl impurities, which are called activators, to obtain an additional energy state in the band cap. The electron can be excited into these additional energy states and back to the valance band [Oli16]. As a result, the probability of visible photon emission is enhanced (see Fig. 3.2). The typical half-life of the de-excitation is $\sim 10^{-7}$ s.

Detector volume

For γ-ray spectroscopy the size of the detector volume has to be considered. The mean free path of the γ-rays, secondary e^-/e^+ and X-rays following photoeffect have to compared with the size of the detector. Typical path lengths are the order of several centimeters. In the scintillator, when the incident energy of gamma-rays is larger than 1.022 MeV, pair production can occur which results in the production of 511 keV annihilation γ-rays. When the incident energy is sufficient to make pair production, it may lead to either full energy absorption or partial absorption. In the latter case, single or double escape peaks are detected on top of the Compton continuum [Kno00]. In segmented detection systems, the incident γ-ray has a chance of either losing its full energy or deposit energy in neighboring units, secondary γ-rays can occur also in the first segment. To deal with this, an add-back algorithm is required. It recovers the lost energy.

Particle detection

When charged particles penetrate matter, they lose their energy and are deflected from the incident direction. These effects are caused by the inelastic collisions with the atomic electrons and elastic scattering with nuclei. Especially in the case of $\mu^{\pm}$, $\pi^{\pm}$, p, α, these particles lose their energy mostly via inelastic collision in the matter. These charged particles lose their energy in matter by ionization. It can be described by the Bethe-Bloch equation, which gives the mean energy loss per unit length [Gro+00]:

$$-\frac{dE}{dx} = Kz^2 \frac{Z}{A} \frac{1}{\beta^2} \left[\frac{1}{2} ln \frac{2m_e c^2 \beta^2 \gamma^2 T_{max}}{I^2} - \beta^2 - \frac{\delta}{2} \right] \tag{3.2}$$

Here T_{max} is the maximum kinetic energy which can be transfered to a free electron in a single collision, $K = 4\pi N_A r_e^2 m_e c^2$, z and Z are the atomic numbers of the incident particle and medium, A is the mass number of the medium, I is the mean excitation energy and δ is the density effect correction to the ionization energy loss. The units of $\mathrm{d}E/\mathrm{d}x$ are MeV·cm^{-2}/g.

This average energy loss per unit path length can be expressed as a function of the kinetic energy. The left panel of Fig. 3.3 shows Eq. (3.2) as a function of the kinetic energy for different particles. It is divided into two energy regions. In the low energy region (around below GeV), $\mathrm{d}E/\mathrm{d}x$ decreases with increasing velocity. For this case $1/\beta^2$ factor dominates in Eq. (3.2). When the velocity of the particles is around 0.96c, dE/dx reaches a minimum and the particles are called minimum ionizing particles (MIPS). This minimum value is related to the charge of the particles. After this point, $1/\beta^2$ term becomes constant, consequently the

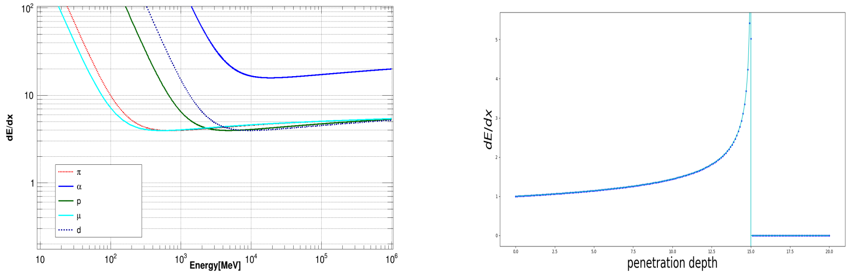

Fig. 3.3: The stopping power dE/dx as function of energy for different particles (left) and as a function of the path length (right).

dE/dx value increases the energy increase. Each particle has unique dE/dx curve below the minimum ionizing point. This property can be used as a method of particle identification.

These particles slow down in matter. The path length of the incident particle has to be considered to calculate the deposited energy in matter. The amount of ionization created by a heavy particle relates with its path length in the matter. This is called Bragg curve (Fig. 3.3: right). Most of the energy is deposited close to the end of the trajectory.

3.2 Sources used for laboratory tests

AmBe source

Isotopic neutron sources of ^{241}Am/Be type have found many applications in industry [Aka+01], scientific research, education and as calibration sources [Cro89]. They are portable and easy to shield. Americium emits an alpha particle, and beryllium produces neutrons following a nuclear reaction with the α-particle.

All low-Z targets are suitable for (α, n) neutron sources. ^{9}Be is the most important target because it offers the highest neutron yield [MKF04]. A stable alloy can be formed between Be and actinide α-emitters [Kno00]. The reaction channel is

$$ {}^{241}_{95}\mathrm{Am} \rightarrow {}^{237}_{93}\mathrm{Np} + {}^{4}_{2}\mathrm{He} + \gamma \tag{3.3} $$

$$ {}^{9}_{4}\mathrm{Be} + {}^{4}_{2}\mathrm{He} \rightarrow {}^{12}_{6}\mathrm{C} + {}^{1}_{0}\mathrm{n} + \gamma \tag{3.4} $$

The emitted α particle from the Am-isotope reacts with the beryllium capsule. An excited state of ^{12}C and neutrons are produced in this reaction.
The AmBe source has a nominal activity and the ratio of neutron emission as a reference value. To get the current activity, that value has to be converted using the half life of ^{241}Am, 432.6 years. Americium decays mainly via α-decay (α: 100 %, SF: $4{\cdot}10^{-10}$ %) [Nes15], thus the activity is related to the number of emitted alpha particles. These alpha particles react with the beryllium encapsulation and produce neutrons. This reaction produces γ-rays (E_γ = 4.44 MeV) from the exited state of carbon. Those γ-rays are the main source for the calculation of the efficiency. Here, the R-value is used to get the exact number of those γ-rays. The R-value is the ratio of the number of 4.44 MeV γ-rays to the number of neutrons produced in the source as a result of the α-reaction on ^{9}Be. This ratio was reported in several measurements [Jud63; Cro89; Che+07]. The R-value of the AmBe source is 0.535 ± 0.011. γ-rays and neutrons can be used in different ways to check the performance of the detector. The γ-ray can be used as a versatile source for the measurement. CALIFA aims to detect light charged particles and gamma-rays. The γ-rays from the AmBe source have a relatively high energy (E_γ = 4.44 MeV, see Fig. 4.6) thus making single and double escape peaks in the detector. For this case, the 511 keV gamma from e^+ annihilation might be detected in neighboring crystals [Abt+08]. Therefore, the source can be used to check the performance of the reconstruction algorithm. These gammas can also be used to calibrate the detector in the high-energy range as explained in section 4.1. In addition, the neutrons from the source will be used in several campaigns which are described in the following section.

Muons from cosmic-rays at sea level

Muons are the most numerous charged particles originating from cosmic radiation at sea level. Most muons are typically produced 15 km above the ground and lose about 2 GeV by ionization before the reaching the ground. Their energy and angular distribution is a convolution of the production spectrum, energy loss in the atmosphere, and decay. The mean energy of muons at ground level is about 4 GeV. The overall angular distribution of muons at the ground is proportional to $\cos^2\theta$ (θ with respect to the normal to the ground), which is characteristic for muons with $E_\mu \approx 3$ GeV [Ber+12].
There are sufficient cosmic muons to be a source in our measurement. They are an alternative solution to get high-energy particles in the laboratory.

3.3 Neutron reaction

Detecting neutrons is not the main purpose of CALIFA. Nevertheless, the neutrons from the AmBe source can be used to obtain other physics processes in the scintillator. The neutron temperature indicates the kinetic energy of the free neutron. They are categorized by their energy range: ultrafast neutrons ($>$ 20MeV), fast neutrons (1-20 MeV), thermal neutrons (0.0025 eV), etc. Neutrons show different reaction depending on the neutron energy. Here, the neutron reaction with fast neutrons ((n,X) reaction) and thermal neutrons (neutron capture) will be described.

(n,X) reaction

When a neutron enters the scintillator it also has a probability to react. In this case charged particles (p, α, d, etc.) are produced. Direct detection of these charged particle can occur in a proportional counter or a scintillator [WE14].
The (n,p) reaction or the (n,α) reaction are examples of nuclear reactions. These reactions occur when a neutron enters a nucleus and a proton or α leaves the nucleus. Neutrons do not have an electric charge. So they can reach the positively charged nuclei without any electric repulsive force [Jha04]. The (n,p) reaction consists of a proton in the nucleus being replaced by a neutron. So, the mass number of nucleus is kept and the charge of nucleus is changed. The (n,α) reaction consists of the nucleus capturing a neutron and emitting an α. When a fast neutron reacts with a heavier nucleus, the produced nucleus is usually radioactive [HB99; Mat+89].
The AmBe source emits neutrons with various energies up to 10 MeV [LZT07].These neutrons have a low cross section to interact in the scintillator. Still, through the (n,p) or (n,α) reaction, protons or α are produced and detected in the scintillator. These charged particles are also identified by the particle identification algorithm [BP14]. Four decay processes with neutrons are predicted in the CsI(Tl) crystal [Bor+63]:

$$^{133}\mathrm{Cs} + \mathrm{n} \rightarrow {}^{133}\mathrm{Xe} + \mathrm{p}$$

$$^{133}\mathrm{Cs} + \mathrm{n} \rightarrow {}^{130}\mathrm{I} + \alpha$$

$$^{127}\mathrm{I} + \mathrm{n} \rightarrow {}^{127}\mathrm{Te} + \mathrm{p}$$

$$^{127}\mathrm{I} + \mathrm{n} \rightarrow {}^{124}\mathrm{Sb} + \alpha$$

Thermal neutron capture

The other way to use these neutrons is as thermal neutrons. A thermal neutron is a neutron in thermal equilibrium with its surrounding medium. This temperature corresponds to 0.025 eV. The neutron produces prompt energy gamma-rays via the thermal neutron capture process [HLL81; Ram+04; Ish+77]. For example,

$$^{58}\mathrm{Ni} + \mathrm{n} \rightarrow ^{59}\mathrm{Ni} + \gamma \tag{3.5}$$

Moderators are used to reduce the speed of neutrons, thereby turning them into thermal neutrons. Hydrogen is the most efficient neutron moderator, and the neutron scattering cross section of H is either constant or slowly varying in the range $E_n = 0.1\sim$ 14 MeV. The optimal thickness of the moderator in our case was determined from theoretical calculations [Nei77] and a Geant4 simulation [Ble15] (see appendix A).

Polyethylene bricks are used to moderate the energy of the neutrons. More thermal neutrons are produced, so the interaction probability for thermal neutron capture is increased. The fast neutrons need the average path length in the moderator from 10 cm to 40 cm to be thermalized.

4 Measurements with the CALIFA PETAL

This chapter contains the description of the measurements to check the response of the CALIFA PETAL. The measurements were structured in three different parts, which aimed at measuring the response to different types of radiation: muons from cosmic rays, neutrons, and high energy γ rays with energies up to 9 MeV. To provide the latter two, an AmBe source was used. In addition, this chapter also describes the preparation of the main measurements, i.e. the calibration measurement, the gain matching and the assignment of channels.

4.1 Preparation measurement

Calibration measurement

The FEBEX3 board has an FPGA chip which applies the energy-filter algorithm for the charge sensitive preamplifier signal [Rus+13]. It converts the preamplifier signal to an energy value in arbitrary units. This can be calibrated with a gamma source.

The first calibration source is ^{22}Na, which has two γ rays (at 511 and 1274 keV). ^{22}Na is the calibration source for the γ-ray measurement using the AmBe source. These campaigns are done in the high sensitivity mode of the preamplifier, which is suitable for measuring in the low-energy range. Another source is the 4.44 MeV γ-ray from the excited state of ^{12}C from the AmBe source. The single and double-escape peak of 4.44 MeV γ-ray can be used for the calibration as well.

Muons from cosmic rays are measured in the low sensitivity mode of the preamplifier. In this mode the sodium spectrum becomes indistinct. In this case, the carbon spectrum can be used to calibrate the detector.

Figure 4.1 shows the energy spectrum of a single crystal. In the left panel the energy spectrum of the ^{22}Na source is shown and the right panel shows the ^{12}C spectrum, which has three gamma peaks; the ^{12}C-photopeak at 4.44 MeV, the associated single escape peak (3.93 MeV) and the double escape peak (3.42 MeV).

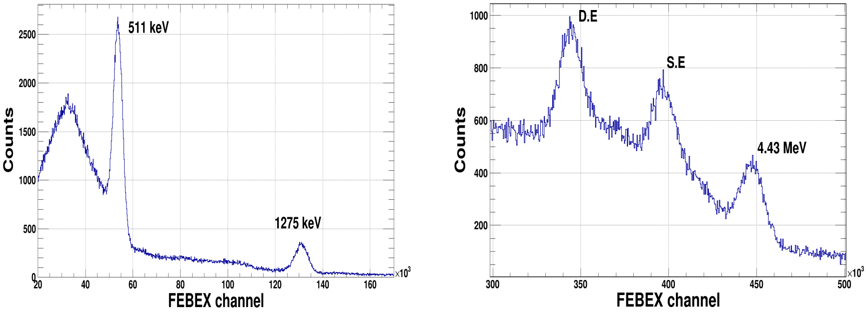

Fig. 4.1: Example of the energy spectrum from the single crystal. Left panel: ^{22}Na spectrum. Right panel: ^{12}C spectrum.

Gain matching

The gain matching is a part of the important preparation process to produce meaningful results by matching the energy signals. This step is achieved by adjusting the bias voltage of each APD. As already mentioned in chapter 2, the CALIFA barrel detectors are connected to the Mesytec MPRB-32 preamplifier. The amplifier can control the bias of each channel in 100 mV steps.

Figure 4.2 shows the superposed spectra of single crystals using a ^{22}Na source. The variation of the gain-matched spectra is smaller than the energy resolution. Each APD has a different recommended voltage to get the optimal performance and break down voltage. It restricts the gain matching by control with the bias voltage.

Gain stability

The measurement with the AmBe source, the thermal neutron capture experiment with a nickel target and the muon measurement require a lot of time to get sufficient statistics. In the measurement with the AmBe source, the single crystals in the CALIFA PETAL have a restricted opening window ($\sim 30{\times}15$ mm^2) facing the source. In the muon measurement, 2 plastic scintillators was used to get a coincidence signal. So these measurements consumed a lot of time.

During the measurement, several variables in the lab can cause fluctuations in the detector's output signal: electrical noise variations, temperature and humidity changes, etc. We supplied dry nitrogen gas to create a low humidity environment for the CsI(Tl) crystals in the CALIFA PETAL. The gas also stabilizes the temperature in the CALIFA PETAL. Nevertheless, the temperature variation in the

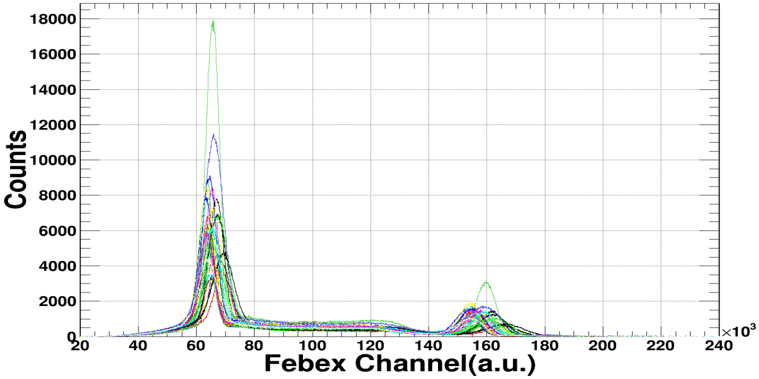

Fig. 4.2: ^{22}Na source spectrum of a single crystal. Each color corresponds to one channel in the CALIFA PETAL.

laboratory still can influence the output signal. It can cause smearing of the output signal, especially it can make it hard to distinguish the signal from the background in low-statistics events (e.g. thermal neutron capture process events). The Mesytec MPRB-32 has a temperature compensation function, but it can only control all 32 channels by one temperature sensor. It is not possible to adapt to a single channel. Therefore, gain stability has to be proven before the analysis. The result will be presented in section 6.1. This measurement took roughly 30 hours.

4.2 Measurement with the AmBe source

In this section details of the measurement with the AmBe source are given. It contains general information on the measurement; detector setup and a detailed of the measurement.
There are three campaigns in this measurement.

- γ rays from the AmBe: $E_\gamma = 4.44$ MeV
- thermalized neutron capture: $E_\gamma = 9$ MeV
- neutrons from the AmBe: $E_{neutron} < 10$ MeV

The AmBe source, which is used in the measurement, has X.3 encapsulation type; 22.4 mm diameter, 31 mm height, and 1.2 mm thickness wall.

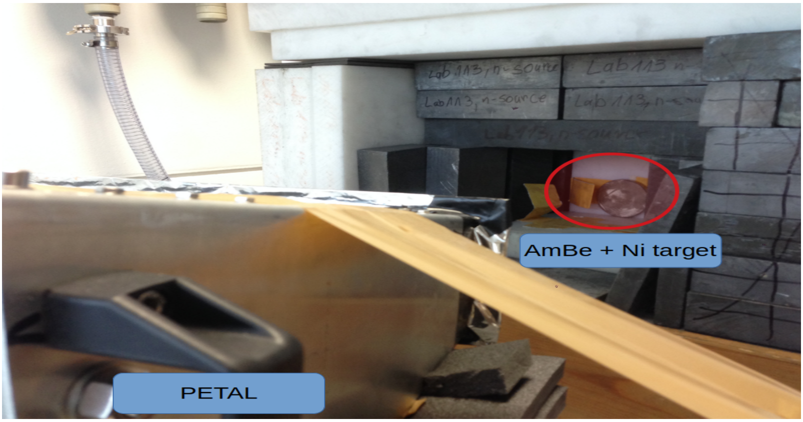

Fig. 4.3: Picture of the experiment setup during the AmBe source measurement. The PETAL is shown in front of the AmBe source.

Detector setup

Figure 4.3 shows the experimental setup during the AmBe source measurement. The left part in the photo displays a part of the CALIFA PETAL. The opening window of the PETAL is facing the AmBe source. The right part in the photo shows the AmBe source in its shielding. The inner layer of the shielding is made of several layers of lead bricks. For the outer layer paraffin plates are used. Polyethylene moderators are placed between the AmBe source and the opening. The nickel target, which is a metallic pad, is in front of the moderator. Figure 4.4 shows the schematic setup. The distance from the CALIFA PETAL to the target position is 60 cm. This distance is the minimum distance which allows to put the shielding structure and the PETAL itself. The PETAL is placed at an angle of 12° with respect to the AmBe source in order to optimise the geometry of the setup. There are two moderator bricks, each of them having a thickness of 5 cm. They are placed in front of the AmBe source. Additionally a nickel target (dia.: 7.5 cm, thick.: 1 cm) is used for the thermal neutron capture measurement.

Measurement with the AmBe source

The measurements have been performed using different setups. Table 4.1 presents details of them. Run 1 used 3 targets in a row: one target with a thickness of 3 cm and two with a thickness of 1 cm each.
Neutrons are emitted from the source isotropically. So, when the thickness of the target is increased in the alignment line of the target this increases the interaction

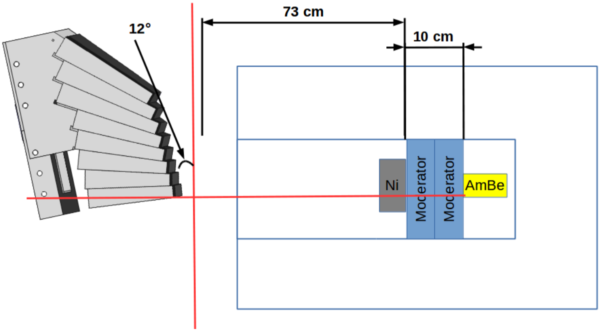

Fig. 4.4: Detector setup for the AmBe measurement

Run Id.	Total measurement time (s)	Thickness of	
		Target (cm)	Moderator (cm)
1	682512	5	15
2	160435	-	10
3	937938	1	10
4	1471506	1	10
5	685988	1 × 2	10

Table 4.1.: Information on the measurement with the AmBe source.

probability. Consequentially, this run has fewer γ rays from the capture process. The γ rays from the thermal neutron capture also scatter in the nickel target. The thickness of the moderator also influences the rate of the detected γ rays. For run 2 the thickness of the moderator was decreased and the data are taken without a nickel target. In run 3 only one nickel target was used. In run 4 were taken data with a high threshold close to 1 MeV. This run focused on high-energy lines. In the energy spectrum of run 3, the number of events of the energy lower than 1 MeV is 4.5 times larger than the number of the events of the energy higher than 1 MeV (Fig. 4.5).

To compare these two runs, the peak-to-background ratio of the thermal neutron capture events is used. It is simply calculated by subtracting the entry of the background to the signal (Eq. (4.1)).

The ratio of the run 3 is 0.098 and the run 4 is 0.157.

$$\text{ratio} = \frac{\text{peak} - \text{background}}{\text{background}} \tag{4.1}$$

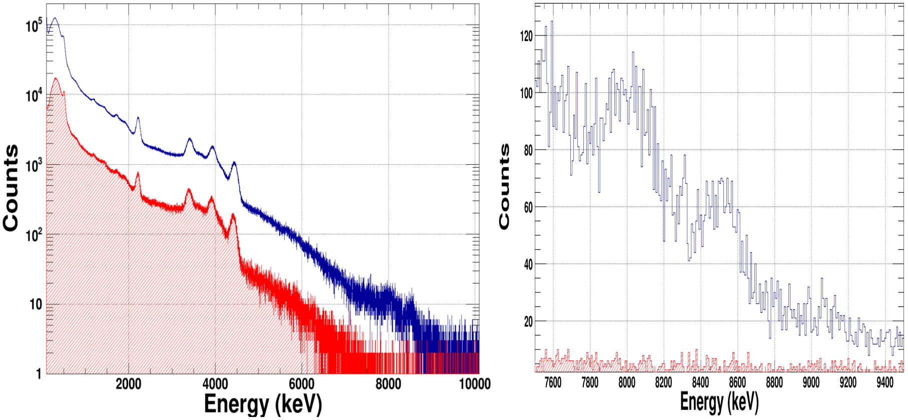

Fig. 4.5: Energy spectrum of a single crystal. The blue line shows AmBe source spectrum with a nickel target. The red line shows the AmBe source spectrum without the nickel target. The high-energy area in linear scale (right)

For the last run two nickel target disks were used to increase the reaction probability (run 5). So, there are more events in the high-energy area visible.

Figure 4.5 shows a comparison of energy spectra obtained with a single crystal. The average of count rate per crystal is 11942 events/s. In red is shown the energy spectrum of run 2, which is without a nickel target. The blue spectrum shows the energy spectrum of run 3. Both spectra have detected energies higher than 4.44 MeV. Obviously, they i.e. an energy spectrum with a nickel target are different for energies higher than 7 MeV. Around 9 MeV, there are two dominant peaks, which correspond to the single and double escape peak of the 9 MeV thermal neutron capture peak.

Figure 4.6 shows the energy spectrum of run 4, which has a high threshold (E_{th} > 1 MeV) set: In the laboratory, there are different sources of γ rays. The nickel capture process shows relatively low statistics. A high threshold of 1 MeV is applied to obtain more statistics in high-energy events. In the spectrum, the 2.223 MeV peak, which comes from the ^{1}H(n,γ)^{2}H reaction in the moderator, and the ^{12}C peak are still dominant. But, the high-energy area is now better visible.
The other task of the neutron measurement is to distinguish the detected signals of the different types of particles in the scintillator. A neutron in the scintillator causes a recoiling protons. That deposit their energy in the crystal and cause additional events. These particles can be separated from the γ-ray events using the RPID algorithm. The detailed results will be presented in Chapter 6. The setup

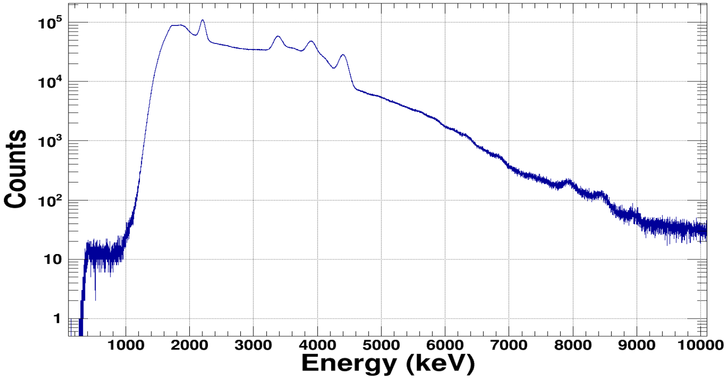

Fig. 4.6: Single energy spectrum with nickel target. A threshold was set 1 MeV.

of the measurement is the same as in the previous measurements. In addition, it uses the neutrons without the polyethylene block to get more fast neutrons. This measurement used the specified DAQ, which is developed by the CALIFA group. It is based on the FEBEX board and has dedicated add-on board for CALIFA's signal processing.

4.3 Muons from cosmic rays

Cosmic rays are one of the natural background radiation sources. They can be utilized as calibration source and to check the performance of the detectors.

Detector setup

In the AmBe source measurement the internal trigger mode in FEBEX was used. On the contrary, the muon measurement used the external trigger. Two plastic paddle scintillators (10×50 cm^2 each) are used as trigger detectors in the measurement. Here, the measurement has the prerequisite that the events are only selected if the muons penetrate the PETAL completely. The plastic scintillators covered only part of the PETAL. The output signal is processed via a constant fraction discriminator (Ortec, 935 Quad. CFD). The processed signals make a coincident signal by using a logic unit module (Ortec, CO4020. Quad. 4-input logic). This signal is connected to the exploder, which produces a trigger signal for the DAQ PC and the FEBEX crate. It is used as an external trigger for the FEBEX.

The 4 FEBEX boards are connected to 2 preamplifiers (each 32 channels) on the

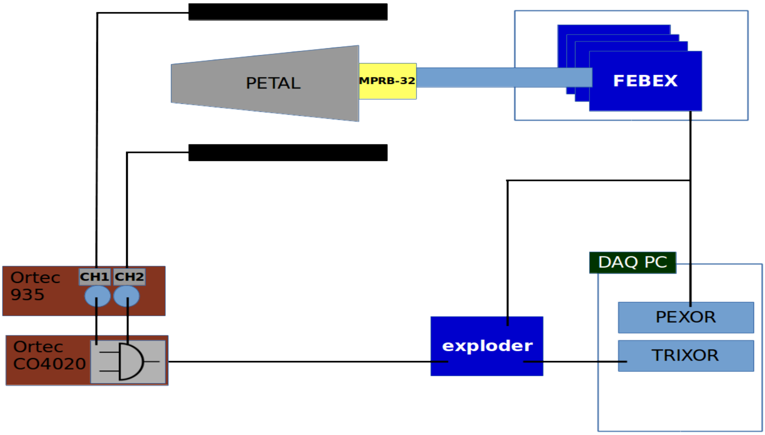

Fig. 4.7: Schematic diagram of the DAQ system used during the cosmic-ray measurement with external trigger.

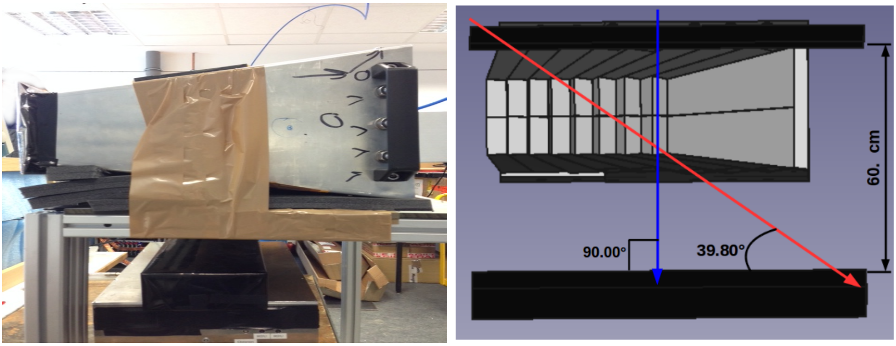

Fig. 4.8: The set up during the muon measurement. The left panel: picture of the muon measurement. The right panel: detector setup for muon measurement.

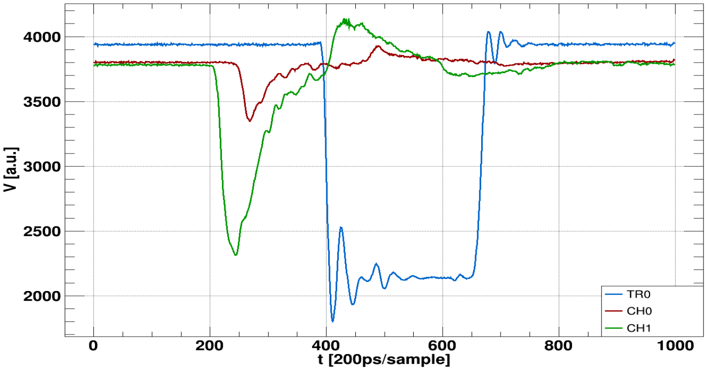

Fig. 4.9: The traces of the digitizer's signal from the trigger scintillator.

PETAL and also to the DAQ PC via an optical cable. The preamplifier is set to low sensitivity (30 pC) to detect the muons caused by cosmic rays. The DAQ PC has two specific boards: PEXOR and TRIXOR. The PEXOR is a PCI-express optical receiver. It is connected to the FEBEX module and the DAQ PC. The TRIXOR is the MBS trigger master, which connects the EXPLODER to the DAQ PC. An accepted readout trigger signal from the source arriving at the EXPLODER will be distributed to the TRIXOR and FEBEX boards. Figure 4.7 shows the schematic diagram of the DAQ system.

Figure 4.8 is a photo of the detector setup of the muon measurement. One plastic scintillator was placed above the PETAL and the other plastic paddle was placed below the PETAL. The position of the trigger detector is 10 cm from the opening window of the PETAL. This is the actual staring point of the CsI(Tl) crystals. The space between the two plastic scintillators is 60 cm. This distance corresponds to the minimum cosmic ray incident angle of around 39.80°.

Measurement of muon

The trigger signal from the plastic scintillator is split in two ways to the trigger module and the digitizer (CAEN V1742). One branch of the trigger signal monitors the trigger during the measurement. Figure 4.9 is an example of the trigger signal. The two signals come from the plastic scintillators (CH0,CH1) and the blue graph is the signal from the coincidence module (TR0). The height difference of the voltage signal occurs because of the difference in the applied voltage.

The first aim of the muon measurement is the selection of the group of the crystals

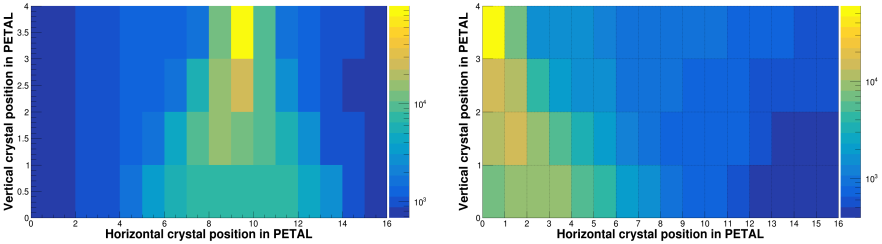

Fig. 4.10: 2D plot of the measured event distribution. It presents the crystals which fired related to the gate crystal.

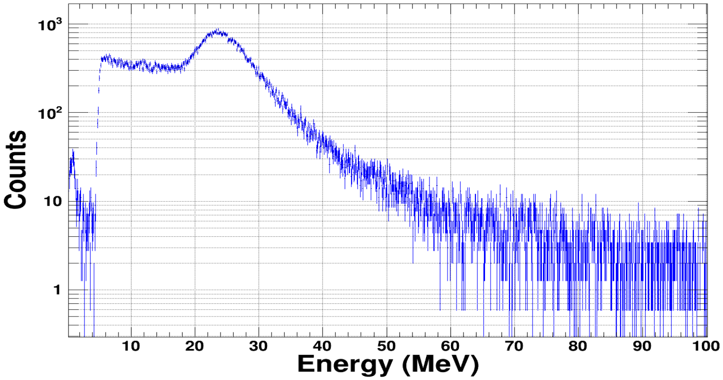

Fig. 4.11: Deposited energy spectrum of muons in a single crystal

which detect the event. Figure 4.10 shows the 2D crystal mapping of the event distribution. The x-axis represents the polar angle of the 16 crystals of the PETAL and the y-axis represents the 4 layers of the azimuthal angles. In the case shown on the right panel a gate crystal, which is on the top layer and hit first, in the middle of the PETAL is selected (Fig. 4.10: left) and the coincident crystals in the same event are counted. These crystals are defined as the ones which are in the same event and have a time signal later than the gate crystal (see section 6.3.1). For the second case the gate crystal on the left side of the PETAL (Fig. 4.10: right) and the coincident crystals are plotted.

After the selection of the crystals involved in the event, their properties are studied. The muons deposite their energy in the crystals partially (Fig.4.11). The deposited

energy correlates with path length in the crystal.
The muons were measured for about 163 hours with the standard FEBEX in the external trigger mode.

5 Simulation

This chapter describes the simulation of the measurements, which are explained in chapter 4. This work's idea is to cross-check the performance of the CALIFA PETAL. In addition, it will prove the result of the R3BRoot [Ber11] simulation toolkit.

5.1 R3BRoot

R3BRoot is used to simulate the previously mentioned measurements, both the one done with the AmBe source and the one done with muons from cosmic rays. It is expected to reproduce detailed physics related to not only the reaction with the scintillator material, but also with the structure of the segmented detection system. The R3BRoot has a data structure as follows:

- MCTrack
- CrystalHit
- CaloHit

"MCTrack" is the raw data of the simulation. It contains the track information on Monte Carlo level: PDGcode (particle data group code), energy, momentum, mass etc. "CrystalHit" is the data structure containing the information returned by the digitizer. It contains the energy deposited in each crystal, time, crystal ID, etc. "CaloHit" is the data structure containing the information reconstructed from individual crystal hits that fulfill proper conditions (threshold, angular window). It contains the total deposited energy, time, angle and information of the pulse shape (N_f,N_s), etc. [AP11].
To obtain a proper simulation, the following information must be specified: a detector structure, a particle generator and a physics list for the modeling.
First, the detector structure is considered. It needs the geometry information of the CALIFA PETAL and a suitable physics model for CALIFA. The R3BRoot already includes information on the detecting system belonging to R^3B experiments: dimensions, geometries and materials. The simulation toolkit has several versions of CALIFA (barrel or barrel+endcap) and also the structure of the demonstrator (2 PETALs), which were prepared for a previous experiment [Pie+16]. This project

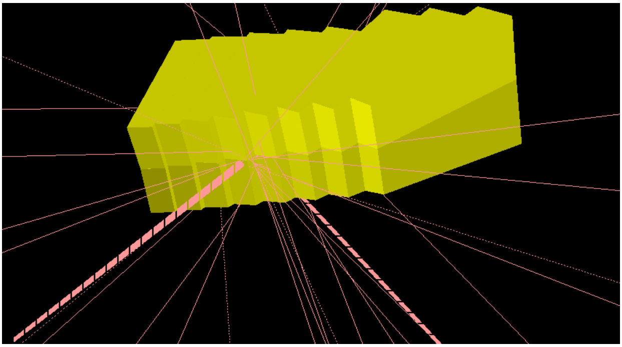

Fig. 5.1: Detector structure of one CALIFA PETAL in the R3BRoot.

included only one PETAL, so the model was modified to the geometry version of the demonstrator.

The PETAL in the simulation reflects the existing PETAL, whose CsI(Tl) crystals have 3 different shapes. Also, it includes the wrapping layer and the outer carbon fiber structure. R3BRoot can use the CAD coordinates to define the dimensions of the object and to place each component in the "detector world".

The next step is to generate the primary particles. The AmBe source measurement can be modeled by two sources: capture reactions with γ-rays up to 9 MeV and the reactions with neutrons. The γ-ray simulation focuses on the γ-rays from the AmBe source and the γ-rays (E_γ = 8.999 MeV) from the thermal neutron capture with the nickel target. The neutron measurement uses the neutron spectrum of the AmBe source. The event generator chooses the energy of the particle and traverse the experimental hall from the center of the full CALIFA barrel area to the PETAL. On the other hand, in the cosmic ray simulation a muon is generated, for which the distribution of the momentum and the incident angle at the sea level of muons is applied [BA13].

The simulation engine needs to optimize the simulation. R3BRoot has three types of simulation engine (Geant3, Geant4 and Fluka). The user can choose one of the simulation engines. The Geant4 engine is the main engine of this work. In addition, for the low-energy neutron simulation the Geant3 engine was selected [Kre]. The result of Geant3 can be a reference for the direct reaction of fast neutron.

The primary particles are generated by one of the mentioned engines. Afterwards these particles interact with the simulated "world", and for this the best suited model needs to be selected. The default physics list is QGSP_BERT _EMV. This model is based on QGSP_BERT, which uses the Geant4 Bertini cascade, but

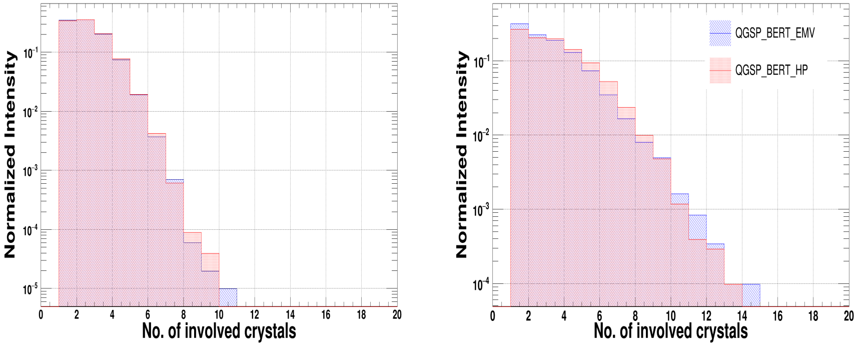

Fig. 5.2: Number of involved crystals per event. Left panel: γ-rays (E_γ = 4.43 MeV). Right panel: Neutrons (E_n = 4.39 MeV)

parameters of electromagnetic processes which are tuned to yield better CPU performance with only slightly lower precision [Gea13]. However, this decreases the EM precision slightly. It causes a difference in the result of the energy range up to 10 MeV. Figure 5.2 shows the difference of the physics lists. The blue area corresponds to the default physics list of R3BRoot (_EMV) and the red line corresponds to the high precision model (_HP). The high precision model describes the particles down to low energies in the detector. As a result, the number of involved crystals in the event is increased. The physics model of R3BRoot works with the physics list and the additional physics cut. It also adopts the Virtual Monte Carlo (VMC) in ROOT. In order to activate the support of VMC features like VMC cuts and VMC process controls, the user has to activate the special processes defined in the TG4SpecialPhysicsList.

5.2 AmBe source measurement

Neutron reaction

Neutron reactions with the PETAL are one task of the simulation. The emitted neutrons from the AmBe source have several energies [LZT07]. In contrast to Geant4, R3BRoot cannot use the General Particle Source (GPS), which allows the specification of the spectral, spatial and angular distribution of primary source particles, for event generation. So, the AmBe source simulation generates neutrons with the energy and intensity that are estimated from the neutron spectrum (Fig. 5.3). Most primary energies of the neutrons are distributed around 2 MeV

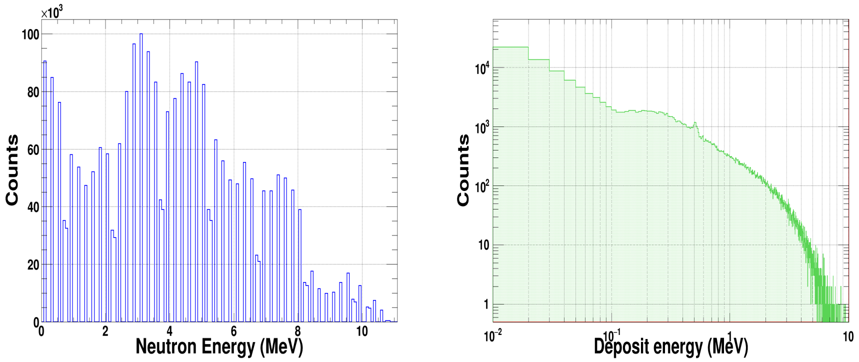

Fig. 5.3: Simulation of the AmBe source. Left panel: Energy spectrum of primary neutrons. Right panel: Detected energy spectrum of single crystals with the AmBe source.

to 5 MeV, and the intensity of the high-energy neutrons ($E_n > 8$ MeV) is relatively low. Additionally to simulating the AmBe source and selecting these energies, the interaction detector needs to simulated.

As mentioned before, R3BRoot works with a selected engine plus specific conditions for the physics process. There are three different possible settings; "Geant4+without specific cut", "Geant4+specific cut" and "Geant3+specific cut". The differences can be shown by comparing the number of involved crystals in the events. The involved crystals show the propagation of the particles in the units of the single crystals. These values do not only count neutrons, but also secondary particles. The simulation was done using a neutron as a incident particle. Each energy and intensity is shown in left panel of the Figure 5.3. Figure 5.4 shows the number of the involved crystals in the AmBe source simulation. The green area is the value of the Geant4 without applying any cuts on the physics process. The red area is the result of applying a cut on the physics process using the same engine. The blue line is the result of using Geant3. The second and third case used a common configuration file (SetCuts.C). So, they show similar behavior in the propagation of the particles. It is divided into two parts: SetProcess, SetCut.
The "SetProcess" function is defined with two variables and sets the process control. The first variable is the flag of the process name and the second variable is the flag value. The default setting of the R3BRoot refers to a complete simulation which generates and follows also secondary particles. The "SetCut" function defines the

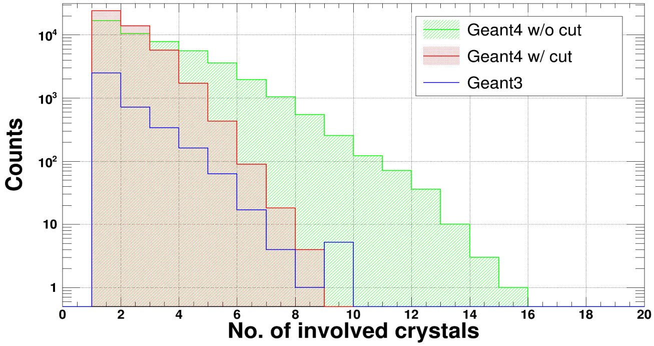

Fig. 5.4: The number of involved crystals of the event depending on used engine.

variable name and the cut value. The details of the configuration file are described in the box below.

```
//SetCuts.C
 gMC->SetProcess("PAIR",1); /** pair production*/
 gMC->SetProcess("COMP",1); /**Compton scattering*/
 gMC->SetProcess("PHOT",1); /** photo electric effect */
 gMC->SetProcess("PFIS",0); /**photofission*//
 gMC->SetProcess("DRAY",1); /**delta-ray*/
 gMC->SetProcess("ANNI",1); /**annihilation*/
 gMC->SetProcess("BREM",1); /**bremsstrahlung*/
 gMC->SetProcess("HADR",5); /**hadronic process*/
 gMC->SetProcess("MUNU",1); /**muon nuclear interaction*/
 gMC->SetProcess("DCAY",1); /**decay*/
 gMC->SetProcess("LOSS",1); /**energy loss*/
 gMC->SetProcess("MULS",1); /**multiple scattering*/

 Double_t cut1 = 1.0E-4;         // MeV --> 1 keV//
 Double_t cutb = 1.0E4;          // GeV --> 10 TeV
 Double_t tofmax = 1.E10;        // seconds

 gMC->SetCut("CUTGAM",cut1);   /** gammas (GeV)*/
 gMC->SetCut("CUTELE",cut1);   /** electrons (GeV)*/
 gMC->SetCut("CUTNEU",cut1);   /** neutral hadrons (GeV)*/
 gMC->SetCut("CUTHAD",cut1);   /** charged hadrons (GeV)*/
 gMC->SetCut("CUTMUO",cut1);   /** muons (GeV)*/
 gMC->SetCut("BCUTE",cut1);    /** electron bremsstrahlung (GeV)*/
 gMC->SetCut("BCUTM",cut1);    /** muon and hadron bremsstrahlung(GeV)*/
 gMC->SetCut("DCUTE",cut1);    /** delta-rays by electrons (GeV)*/
 gMC->SetCut("DCUTM",cut1);    /** delta-rays by muons (GeV)*/
 gMC->SetCut("PPCUTM",cut1);   /** direct pair production by muons (GeV)*/
 gMC->SetCut("TOFMAX",tofmax); /**time of flight cut in seconds*/
```

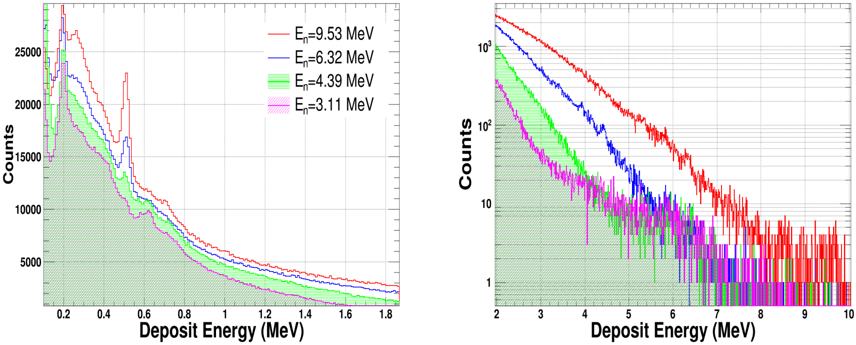

Fig. 5.5: Comparison of the deposited energy for selected neutron energies. Left panel: Energy spectrum in the low energy range (up to 2 MeV). Right panel: Energy spectrum in the high energy range.

To focus on the physics at certain neutron energies, five neutron energies are selected for the simulation (3.11, 4.39, 6.32, 7.39 and 9.53 MeV), which are the dominant energies in the AmBe spectrum.

First, the single crystal spectrum is considered. Figure 5.5 shows the comparison of the single crystal spectra for selected energies. In the low-energy spectrum (Fig. 5.13: left panel), the energy spectrum caused by a 3.11 MeV neutron has inelastic neutron scattering peaks, which are ^{127}I(n,n$'$ γ) γ-rays with the energy E_γ = 202 keV [CKR79] and ^{133}Cs(n,n$'$ γ) γ-rays with the energy E_γ = 632 keV. Inelastic scattering on ^{127}I also appeared in the other neutron energy spectra. But this energy peak is smeared out due to other low energy events in the measured energy spectrum of the AmBe source. In contrast, inelastic scattering of ^{133}Cs decreases as the incident neutron energy increases. 511 keV γ rays are detected at initial neutron energies of more than 4.39 MeV.

Another interesting property is the number of involved crystals of the events. Here, not only neutrons are counted, but other secondary particles as well. Neutrons penetrating the crystal without changing direction is the most probable event independently of the energies. The maximum number of the involved crystals is inversely proportional to the incident neutron energy. The left panel of Figure 5.6 shows one example of the involved crystals of the events. It is simulated with the Geant4 engine with a specified cut (Box in p.45). Each color code indicates a different incident neutron energy. In case the incident energy increases, the secondary particles can propagate to the next crystals. The right panel is the average value of the

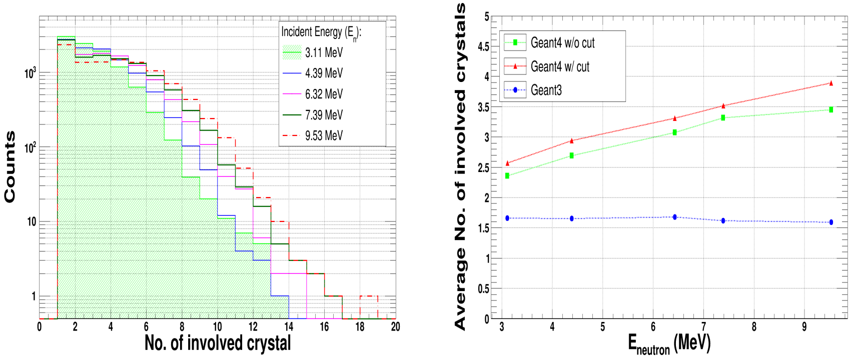

Fig. 5.6: Comparison of the number of involved crystals using different simulation engines. Left panel: One example of the involved crystals of the selected neutron energies. Right panel: Involved crystals comparison of the simulation engines.

involved crystals. It is the average value of the all events dependent on incident energy and the simulation engine. It shows a similar trend for both cases using Geant4 but a different to the Geant3. The value of the AmBe simulation are 2.98 (Geant4 without cut), 3.25 (Geant4 with cut) and 1.64 (Geant3) on average.

The last task of the neutron simulation is identifying the particles in the scintillator. Especially positively charged particles from (n,X) reaction can be detected in the scintillator.

In spite of the low cross section for high-energy neutrons, it is expected to get neutrons with energies up to $E_n = 10$ MeV. The following reactions are expected to produce charged particles: ^{127}I(n,p)^{127}Te and ^{133}Cs(n,p)^{133}Xe or ^{127}I(n,α)^{124}Sb and ^{133}Cs(n,α)^{130}I. These interactions are indistinguishable in the energy spectrum. The PID process allows to distinguish these particles. The data structure of R3BRoot already includes the fast component (N_f) and the slow component (N_s) as a member of the data tree. These members can be used by the RPID algorithm. The main focus of this simulation is using the RPID algorithm to distinguish γs and protons at a similar energy. Here, the possibility of the RPID in R3BRoot explained and details of RPID will be given in section 6.5. Figure 5.7 shows examples of the RPID spectrum. The fast component is plotted on the x-axis and the slow component is plotted on the in y-axis. The first row shows the case of the lowest incident energy (E = 3.11 MeV) of the single neutron simulation. The second row is the case of the highest incident energy (E = 9.53 MeV). The third row is the case of the full neu-

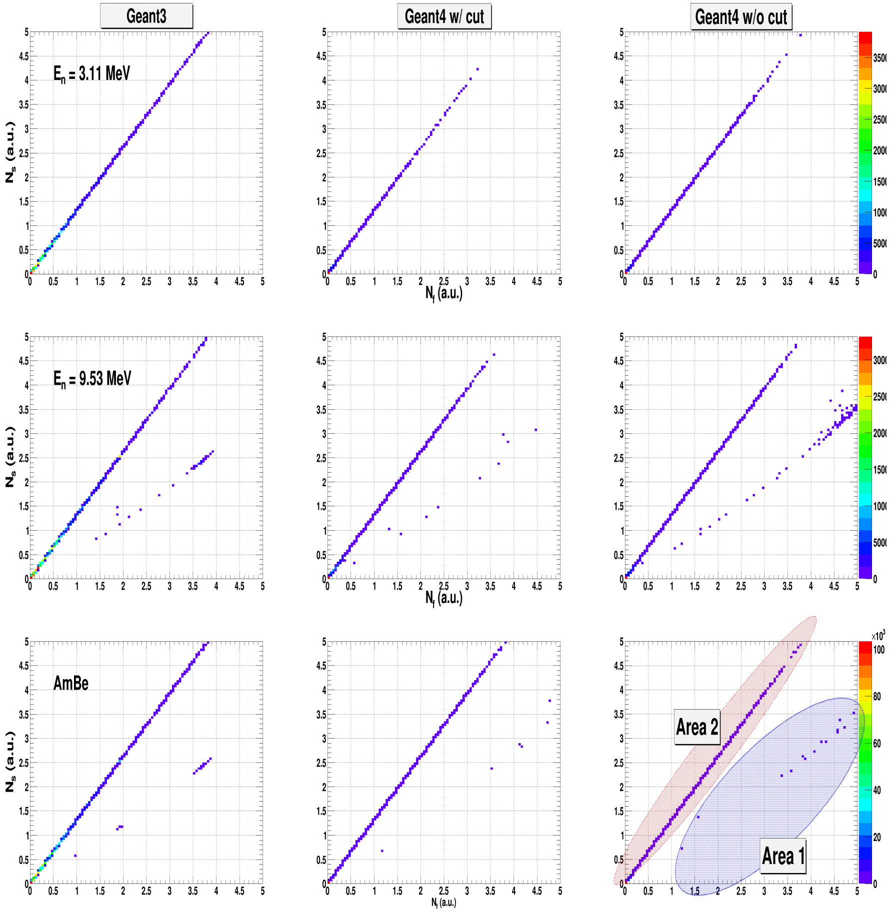

Fig. 5.7: The RPID spectrum in the R3BRoot simulation. The cases for incident neutron energies 3.11 MeV, 9.53 MeV and for the full energy spectrum of the AmBe source are shown.

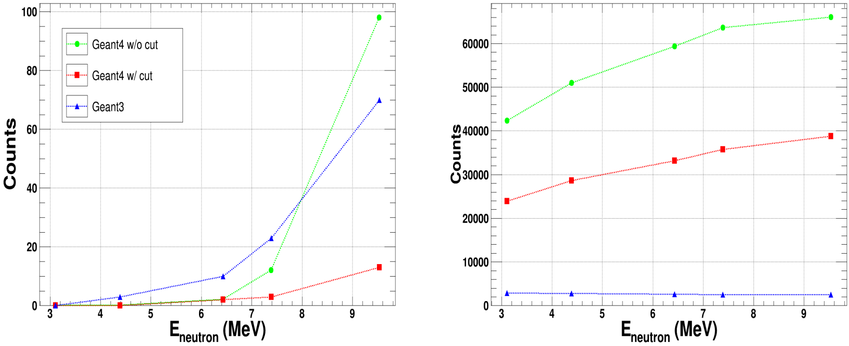

Fig. 5.8: Particles identificiation by the RPID algorithm. Left panel: The charged particles in "Area 1". Right panel: The neutral particles in "Area 2". See Fig. 5.7.

tron spectrum of the AmBe source (see Fig. 5.3). Each case was also simulated with different simulation engines. This result is simply divided into two areas, which are the charged particle track area (Area 1: the blue colored circle in Fig. 5.7) and the neutral particles track area (Area 2: the red colored circle in Fig. 5.7).

The tracks of each area are counted to compare the results (Fig. 5.8). The left panel shows the number of particles, which belong to "Area 1", as function of the incident energy. The right panel shows the number of the particles in "Area 2". From the result of "Area 1", it can be figured out that the process configuration file in R3BRoot sets a limit for the propagation of low-energy particles in the scintillator. Both Geant4 cases show inelastic scattering starting at 6.32 MeV. Only Geant3 starts this process at 4.39 MeV. This simulation was checked carefully; for each energy the simulation was done with same number of events. In contrast, the intensity of emitted neutrons with the energy 4.39 MeV, 6.32 and 9.53 MeV correspond 86%, 55% and 16% relative to neutrons with the energy 3.11 MeV, respectively. So, the total rate of the inelastic scattering events decreases.

Finally, the emitted neutron energies from the AmBe source are applied in the simulation. The number of events in "Area 1" are 11 counts (G4+cut), 17 counts (only G4) and 26 counts (G3+cut) of out 2671835 neutron events.

High-energy γ rays

The other task of the simulation, which belongs to the AmBe source, is the simulation of high-energy γ rays. This simulation uses only two γ-ray energies: 4.44 MeV (from AmBe) and 9 MeV (from thermal neutron capture on the nickel target). These two γ-ray energies are used as a sources in the reconstruction algorithm. Especially the γ-rays from the thermal neutron capture processes are the main task of this simulation. When the high energy γ-rays penetrate the PETAL, some γ rays are not totally absorbed in a single crystal, but also in neighboring crystals. This is caused by the geometrical limit of the crystal.

The reconstruction algorithm included in R3BRoot converts each single-crystal hit level to the calorimeter hit level. The algorithm defines the related crystals in a single event and converts all related crystals to one reconstructed calorimeter hit. In this work only one PETAL is used for the simulation, so the reconstruction algorithm does not work properly and cannot be directly applied. Thus, we take the main idea of the algorithm for R3BRoot and modify this algorithm to fit our case. This algorithm was created by a former member of our group [Lut13](see section 6.3.2 for details on the algorithm). It is also applied in this work. In the simulation, the natural background in the laboratory was not considered.

The number of γ-rays from the nuclear reaction of beryllium and alpha particles is sufficient for the calibration. They can be selected as the source of high-energy γ-rays to reconstruct events using the algorithm. The left panel in Figure 5.9 shows the deposited energy spectrum from a single crystal. And on the right panel the resulting energy spectrum of the applied reconstruction algorithm is shown. This simulation used only 64 crystals, which are only a part of the total CALIFA barrel. This puts a limit to the reconstruction of the events. As a result, the single-escape gamma events are still in the reconstructed histogram (Fig. 5.9: right panel).

The efficiency of the algorithm can simply be estimated from the result by taking the ratio between detected full-energy hits before and after applying the reconstruction algorithm. The other γ-ray energy of the simulation is 9 MeV, which is the expected energy coming from thermal neutron capture of the nickel target. Figure 5.10 shows the result with same structure as in the case of 4.44 MeV γ-ray. The detailed numbers of the results are given in Table 5.1.

The last part addresses the simulation of the nickel target when irradiated with thermal energy neutrons (E_n = 0.025 eV). Two different kinds of γ rays are produced using that target (Fig. 5.11), one energy comes from ^{58}Ni (E_γ = 9.00 MeV) and the other one from ^{62}Ni (E_γ = 6.83 MeV). This simulation used the same dimensions of the target as in the measurement. The thermal neutrons impinge on the target. The dedicated physics list of the high-energy collisions does not include the total physics model down to the thermal energy neutrons. Because of this the

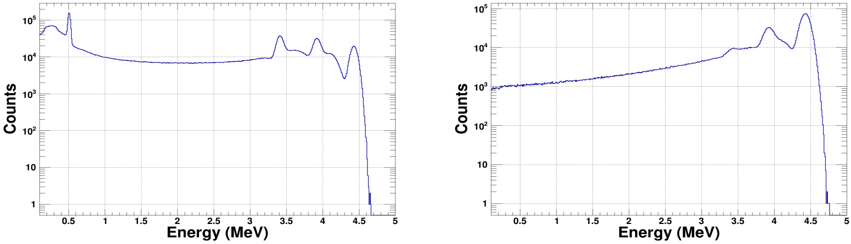

Fig. 5.9: R3BRoot simulation data for 4.44 MeV γ-rays: The left panel shows the energy spectrum of single crystals. The right panel shows the resulting energy spectrum after application of the reconstruction algorithm.

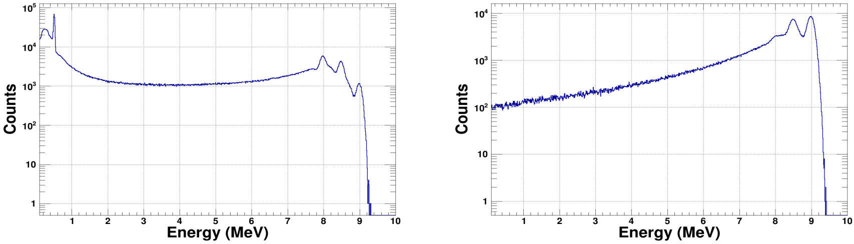

Fig. 5.10: R3BRoot simulation data for 9 MeV γ-rays: The left panel shows the energy spectrum from single crystals. The right panel shows the resulting energy spectrum after application of the reconstruction algorithm.

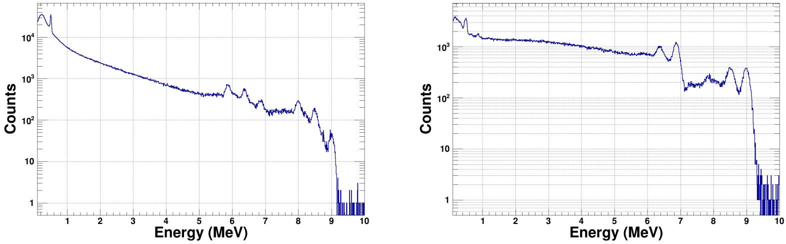

Fig. 5.11: R3BRoot simulation data for thermal neutron capture on a nickel target: The left panel shows the energy spectrum from single crystals. The right panel shows the resulting energy spectrum after application of the reconstruction algorithm.

E_γ (MeV)	No. of full energy γ-ray		ratio of reco(%)	Type of primary
	Before reco	After reco		
4.44	179034	911080	80.34	single energy gammas
9.00	17771	164472	89.20	
6.83	7821	23249	66.35	thermal energy neutrons
9.00	676	7212	90.63	

Table 5.1.: The number of reconstructed events for the high energy γ ray simulation. These values are compared with the detected full energy event before the reconstruction.

simulation skipped the thermalization process in the paraffin moderator and the nickel target.

Table 5.1 shows the results of the high energy γ-ray simulation. It presents how many events are reconstructed by the algorithm. The first two cases are the simulation with single gamma energies only and the next two cases are the simulation of the thermal energy neutrons captured by the nickel target, which has higher gamma background. The results show that reconstruction ratio are higher for the single γ-rays.

5.3 Muons from cosmic rays

The cosmic-rays measurements are focused on the reaction with muons, because they are the most numerous charged particles at sea level. The simulation determines the type of the incident particle. It also has to consider the energy and incident angle of the muons. The main parameter to determine the incident angle of the muon is the relation between incoming angle and the zenith line of the detector. The zenith angle (θ) dependence of the muon intensity at sea level is given by

$$I(\theta) = I(0^\circ) \cdot \cos^n(\theta), \tag{5.1}$$

where $I(0^\circ)$ is the intensity at 0° and n is a function of the muon momentum. The value of n for a 1 GeV muon is 1.95 ± 0.10 [BA13].

The other parameter of the primary particle is the energy of the muons. The study of the energy distribution at sea-level was done with several tools (Geant4, MCNPX and FLUKA) [HLW07]. The event generator provides primary particle with various energies and angles. Figure 5.12 shows the distribution of the primary particles in the generator level; the energy distribution (left) and the incident angle distribution(right).

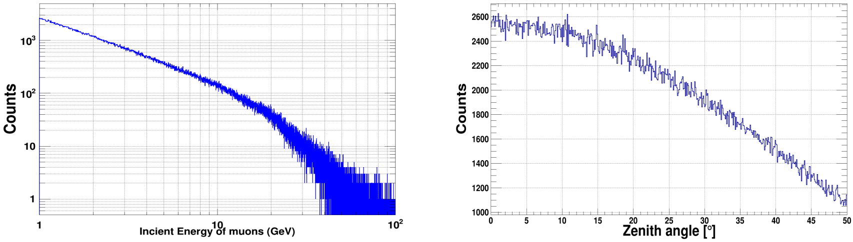

Fig. 5.12: Histogram of the generated cosmic muons in the primary generator. Left panel: Primary energy distribution produced by the event generator. Right panel: Zenith angle distribution.

The primary muons cross the PETAL in vertical direction, which is not the side of the PETAL with the opening window (see Fig. 4.8: right panel).

Also, the active area of the PETAL has to be considered. In the measurement, the two plastic scintillators are used to make the trigger signal for the event (section 4.3). They also restrict the active area and the incident angle of the muons. The primary particle determines the starting position on the surface of the plastic scintillator (10×50 cm^2). In addition, the zenith angular dependency of the muon has to considered [KB03]. The zenith angle is restricted from 0° (the vertical on the PETAL) to 50.2° (the elevation angle: 39.8°, see Fig. 4.8: right).

Generally, muons are not fully absorbed in the detector and most of them punch through the detector. As a result, the muon energy spectrum registered by a detector does not show a single-peak spectrum. Figure 5.13 shows these results. As the CALIFA PETAL has CsI(Tl) crystals with three different shapes, there are three different lines shown in different colors. The green line histogram is the energy spectrum of the longest crystal (type: 1101, see Table 6.2). The blue line histogram is the energy spectrum of the medium length crystal (type: 1103). The red line histogram is the energy spectrum of the shortest crystal (type: 1105). The intensity in show each histogram is normalized to compare them more easily with the other cases.

Here, the direction of the incident particles has also to be considered. This was already mentioned in section 4.3 (cosmic-rays measurement). In the simulation only restricted places and angles are allowed. Consequently, each crystal has a different active area. The active area of the 170 mm crystals is larger than for the 220 mm crystals. The maximum deposited energy is dependent on the crystal dimension. For the crystal type with 170 mm length the deposited energy is 22.85 MeV, for

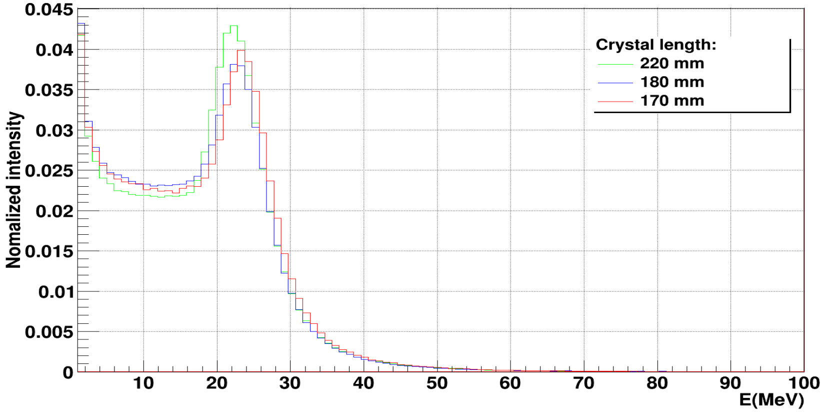

Fig. 5.13: Simulated and normalized energy spectra of muons for different crystal shapes. The green line corresponds to the longest crystal (220 mm), the blue line to the 180 mm one and the red line to the 170 mm one.

the 180 mm crystal it is 21.86 MeV and for the 220 mm case it is 20.85 MeV. The simulation results agree with the measured data (chapter 6).

6 Data analysis

In this chapter the analysis methods for the γ and muon data are introduced and the results are presented. In addition, the basic properties of the detector are discussed. The reconstruction of the events is one of the main subjects of this chapter. The idea of the add-back algorithm and the event selection will be described in detail. Also, the efficiency and the size of the algorithm range will be defined as a benchmark for the algorithm.

Aside from this, the method of the particle identification will be presented. In addition, the results of the measurement with the CALIFA PETAL will be presented. In most cases experimental data and simulation data are compared.

6.1 Basic calibration of the detector

Detector calibration

Prior to the analysis the detector energy has to be calibrated. The detection units are calibrated with a ^{22}Na source. The calibrated values are fitted with a linear function:

$$\mathrm{E}_{\mathrm{calib}} = a_0 \times \mathrm{X}_{\mathrm{FEBEXch}} + a_1 \tag{6.1}$$

The average fitting parameters are: $a_0 = 9.80 \times 10^{-6}$ [keV/ch], $a_1 = 0.004$ [keV/ch]. This calibration is applied to the energy spectrum obtained in the AmBe measurement. Figure 6.1 shows the correlation between the FEBEX channel and the calibrated energy of a single crystal. The values were obtained from the nickel target measurement. The blue dots correspond to the following dominant gamma-ray energies: deuteron (2.23 MeV), ^{12}C (4.44 MeV) and the thermal neutron capture of ^{58}Ni target (8.99 MeV). The linearity of the data points is checked by the Pearson correlation coefficient (PCC) [Coh88]. It is a measure of the linearity of the correlation between variables x and y. It is denoted by the letter r_{xy}:

$$\mathrm{r}_{xy} = \frac{n\sum x_i y_i - \sum x_i \sum y_i}{\sqrt{n\sum x_i^2 - (\sum x_i)^2}\sqrt{n\sum y_i^2 - (\sum y_i)^2}} \tag{6.2}$$

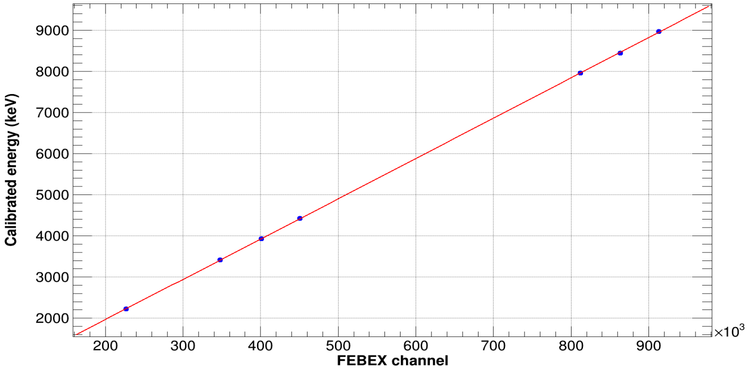

Fig. 6.1: Correlation of the calibrated energy with the FEBEX channel. The γ-rays stem from the AmBe source using a nickel target.

Here, n is the sample size, while x_i and y_i are the single samples indexed with i. The r_{xy}-value obtained in this work is 0.999. The result shows that the data points have a positive linear correlation.

Gain stability

The detector gain has to be maintained during the measurement. The gain stability of the detection units in the PETAL was checked in the AmBe measurement. The double escape peak of ^{12}C (E_γ = 3.41 MeV) was chosen to be the reference point. This is the case as in some spectra the single escape and full energy peak are not visible as distinct peaks. An example spectrum where the only full energy peak has lower statistics is shown (see Fig. 6.3: left). Another example is shown on the right where only the double escape peak is clearly visible while the other two are smeared out.

Figure 6.2 shows the gain stability of one crystal. To investigate this further the coefficient of variation (c_v), also known as relative standard deviation (RSD), is used to prove the stability. The coefficient c_v is defined as ratio of standard deviation to the mean value [ES98]

$$C_v = \frac{\sigma}{\mu}, \tag{6.3}$$

where σ is the standard deviation, and μ is the mean value.

For this measurement data were taken for around 30 hours. We divided the full

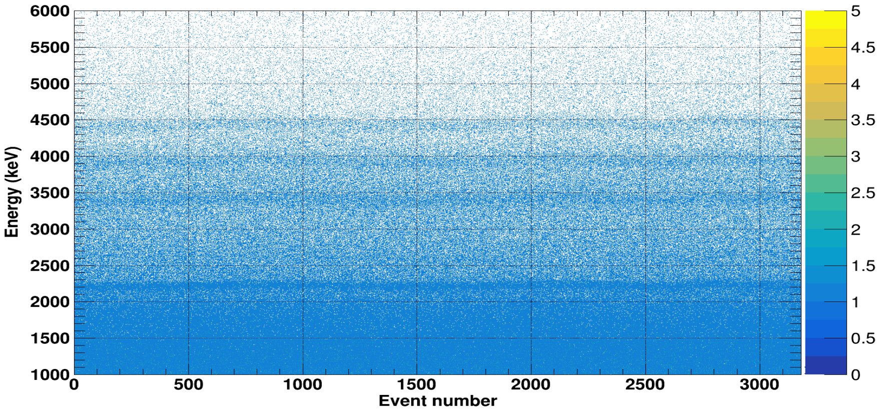

Fig. 6.2: Gain stability of a single crystal is shown.

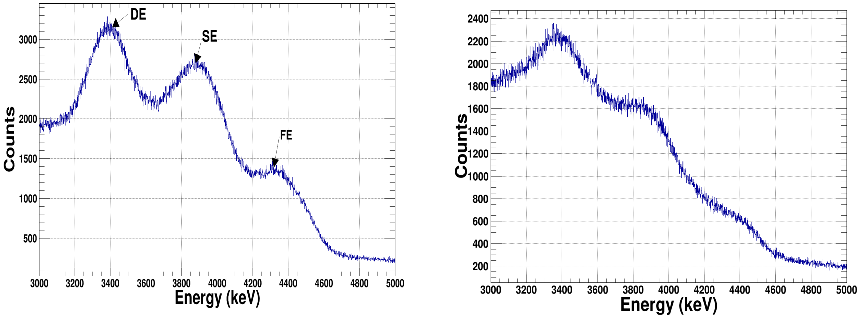

Fig. 6.3: Single crystal spectra. Left panel: Example spectrum of one crystal which detected full energy events only with reduced statistics. Right panel: Single spectrum with smeared peak for single escape and full energy events.

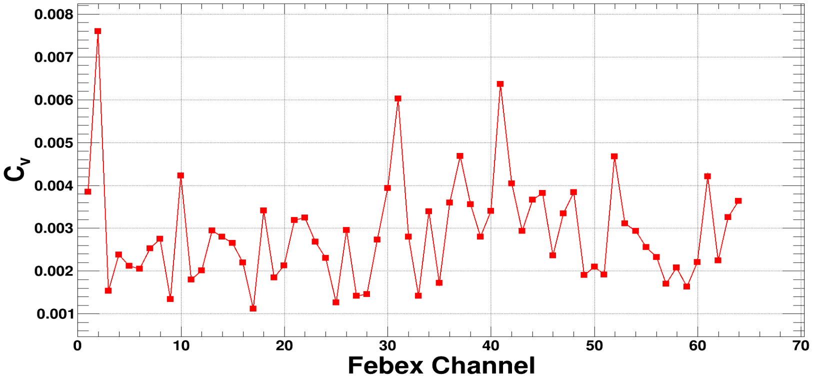

Fig. 6.4: Energy variation coefficient in all crystals in the PETAL.

data into sets of 100 million events for each single channel. For each of those 24 samples the mean value was calculated. One sample corresponds to data within 75 minutes. The energy variation coefficients are calculated with Eg. (6.3) and are shown on the y-axis of Figure 6.4. The x-axis corresponds to the 64 channels of the CALIFA PETAL. It shows the gain stability of all channels during the measurement. The coefficient of the variance of all channel is less than 1%. The result shows that the environment of the laboratory and the data acquisition did not affect the gain of the detection units.

Energy spectrum from the AmBe measurement in a single detecting unit

As first step the energy spectrum of each crystal in the range up to 9 MeV was investigated. If a certain energy is not detected, even though it is expected to originate from the used source, it points to a problem with the efficiency of the detector. Due to this some channels had to be excluded from the analysis. Figure 6.5 shows the energy spectrum of a channel which was used in the analysis. Various γ-rays are expected from the AmBe source. To emphasize each peak, the histogram is divided into two ranges: the low-energy range (up to 5 MeV: Fig. 6.5, left) and the high-energy range (5 MeV to 9 MeV: Fig 6.5, right). In the low energy spectrum several energy peaks show up. The dominant energies are 511 keV, 2.223 MeV (^{1}H(n,γ)^{2}H) and 4.439 MeV (^{9}Be(α,nγ)^{12}C). Also, their Compton edges are visible in the histogram. The 4.430 MeV γ-rays are used as a calibration source for the high-energy reactions and to test the reconstruction algorithm. The threshold of the detector is set around 200 keV. Additional targets are used to get high-energy

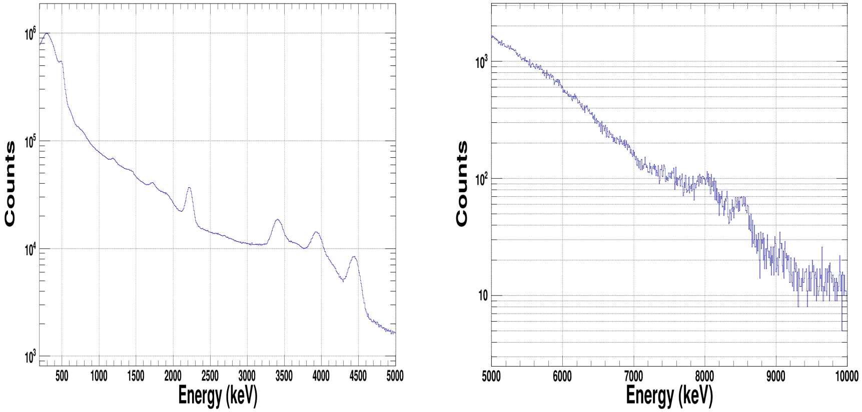

Fig. 6.5: Left: Energy spectrum of the AmBe measurement (lower energy range). Right: Energy spectrum of the AmBe measurement (high energy range).

γ-rays. In the high-energy range spectrum γ-rays from thermal neutron capture reactions are distinguishable; ^{58}Ni(n,γ)^{59}Ni (E_γ = 8.999 MeV). They will be used as one of the γ-rays to be reconstructed by an algorithm (section 6.3.2). The double escape peak of this reaction overlaps with the γ-ray from the other isotope of nickel; ^{60}Ni(n,γ)^{61}Ni (E_γ = 7.820 MeV).

Energy spectrum of muon measurement

The muons originated from the cosmic-rays have an energy of more than 4 GeV on sea level. These muons energy is not fully deposited in the CALIFA crystal. Their energy is partially absorbed in the crystals and they punch through neighboring crystals. In general, the deposited energy in the crystal can be predicted by using Eq. (6.4). It is related to the path of the incident muons. The average rate of energy loss of a particle with the kinetic energy E due to ionization [Pau71] is

$$-\frac{1}{\rho}\frac{d\mathrm{E}}{dx} = \frac{A}{\beta^2}[B + 0.693 + 2\ln\frac{p}{m_i c} + \ln\varepsilon_{max} - 2\beta^2 - \delta - U], \qquad (6.4)$$

Type	A [mm]	B1 [mm]	B2 [mm]	C1 [mm]	C2 [mm]
1	220.0	29.22	44.51	15.25	24.82
2	180.0	29.29	44.59	15.27	23.10
3	170.0	29.32	45.47	15.27	22.67

Table 6.1.: Dimensions of all crystal types in the CALIFA PETAL.

where A and B are constants dependent only on the medium. In the condition $p \ll m_i c^2/m$ and $m_{\ i} \gg m$, Eq. (6.4) can be approximated. The change rate is constant along the entire path length:

$$k = -\frac{1}{\rho}\frac{dE}{dx} \tag{6.5}$$

and is expressed in units of MeV/(g·cm^{-2}).
For the case of CsI, the absorbed energy is distributed like a Vavilov distribution [Vav57]. The distribution approaches the Landau distribution for x $\ll$ 1 and the Gaussian distribution for x $\gg$ 1. However, in most of the cases, considering the full distribution curve is not necessary. The most important quantity of the energy loss distribution is the most probable energy loss. The most probable energy loss of muons is 5.273 MeV/cm using the incident energy at sea level for the calculation (E_μ = 4 GeV) [Pau71]. The deposited energy is proportional to the path length in the crystal.
During the measurement, the crystals were placed horizontally with respect to the ground. In other words, the cosmic muon do not penetrate along the longest side of the crystal (A in Fig. 6.6). So the height of the crystals (B1, B2 in Fig. 6.6) is considered to calculate the energy loss in the crystal. Table 6.1 shows the dimensions of the crystals in the PETAL. Geometrically, the incident angle is also considered to calculate the path length in the crystal. The predicted path length is 2.922 cm to 5.804 cm.

The measured data is compared to the R3BRoot simulation. Figure 6.7 shows the comparison of the deposited energy. The blue histogram shows the measured data. The shape agrees with the simulation result, but the data are shifted to higher energies. The difference between simulation and measurement is caused by the fact that along A (see Fig. 6.6) cannot be exactly determined. Therefore the incident particles have to travel through a not precisely determined detector thickness. This creates the aforementioned shift. The path length in the crystal is calculated from the deposited energy. In the measured data, the deposited energy range is 21.74 MeV to 24.47 MeV, which corresponds to a path length of

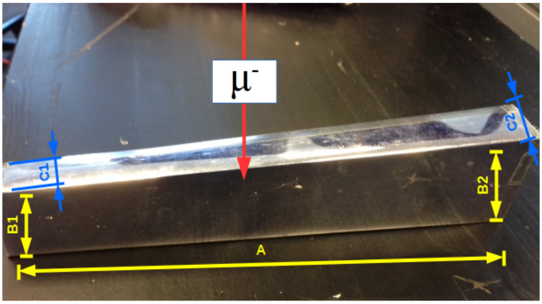

Fig. 6.6: Photograph of one of the crystals. The direction in which the muons hit the crystals is indicated.

41.17 mm to 46.41 mm. Most events have a deposited energy in the crystal of around 23.5 MeV, that corresponds to a mean path length of the particle through CsI(Tl) of 44.57 mm. In the simulation, the deposited energy range is 21.38 MeV to 23.74 MeV. The values correspond to a path length from 40.55 mm to 45.02 mm in CsI(Tl).

Energy resolution

The energy resolution is a basic and an intuitive property of the detector. Also, it is one of the quantities used to characterize detector. The resolution of a single detecting unit has to fulfill the requirement for a CALIFA barrel sector.

$$\text{Resolution } [\%] = \frac{\Delta E(FWHM)}{E} \times 100 \tag{6.6}$$

The energy resolution is measured with a ^{22}Na source. The γ-ray energy (E_γ = 1274 keV) is compared to the nominal specification of the CALIFA barrel. Figure 6.8 shows the energy resolution of the CALIFA PETAL. The CALIFA detection system carries out the role as a high-resolution spectrometer. The energy resolution is in this case the most critical parameter of CALIFA. This value has been set to be of $\Delta E/E < 6\%$ (for a 1 MeV γ-ray), which allows to distinguish most of the simple γ-ray cascades that come from the de-excitation of light exotic nuclei [R3B11]. The average energy resolution of a crystal is $6.01 \pm 0.77\%$, which is slightly worse than the requirement. Only five channels cause a worse average of the resolution. Apart from those, most of the channels meet the reference value.

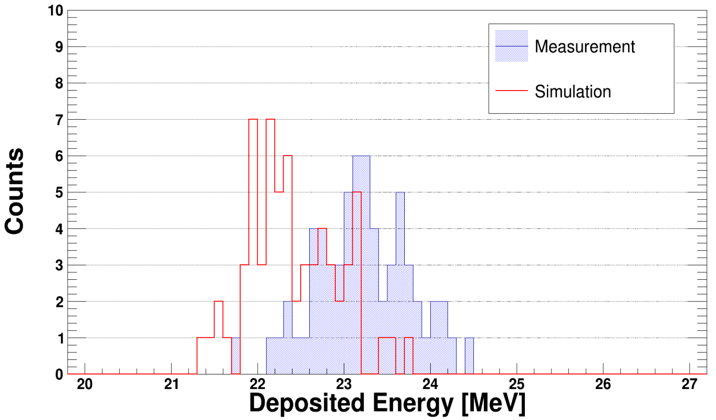

Fig. 6.7: Deposited energy in a single crystal. The red lined histogram shows the simulation result and the blue line histogram shows the measured data.

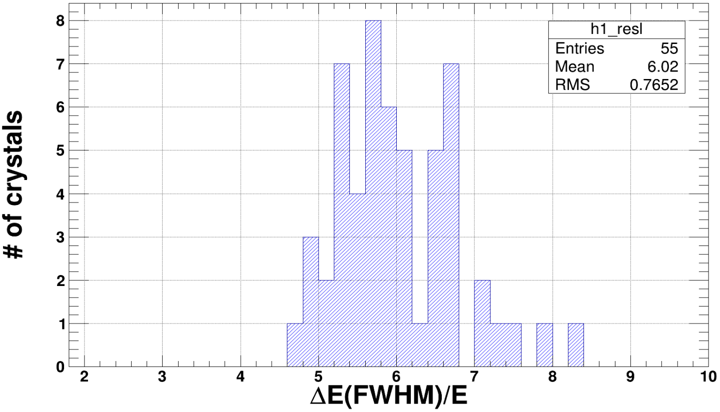

Fig. 6.8: Distribution of measured energy resolution determined with ^{22}Na (E_γ = 1274 keV) using 55 crystals.

6.2 Crystal mapping

This section shows the mapping of the working crystals in the CALIFA PETAL, the analysis of the data, and describes the reason for the elimination of a few crystals for the further analysis. During the preparation measurement several crystals were determined to be not suitable to use in the main measurement. The main problem with these crystals is related to the response of the detectors to the high-energy γ rays, i.e. that they cannot distinguish between energy peaks with an energy of > 4 MeV and background. An example illustrating such a detector response was already discussed in the last chapter (Fig. 6.3 right panel).

Note that the problem is not related to the gain stability of single crystals, but to the smearing out of high-energy peaks. If these were used in the main measurements it would cause an increased noise rate in the reconstructed events.

The CALIFA PETAL had been assembled before our measurements were done and had been used in several campaigns beforehand. That means that malfunctioning crystals can not be removed as it would destroy the coherence to previous works. Therefore we decided to keep the PETAL as it was and just exclude the data from these channels instead of removing crystals.

A list of malfunctioning crystals can be found in Table 6.2.

Type	ID.	Problem
1090.10.000.1105 (23×46×170 mm^3)	9	unstable gain
1090.10.000.1103 (23×46×180 mm^3)	17	low gain
	29	high-energy γ are not properly detected
	36	unstable gain
	37	double peak in high-energy region
	39	high-energy γ are not properly detected
1090.10.000.1101 (23×46×220 mm^3)	44	double peak in one energy area
	61	smeared data
	63	double peak in one energy area

Table 6.2.: The list of the excluded crystals.

Figure 6.9 shows a picture of the CALIFA PETAL. The division represents the position of all 64 crystals. The red squares mark the position of the excluded crystals. In total, 9 crystals were excluded. Two of them are positioned close to the AmBe source. There is no real positional pattern related to the excluded crystals. It is only noticeable that several crystals, which are placed on the bottom layer of the PETAL,

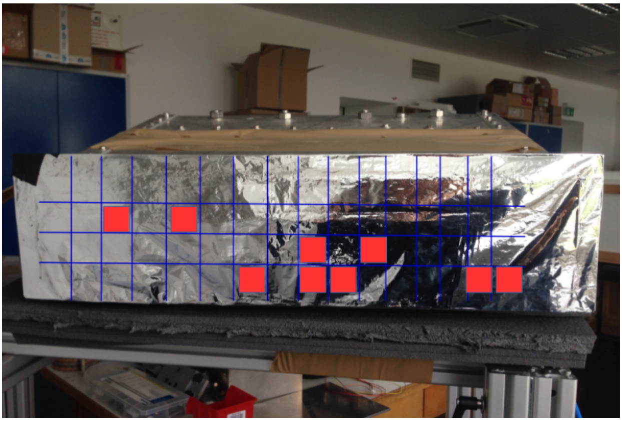

Fig. 6.9: The picture of the CALIFA PETAL, with all 64 crystals being indicated. Red marks signals excluded crystals.

are not working. They are all in a position with a lower probability of seeing γ rays from the source. Nevertheless, the other crystals in the bottom layer show a good performance through all energies.

6.3 Event reconstruction

In this section the results of the event reconstruction are presented. The method of the event selection is described, and afterwards the procedure of the add-back algorithm is explained. A way to check the performance of the algorithm is presented afterwards.

Event propagation

The particles in the scintillator can deposit their energy only partially and escape afterwards the volume. The CALIFA barrel is a segmented structure, so these escaped particles still have a chance to be detected in neighboring crystals. For that reason, the number of firing crystals is one of the interesting parameter. It corresponds to the propagation of the γ-rays and also other secondary particles. Each run has a different set-up for the measurement (see Table 4.1). This causes a difference in the hit patterns. Figure 6.10 shows the comparison of the cases. The amount of entries in the histograms was normalized. The left panel shows the comparison between using a nickel target and not using it. The blue histogram shows the measurement without a nickel target. In this case a γ-ray from the AmBe source

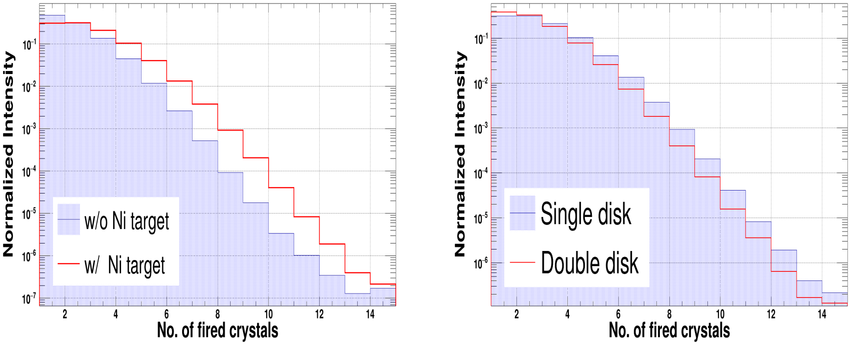

Fig. 6.10: Comparison of number of firing crystals. Left panel: the blue histogram shows the case without Ni target (run.2) and the red histogram shows the case with target (run.3). Right panel: the blue histogram shows the case one target (run. 3) and the red one shows the same with two targets (run. 5).

and a γ-ray from the reaction with the polyethylene (P.E) moderator is expected. Both energies are no higher than 4.44 MeV.

The red histogram shows the measurement with a nickel target. In this case there is a higher probability to get higher energy γ-rays. In fact, these γ-rays are not easily distinguishable from background (see 6.3.1 for details on how the background is determined). The histograms reflect the higher probability for multi-hit events in the range from 4 to 14 firing crystals. The right panel shows a comparison with different number of targets (see Table 4.1 for details on how the nickel targets were oriented). The blue histogram shows the result of using only one target disk. In this case the reaction surface is 14.52π cm^2. The red histogram shows the case of using two targets. Two target disks were used, which have the same disk shapes. The reaction surface is two times larger than in the previous case. In the range of 4 to 14 firing crystals, the counts in single-disk measurement are higher than in the double disk one. It can be predicted that increasing nickel target area enhances the probability of nickel capture processes, but at the same time the γ-rays from the AmBe source and the reaction with the moderator are scattered more often in the nickel target.

Run Id.	Average # of firing crystals
1	2.193
2	1.794
3	2.313
4	1.314
5	2.074

Table 6.3.: The average number of crystal fired in the given runs.

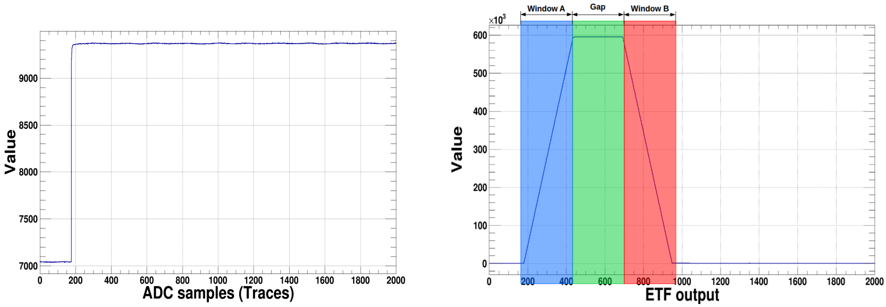

Fig. 6.11: The data trace of the input signal by the pulse generator without trapezoidal filter (left) and applied trapezoidal filter (right).

6.3.1 Event selection

It is required to define relating hits from the main events. The propagated events have to be distinguished from background events from the environment. For this work, the time information of the detected signal is necessary to connect related events. To obtain this information, the process of detecting a signal has to be modeled into the algorithm. FEBEX uses the trapezoidal filter (TF) to process the differentiated signal from the preamplifier [Jor+94; Rus+13]. The TF has two defined individual ranges for two purpose: a Fast Trapezoidal Filter (FTF) and an Energy Trapezoidal Filter (ETF) range. The FTF is first processes several samples from the signal trace. This is then used to decide if it is a triggering event. Whereas the ETF uses a relatively large number of samples. The energy value is obtained from this filter.

Figure 6.11 shows an example of the applied filter. One trace consist of 2000 samples. The data acquisition rate is 50 MHz. One sample corresponds to 20 ns. The total trace is 4 μs. The left panel shows the example trace from the pulse generator. An artificial trigger delay of 200 samples (400 ns) is applied. The right panel shows the output if the filter is applied to the testing signal (left panel). The filter output consists of three ranges. The first 256 samples are defined as "window A". This range corresponds to the increasing range in the trapezoidal shape. The next 257 samples are defined as "Gap" and correspond to the plateau range. The last 257 samples are defined as "window B". A total of 770 samples is used to extract the energy. Table 6.4 shows the used parameters for the two filters during the measurement with internal trigger.

	Window A	Gap	Window B
FTF	14	4	15
ETF	256	257	257

Table 6.4.: The used parameters of the trapezoidal filter.

FEBEX records the time information, that is the difference between the trigger point and the starting point of the each signal. Here, the trigger point of the amplitude of the signal has larger than threshold. Consider the following situation: A particle is detected in a single crystal and another event is detected in a neighboring crystal (see Fig. 6.12). Figure 6.12 illustrates the 64 crystals in PETAL. This way the trace ("Trace") and the time information ("t_adc") of each crystal is recorded.

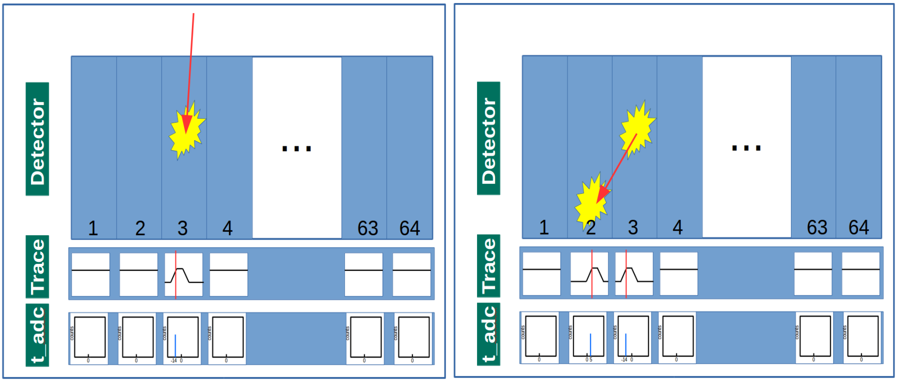

Fig. 6.12: Detecting one event in "detector 3" (left). Following event in "detector 2"(right).

Internal trigger mode

The "Internal trigger mode" uses the first fired channel as a trigger signal for all other channels. In other words, one channel has a signal, which is above the threshold. At the same time, the other channels are reading data, too.
When one channel (detector 3 in Fig. 6.12) has a triggering signal, 63 channels start reading data simultaneously. At this moment, the triggered channel has a time information. This value is extracted by the FTF. In this case, first 14 samples are used as window A and the threshold is checked at this point. So, this point is designated as t_adc = 0. As a result, the recorded time information of this crystal is "-14". The following events (Fig. 6.12; right, fired event in detector 2) also have time information. It is calculated between the triggering point of the first channel and the triggered time its own. This information can be used to relate the first hit with following hits. It makes it easy to distinguish the event, which is belongs to the reference signal, and noise.

External trigger mode

The "external trigger mode" used a trigger signal from the external trigger system. When the trigger detector has the signal, 64 channel start reading data. The time information is determined with the trigger time with respect to the starting point of the individual crystals.

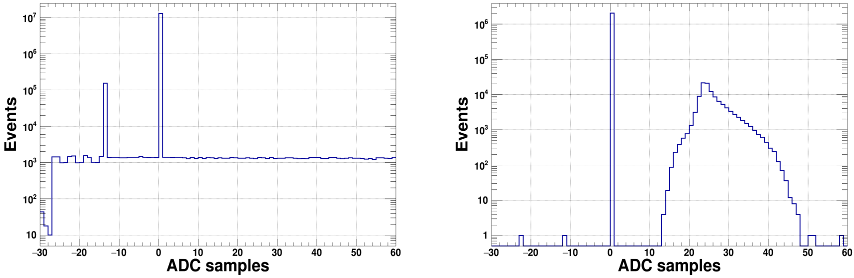

Fig. 6.13: Trigger examples. The time information (t_adc) of internal trigger mode (left) and external trigger mode (right) are shown.

Figure 6.13 shows an example of the time information from a single channel. The internal trigger mode (left) has two dominant positions -14 and 0. When the time information is -14, this crystal was the first fired crystal assigned. 0 means that the crystal has no signal. Obviously, a signal faster than -14 is a noise signal. On the other hand, signals later than the trigger point are candidates for related

events.
In the external trigger mode (right) events are distributed between 14 and 48. 14 corresponds to the start of reading the signal right after the trigger signal's arrival.

6.3.2 Reconstruction algorithm

In the reactions studied using CALIFA, one or more particles are expected to be detected simultaneously. In addition, low-energy background produced via bremsstrahlung in the target or other mechanisms will contribute to the detected hits in the detectors. Therefore, it is a mandatory to develop an algorithm for both γ-rays and protons. It will maximize the detection efficiency and resolution [R3B11]. The following sections will describe the reconstruction algorithm and how we defined some parameters for the quantitative analysis.

Add-back algorithm

The CALIFA group has previously developed a reconstruction algorithm, which was checked in simulations. The most basic approach to an algorithm for the reconstruction of γ-ray energies is to sum up the energy of all crystals in a selected angular region. Two different approaches were adopted when considering the angular region for the add-back algorithm; a circular window and a square window. The "circular window" method uses only one parameter, which is related to an opening angle of a cone. The "square window" method uses two parameters, which are related to the polar and the azimuthal angles. Both of them use their own parameters to define the size of the window, which is the angular region used to reconstruct events. In this work, we choose the "square window" method. As the CALIFA PETAL is a part of the full CALIFA barrel, the solid angles do not define the neighboring crystals in this windows properly. For this, the "square window" method is used. It can convert the physical angle to a relative angle, with the center of the PETAL as reference point.

Figure 6.14 shows the reconstruction process by the algorithm. Suppose the simulation of one event. As center of the first cluster the crystal hit with the highest deposited energy is chosen. All hits falling into the angular region around this center are assigned to this cluster. The deposited energies of all crystals in the cluster are summed to the reconstructed energy. After this procedure the crystal with the highest energy of the remaining hits is chosen as the next cluster center and the procedure is repeated until all hits above the threshold have been assigned to a cluster. Each cluster corresponds to one identified incoming photon. Our group has developed a second approach for a reconstruction algorithm with a new method to

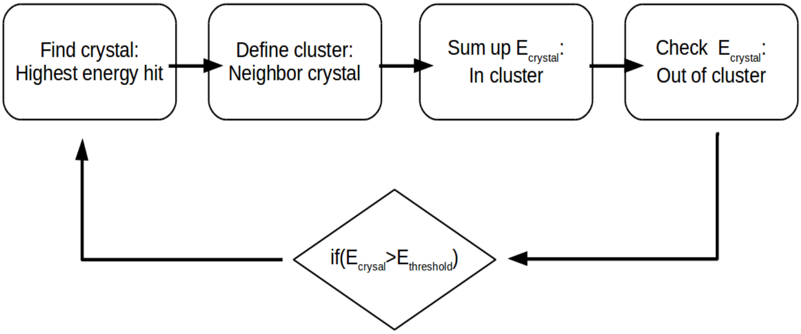

Fig. 6.14: Flow chart of the reconstruction algorithm.

define windows [Lut13]. The new method defines the cluster range using the type of crystal shape and the relative position of the alveolus. The CALIFA barrel includes different types of crystal shapes which are identified using the position of carbon fiber alveoli. These two parameters define the position of the crystals. Again suppose the simulation of one event. Here, the first cluster center is chosen and the algorithm saves this crystal's information, i.e. type of crystal shape (ID$_{type}$) and alveolus (ID$_{av}$). After this, the algorithm collects the related hits (neighbor hits). The neighbor hits have to fulfill the following conditions:

1. Above the threshold (50 keV).
2. In first layer neighbor: Difference of ID$_{type}$ and ID$_{av}$ between -1 to 1
3. In second layer neighbor: Difference of ID$_{type}$ and ID$_{av}$ -2 or 2

One alveolus has 4 crystals. If the hit propagates to a neighbor in the same alveolus, the difference of ID$_{type}$ and ID$_{av}$ is 0 in this case. This algorithm was beforehand only tested in a simulation, so in this work, it will be cross-checked with the measured data.
Both reconstruction algorithms, the square window reconstruction algorithm (algorithm 1) and the alveoli method (algorithm 2) were used.

6.3.3 Reconstruction ratio of the add-back algorithms

The measurement program with a nickel target provides high-energy γ-rays up to 9 MeV. This measurement is chosen to check the performance of algorithm 2. The

energy spectrum is divided into three energy ranges: low energy up to 2.5 MeV, intermediate energy from 2.5 MeV to 5.5 MeV (see Fig. 6.15) and high-energy range from 7.5 MeV to 9.4 MeV (see Fig 6.17). All histograms show the comparison of the energy spectrum without reconstruction and after the algorithm was applied.
The red histogram shows the energy spectrum before applying the reconstruction, and the blue histogram shows the reconstructed energy spectrum using algorithm 2. In the low-energy region ($E_\gamma < 600$ keV) the counts of γ rays decreases after the reconstruction process. These γ rays are related to primary hits. The energy spectrum for intermediate energy ranges is shown in Fig. 6.15: right. γ rays from de-excitation of $^{13}C^*$ lie in that region. Due to the size of the crystals in the PETAL single- and double-escape peaks can occur. These events can be reconstructed by the algorithm. The counts that cause the peak at the double-escape gamma energy decrease after the add-back process. Nevertheless, the reconstructed spectrum has still single- and double escape gamma peaks. Some crystals which are placed in the outer part of the PETAL cause an imperfect event reconstruction. The reconstruction ratio is calculated with following formula:

$$\text{ratio} = \frac{N_{\text{reconstructed}} - N_{\text{before Reco}}}{N_{\text{before Reco}}} \tag{6.7}$$

After applying the algorithm, the amount of double escape γ-rays was reduced by 4.74%. The γ-rays in the single-escape and full-energy ranges were increased by 9.64% and 32.54% , respectively. Table 6.5 shows the average ratio of reconstructed events in all measurement set-ups. Algorithm 2 was used.
For algorithm 1 the window size needs to be tuned to optimize the reconstruction process. The window size (i.e. polar-angle cluster size) is increased from 12° to 30° in 7 steps. Algorithm 2 has a defined reconstruction window as reference point: ID of alveolus, type of crystal shape, i.e., it has fixed values. To compare this to algorithm 1, the polar angle of the alveolus in the PETAL is calibrated ($21.7° \pm 1.5°$). The result of the reconstructed events in the 4.44 MeV peak with error bars on windows size is presented in Fig. 6.16. The blue graph shows the reconstructed ratio after applying algorithm 1. When the cluster window size is increased, the increase of the reconstructed events is checked. The red point in the graph shows the result of algorithm 2. The number of reconstructed events increased by 10% when increasing the window size twice. Algorithm 2 uses the alveoli as a defining cluster size. This value is converted to an angle. And the increment ratio of algorithm 2 is in agreement with the ratio curve of algorithm 1. The increase ratio of the reconstructed events represents the performance of the algorithm.

Figure 6.17 shows the energy spectrum of the γ-rays of the thermal-neutron capture reactions with the nickel target. The statistics is quite low. After applying

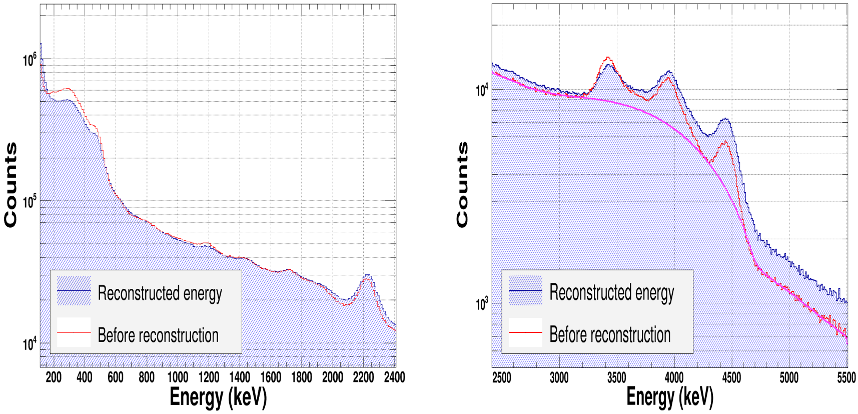

Fig. 6.15: Reconstructed energy spectrum of nickel target measurement in the low-energy range. Left panel: The energy spectrum of range 100 keV to 2.4 MeV. The red-lined histogram shows the energy spectrum of the single crystal, without the reconstruction algorithm being applied. The blue-lined histogram shows the reconstructed energy spectrum. Right panel: The energy spectrum in the range of 2.5 MeV to 5.5 MeV (same color code as left panel). The pink line shows the background of the red-lined histogram.

Energy range	Reconstructed ratio (%)
Double escape energy	-4.39±0.93
Single escape energy	10.51±0.40
Full energy	33.39±1.71

Table 6.5.: Average change in ratio of reconstructed events in the 4.44 MeV peak in all measurement configuration (see Table 4.1).

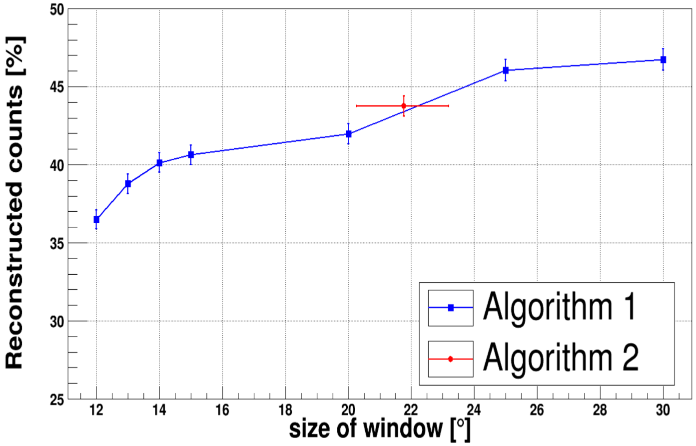

Fig. 6.16: Reconstructed events for the 4.44 MeV peak using different cluster windows sizes. The increase ratio of the full energy peak of 4.44 MeV γ-rays is shown. The blue line shows the efficiency of algorithm 1 and the red dot shows algorithm 2. The error bar corresponds to the angular range of the alveoli.

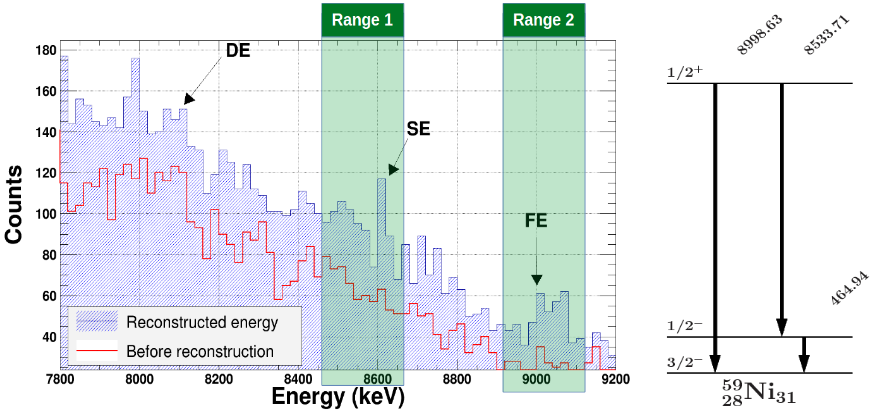

Fig. 6.17: Left panel: Reconstructed energy spectrum using algorithm 2 of the nickel target measurement in the range 5 MeV to 9 MeV. It has the same color code as Fig. 6.15. Right panel: Partial level scheme of ^{59}Ni [Nit].

Run Id.	Ratio of the reconstructed events (%)	
	Range 1	Range 2
3	50.43±3.44	53.22±7.17
5	43.79±1.93	69.21±2.87

Table 6.6.: Increase of reconstructed events from the thermal-neutron capture γ-rays.

the add-back algorithm 2, some events are reconstructed. In this case the single-escape peak belonging to the transition $1/2^+ \rightarrow 3/2^-$ (E_γ = 8.99 MeV) overlaps with the full-energy peak of the transition $1/2^+ \rightarrow 1/2^-$ in ^{58}Ni (E_γ = 8.53 MeV, see Fig. 6.17). The intensity of this line is 47.84% compared to the 8.99 MeV ground-state transition. Because of this reason, two energy ranges are considered individually; the smeared energy range with the single escape peak of the ^{58}Ni capture and the other transition of ^{58}Ni (range 1, $E_\gamma \simeq$ 8.50 MeV) and the full-energy peak of the ^{58}Ni target (range 2, E_γ = 8.99 MeV). After the reconstruction, counts in both ranges are increased. Table 6.6 presents the ratio between two different set-ups (run3, run5). The correlation between the reconstructed ratio and the cluster window size is calculated only for range 2. When the window size is larger than 24°, the amount of reconstructed events is twice as large as before.

6.3.4 Cluster size of the reconstruction

The cluster size of the reconstruction is the number of involved crystals during the reconstruction process. It is another parameter to ensure an efficient reconstruction algorithm. As a result, it can provide the optimal size of the cluster.

The number of involved crystals is compared using different reconstruction window sizes. The defining windows are the same as in the previous section. They are compared to simulation results. Figure 6.19 shows the comparison of the different algorithms. Each value corresponds to a different window size of the reconstruction area. The blue-dashed line shows the average cluster size of measured data, which is used by algorithm 1. And the red-dashed line shows the simulation data with the same algorithm. Pink and green dots in the graph show the cluster size of algorithm 2, measurement and simulation, respectively. The error bar presents the various angular ranges used by algorithm 2. The average cluster size of the simulation is 0.7 larger than the measured data. This difference is caused by the threshold set during the measurement. The threshold of the reconstruction algorithm in the simulation is 50 keV. It is obviously lower than the threshold of the measurement.

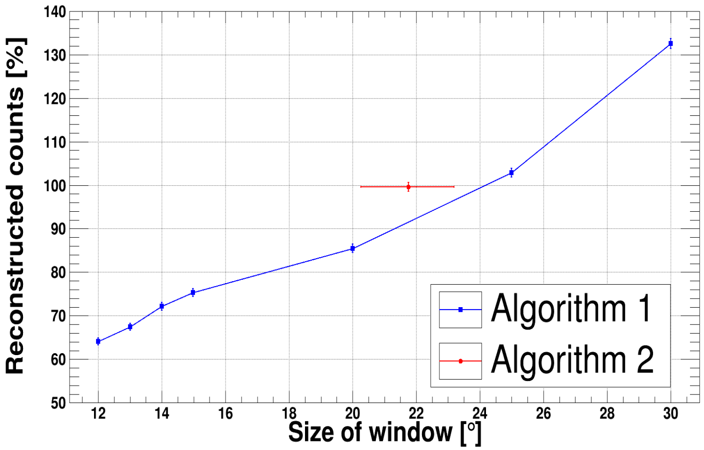

Fig. 6.18: Reconstructed events for different cluster window sizes in the 8.99 MeV peak. The blue line shows the increase ratio of algorithm 1 and the red dot shows algorithm 2. The error bar corresponds to the angular range of the alveoli.

In our measurement the threshold of each crystal was set to be around 300 keV. When the size of the window increases, the cluster size saturates and the difference between simulation and measured data is smaller than 0.3.

6.4 Efficiency

The detection efficiency of the CALIFA barrel has been one of the key requirements and a huge effort has been devoted to improve it in the calorimeter concept and design. The efficiency in detecting high-energy γ-rays can be increased by a reconstruction algorithm. In this part, the reconstruction of the efficiency is explained. It is showed in the performance reconstruction algorithm. The efficiency is defined as the following ratio:

$$\varepsilon = \frac{\text{Number of reconstructed } \gamma \text{ rays / the full energy peak area}}{\text{Number of total incoming } \gamma \text{ rays / the detector surface}} \qquad (6.8)$$

First of all, the number of photons emitted into the detector area has to be calculated to obtain the efficiency. In this part, the AmBe source is used. Its current activity can be calculated with the information in section 3.2.

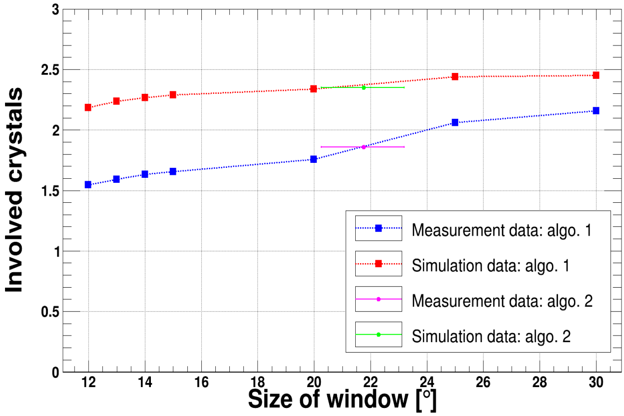

Fig. 6.19: The average amount of involved crystals in the measured data compared to simulated data. The blue (red) line shows the ratio of the average amount of involved crystals for algorithm 1 in the measurement (simulation). The pink (green) dots show the average amount of involved crystals for algorithm 2 in the measurement (simulation).

In the measurement set-up, the emitted γ rays from the neutron source penetrate the PE block. The monoenergetic photons with an incident intensity I_0 penetrate a layer of material with the mass thickness x and density ρ, and emerges afterwards with the intensity I given by the exponential attenuation law:

$$\frac{I}{I_0} = \exp\left[\left(-\frac{\mu}{\rho}\right)x\right] \tag{6.9}$$

Here μ/ρ is the attenuation coefficient. It is 3.44×10^{-2} cm^2/g for polyethylene and 3.08×10^{-2} cm^2/g for air [Hub82] at an incident energy of around 4 MeV. So far, the values were calculated assuming a point source.
Additionally, the geometrical efficiency has to be considered [Lé10]. This denotes the ratio of the number of photons emitted towards the detector over the number of photons emitted by the source. It only depends on the source-detector geometry.

$$\Omega_{rel} = \frac{\Omega}{4\pi} \tag{6.10}$$

In this case, the detecting area of the PETAL is a rectangular surface [Zal14]. Here, the solid angle of the rectangular surface is defined by the formula:

$$\Omega = (1 - f_s) \cdot 4 \cdot \arcsin(\sin\alpha \cdot \cos\beta) \tag{6.11}$$

$$\alpha = \arctan\left(\frac{w}{2d}\right) \tag{6.12}$$

$$\beta = \arctan\left(\frac{h}{2d}\right) \tag{6.13}$$

where w and h are the width and the height of detector surface, respectively, d is the distance between the source and the detector surface, and f_s is the fractional shadowing of the detector by any object or window support grid between the active area of the detector and the specimen.
Through all these steps, the denominator of Eq. (6.8) can be calculated

$$\mathrm{N}_{emit} = \frac{\mathrm{A}_{now}}{\mathrm{A}_{ref}} \cdot \mathrm{n}_{emit,n} \cdot \mathrm{R}_{E=4.43} \cdot \exp\left[\left(-\frac{\mu_{\mathrm{mod}}}{\rho}\right)x_{\mathrm{mod}}\right]\left[\left(-\frac{\mu_{\mathrm{air}}}{\rho}\right)x_{\mathrm{air}}\right] \cdot \Omega_{rel}, \tag{6.14}$$

showing the number of emitted γ rays (E_γ =4.44 MeV) per second. Here, A_{now}, A_{ref} are the activity of ^{241}Am now and at a reference date. $\mathrm{n}_{emit,n}$ is the neutron emission value and $\mathrm{R}_{E=4.44}$ is the R-value of the source (see chapter 3.2). The av-

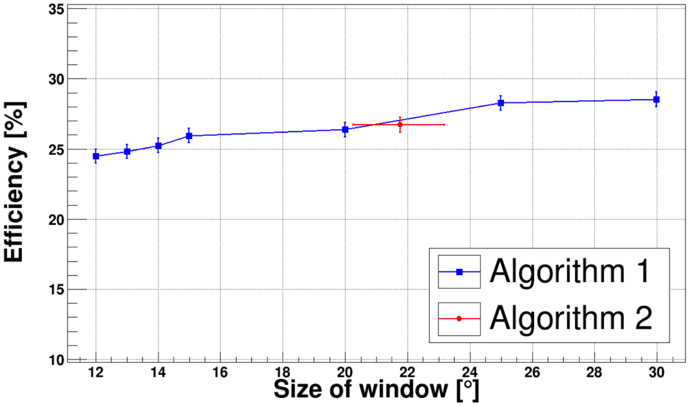

Fig. 6.20: The efficiency for the reconstructing events for different cluster window sizes is shown. The blue line shows the efficiency of algorithm 1 and the red dot shows algorithm 2. The error bar corresponds angular range of the alveoli (E_γ =4.44 MeV).

erage value of x_{mod} is 10.35 cm and x_{air} is 62.11 cm.

Again, two algorithms are compared. This work used the data of run 2, which did not use the nickel target. This measurement has a lower probability of getting the high-energy γ background. The full-energy peak of $2_1^+ \rightarrow 0_1^+$ the transition in ^{12}C is chosen as a source for the reconstruction.

Measuring time	Measured event
160435 s	7146862 events

Table 6.7.: Information on the measuring time (run 2) and obtained number of carbon events.

The same idea is used to obtain the efficiency of the algorithm (see Fig. 6.16). The efficiency of the reconstruction is calculated using reconstructed events and expected events from the calculation above. The efficiency of the algorithm is calculated with Eg. (6.8). It is an important parameter to optimize the reconstruction algorithm. The same criterium as before is used. In this work, we try to study this with measured data. The efficiency is calculated as the number of reconstructed events. It compares the two different definitions for a cluster. In the simulation, the maximum efficiency of 4 MeV γ rays is around 40% [AP+14]. In the measurement, the maximum efficiency is 29% (Fig. 6.20).

6.5 Particle identification

The particle identification is the process of using information of passing particles in a detector to determine their properties and to distinguish the different types of detected particles that have a similar energy. Several methods can be used to identify the charged particles: TOF measurements, Cherenkov counters, transition radiation detectors and multiple ionization measurements [Kle98].

The CALIFA barrel consists of CsI(Tl) crystals. The light output signal of CsI(Tl) has two exponential decay components. And those components show different response depending on the incident particle. The light output of these crystals can be used for particle identification [SJW58; SM01].

The CALIFA group developed a new digital algorithm for the online particle identification, called Reconstructive Particle IDentification (RPID). The algorithm is based on a model for the the scintillation light output and an exponential response function for the preamplifier. The underlying idea is to use different processing steps that modify the pulse shape in a way that allows to determine the amplitudes of the two main components directly [Ben10; Ben+13]. To implement this, the Field Programmable Gate Array (FPGA)-based electronics are required for the on-line particle identification. More details will be explained with a concrete example in the following.

Assume that a particle hits the scintillator, then the scintillation light of the CsI(Tl) can be divided into a fast component (N_f) and a slow component (N_s)

$$L(t) = \frac{N_f}{\tau_f} \mathrm{e}^{-\frac{t}{\tau_f}} + \frac{N_s}{\tau_s} \mathrm{e}^{-\frac{t}{\tau_s}}, \tag{6.15}$$

where τ_f and τ_s are the decay time constants of the fast and the slow scintillation component, respectively. The time constants are in the order of $\tau_f \approx 600 \sim 800$ ns, $\tau_s \approx 3.0$ - 3.5 μs [Val+93]. The light yield depends on the incident particle type due to quenching effects. So, the particle is identified by determining the ratio of the components amplitudes N_f and N_s.

This light is converted to an electric pulse by the APDs. Within the charge-sensitive preamplifier these pulses will be convoluted with an exponential decay.

$$U(t) = \int_0^t \left(\frac{N_f}{\tau_f} \mathrm{e}^{-\frac{t'}{\tau_f}} + \frac{N_s}{\tau_s} \mathrm{e}^{-\frac{t'}{\tau_s}} \right) \mathrm{e}^{-\frac{t-t'}{\tau_{RC}}} dt' \tag{6.16}$$

After the preamplifier signal is digitized by a sampling ADC, Eq. (6.16) converts to a digital time-discrete function. This process leads to two problems: Firstly, the exponential tail of the signal distorts the signal in case of pile up events. The preamplifier induces a ballistic deficit in the pulse height. The moving window deconvolution (MWD), that process the data stream, copes with this issue [GGL94]. It deconvolves the preamplifier's exponential decay response function. It shortens the signal, thus reduces pile up effect. In other words, the original charge function is reconstructed within defined windows.

This processed signal is used for particle identification. This signal is differentiated. From this step, the signal reflects the original luminescence signal

$$L(i) = \frac{N_f}{m_f} e^{-\frac{i}{m_f}} + \frac{N_s}{m_s} e^{-\frac{i}{m_s}}, \tag{6.17}$$

where i, m_s, m_f are multiples of the sampling interval t_s. Here, Eq. (6.15) converts to a time discrete function. Equation (6.17) can be divided into two independent terms by multiplying it by an exponential function of the slow component ($e^{\frac{i}{m_s}}$). The final step is to apply a second MWD to eliminate the remaining exponential function. The signal trace has two windows: linear slope (window 1) and constant offset (window 2). This light output signal is converted from the preamplifier's signal by processing all this sequence. Subsequently a step output function divides the signal into fast-component term and slow-component term.

$$\mathrm{F}(i) = \begin{cases} \frac{N_s}{m_s} \left(\frac{i}{m_{sf}} + 1 \right) + \frac{N_f}{m_f} & \text{window 1} \\ C_{win} \frac{N_s}{m_s} & \text{window 2} \end{cases} \tag{6.18}$$

where, $m_{sf} = \frac{m_s m_f}{m_s - m_f}$ and C_{win} is a constant related to the length of the window 1. The slope represents the slow component (N_s). The main goal of these procedure is to identify particles in the scintillator using a small part of the full trace.

This process has been applied to the AmBe source measurement, and the particle identification histogram has been obtained. Figure 6.21 shows the particle identification of AmBe source measurement. Most events are distributed in the area such

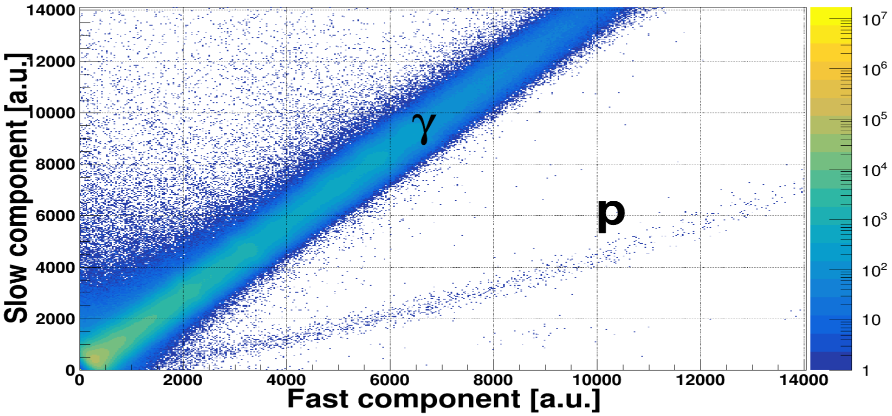

Fig. 6.21: Reconstructed slow component as a function of its corresponding fast component in the AmBe measurement, both in arbitrary units.

that the slow components are slightly larger than the fast components. Both γ-rays and punch through particles are expected in the scintillator. Whereas, some events have larger fast components with a small slow component, which is expected detecting proton from (n,p) reactions. Figure 6.22 shows the energy spectrum of the identified areas. The upper histogram corresponds to the proton events area. The particle energy is around 2 MeV. The histogram below corresponds to the γ-ray events area.

The measured data are compared to simulation data. To compare this, the ratio, which is between events in proton area and total events

$$R = \frac{(\text{events in proton area/full energy detected events})_{\text{measurement}}}{(\text{events proton area/full energy detected events})_{\text{simulation}}}, \qquad (6.19)$$

was used. This value is 1.63. The difference comes from the precision of the particle generation (see Fig. 5.3).

Figure 6.23 shows the same method applied to the muon measurement. Most detected events are $\mu^{\pm}$ and distributed in the area where the slow component is slightly larger than the fast component. Some events have larger fast component with small slow component, which is expected for protons and α particles. Figure 6.24 shows the energy spectrum of the identified areas. The top histogram belongs to the muon events area. This measurement used "internal trigger mode"

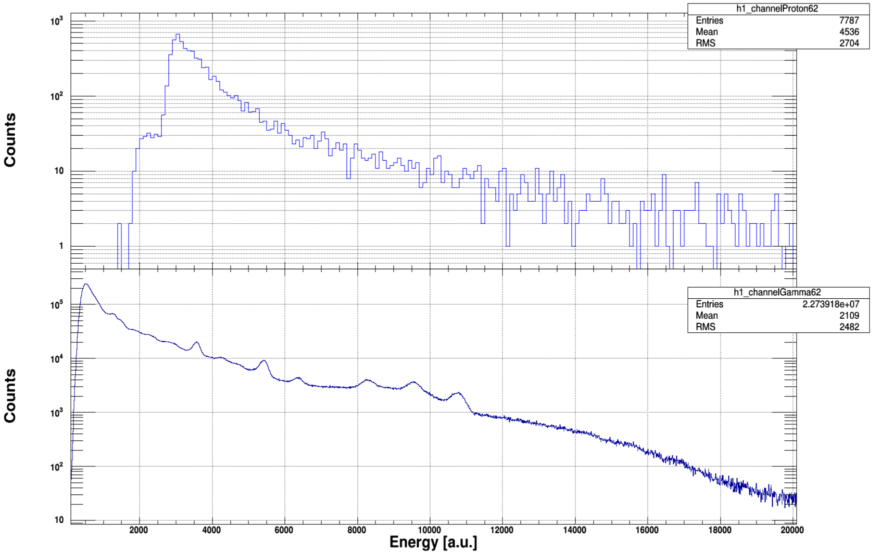

Fig. 6.22: Energy spectrum gated on PID in the AmBe measurement. Detected energy in proton events (top). Detected energy in γ area (bottom)

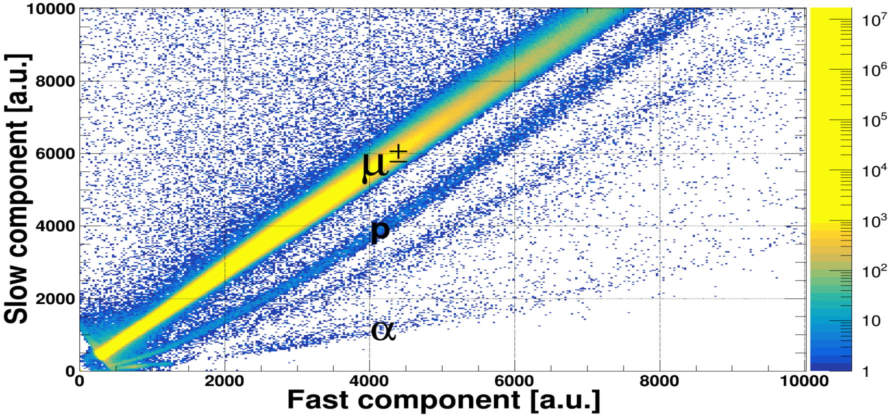

Fig. 6.23: Reconstructed slow component as a function of is corresponding fast component in the muon measurement.

without additional trigger detector (plastic scintillators). The deposited energy histogram differs from the Fig. 4.11. There are many background events, which are not triggered by the plastic scintillators (for example, secondary e^-). They are distributed in the lower energy area. The middle and bottom histograms correspond to the proton events area and alpha area, respectively.

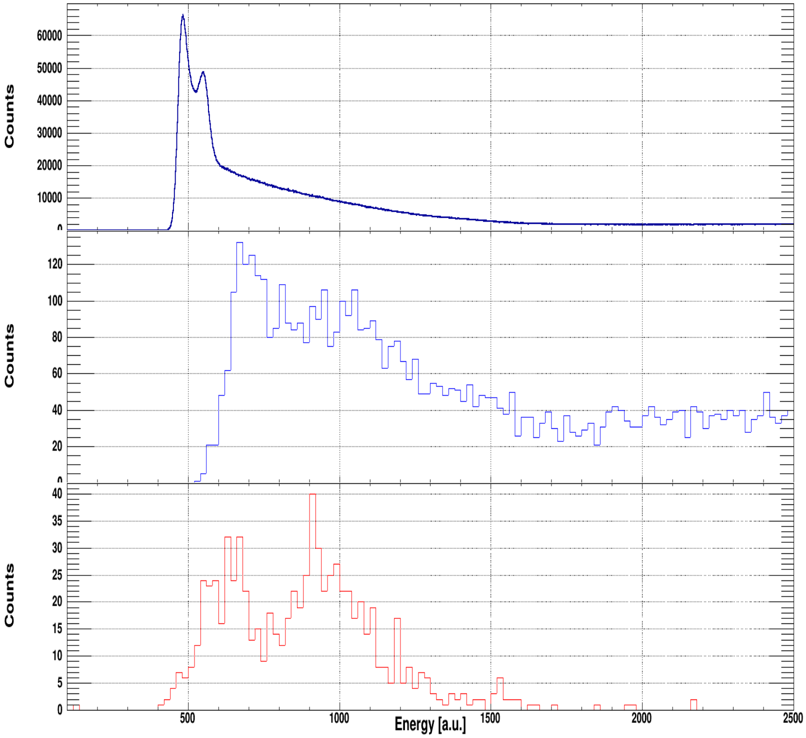

Fig. 6.24: Energy spectrum gated on PID in the muon measurement: detected energy in muon events (top), detected energy in proton area (middle), detected energy in α area (bottom).

7 Conclusion

In this work, I have tested the CALIFA PETAL response to different types of radiation: γ rays and fast neutrons from an AmBe source and thermal neutron capture with a nickel target, muons from cosmic rays and fast neutrons. This campaigns have been done in the laboratory at the IKP, TU Darmstadt.
Firstly, the basic properties have been checked. The response to different types of incident particles of each detection unit has been checked. Several γ energies up to 9 MeV were used: 1275 keV from ^{22}Na, 2223 keV from the reaction of polyethylene moderator with neutrons, 4439 keV from the AmBe source and 8999 keV from the thermal neutron capture of a nickel target. Also the gain stability of the output signals has been checked over around 30 hours. This factor was verified by calculating the coefficient of variation (c_v). The average value of all channels is 0.0029 ± 0.0012, which means the gain of the PETAL is stable. The energy resolution is one of the most important parameters when CALIFA is operating as a spectrometer. The average energy resolution is 6.01% ± 0.77% at 1275 keV and is close to the requirements of the CALIFA barrel. In the muon measurement, the energy spectrum is calibrated with 4.44 MeV gammas using the low sensitivity mode of the MPRB-16 preamplifiers. The measured data is compared to the simulation data. The average deposited energy of the single crystals is 23.23 MeV ± 0.60 MeV in the measurement and 22.44 MeV ± 0.68 MeV in the simulation. This means that the 4.44 MeV γ-rays can be used as a calibration source of the high-energy area of the spectra also in future experiments at GSI/FAIR.

The reconstruction of γ-ray hits is needed as especially high-energy γ rays do not deposit their full energy in a single crystal. The reconstruction of events has been tested with two high energy gammas (4.44 MeV and 9 MeV). First of all, the related hits in the PETAL need to be selected. The time information of the signal in FEBEX is used to distinguish between related hits in the same event and the background. Especially in the "Internal trigger mode", this information is useful to connect the hits for the reconstruction. In this case, the time between the triggering point of the first signal and the trigger time of the other channels is calculated. After the selection of the events, the reconstruction algorithm is applied to these selected events. I have tested two algorithms: one that uses the square window method and one that uses the alveoli method. The square window method uses the polar angle and the azimuthal angle of the crystal to define the boundary for the reconstruction of events. In this work, I increased the size of the windows to check its performance. The alveoli method uses the ID of the alveoli to define the boundary for the reconstruction of events. To compare the two methods, the reconstruction ratio, the number of involved crystals and the efficiency are considered. The reconstruction window size of the alveoli method corresponds to 21.7° ± 1.5°. In the square-window method, the reconstruction ratio, amount of involved crystals and efficiency saturate when the reconstruction window is larger than 25°. In other words, the reconstruction window is not necessary to be larger than 25° to optimize the algorithm. The alveoli method covers the window size around 22° and its results agree with the one of the square-window method. So, it is also good enough to be another option to reconstruct events.

The AmBe source emits fast neutrons of energies up to 10 MeV. These fast neutrons cause (n,X) reactions in the CsI(Tl) crystal. In which, charged particles (p, α) are produced. They can be distinguished using their unique pulse shape in the detection units. I used these reactions to verify the RPID method for CALIFA. In the measurement, the particles are identified well and also agree with the simulation data. CALIFA can act as a neutron detector, as well. The direct illumination with protons has been done before with the experiment. In this work, the RPID method is used to identify secondary particles for the first time. The secondary particles in the muon measurement are identified with this method, too.

Lastly, the result of the R3BRoot simulation agrees with the measurements. It was developed to cover the full experimental program with CALIFA. Through this work, R3BRoot shows the possibility to simulate various physics programs apart from the main physics program of CALIFA. The members of the data structure (e.g. N_f,N_s in the "CaloHit") reproduce real data nicely. They can be used to obtain much information from the simulation.

8 Development of a quality assurance test stand for APDs

In this chapter, the quality assurance test stand for CALIFA APDs will be introduced. The quality assurance (Q.A) test for each component has to be done before the construction of the full CALIFA detector. In this project, we have developed the test bench and proved its functionality. Afterwards, the result of the calibration measurement and an example of the quality assurance test will be presented.

8.1 Quality assurance test stand

The CALIFA barrel consists of CsI(Tl) scintillating crystals and double avalanche photo diode (APD) as detecting units. Before assembling the detection units, a precise study of their individual parts has to be done. This project aimed to develop the quality assurance test stand for the APDs and to provide information to characterize the individual units. Figure 8.1 (left) shows a photo of the system. The test stand provides controlled temperature for the APDs and supplies an input signal to check the performance.

8.1.1 Design of quality assurance test stand

The main goal of the quality assurance test stand is to provide controlled conditions for testing the APDs and to measure the variance of the output. For this work, the test bench has to control two main parameters: bias voltage and temperature [Mos+02]. The bias voltage is controlled by the Mesytec MPRB-32 preamplifier. The MPRB-32 allows to adjust the bias voltages up to 600 V. The typical break down voltage (V_{BR}) of a Hammatsu APD (S8664 series) is around 400 V.
Temperature control is the main task of this project. A straightforward way to control temperature is heat convection, i.e. to control the temperature in a closed space by using an air flow. The disadvantage of this method is that it is hard to control the temperature variation of each APD. The temperature control system uses a Peltier unit for the determination of the temperature.
The Peltier effect is the appearance of heating or cooling at an electrified junction of two different conductors and is named after French physicist Jean Charles

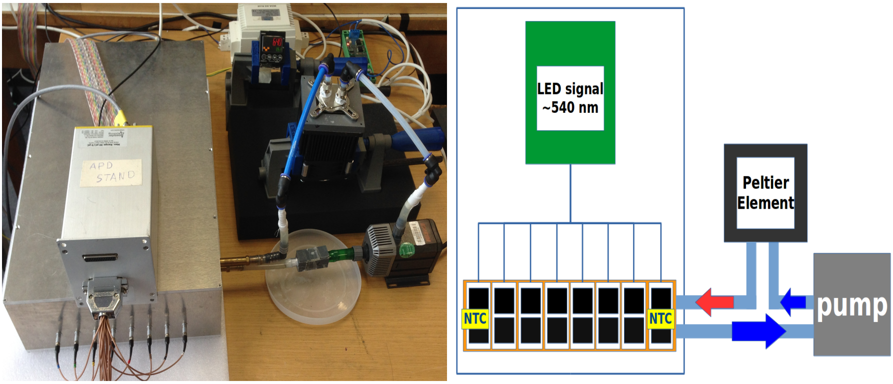

Fig. 8.1: Left photo: Full APD test bench. The left side shows the boxes in which the preamplifer, the APD test bench and the LED source are situated. On the right side the temperature controlling part (the temperature controller and the circulation pump) are shown. Right: Schematic view of the the test stand.

Athanase Peltier, who discovered it in 1834. The Peltier unit uses the Peltier effect to create a heat flux between the junction of two different types of materials. It can be used either for heating or for cooling. The main application in practice is cooling [TS08]. A typical Peltier heat pump device involves multiple junctions in series, through which a current is driven. Some of the junctions lose heat due to the Peltier effect, while others gain heat.

When designing the Q.A. test stand, it was considered to make a simple structure which is easy to handle and to make it compact. The advantage of using the Peltier unit is that we can build a compact system. The heat processing unit's dimensions are $90 \times 90 \times 97$ mm^3. Another essential part of the system is the pump, which delivers water to the system. The liquid moves into the copper channel and controls the isothermal state of the system. The details of these parts are presented in the following section. Figure 8.1 (right) is a schematic view of the quality assurance test stand.

Temperature controlling parts

As mentioned above, the temperature in the system is controlled by the Peltier unit. The Peltier kit has a Peltier unit, a heat sink, a fan and a thermistor. The size of the Peltier unit is 40×40 mm. The original kit worked with a PT-100 thermistor and was modified to work with NTC-thermistor by the electrics workshop in the

TU Darmstadt.

The temperature controller of the system has a compact size (48×48×79 mm^3) and a LED panel to monitor the process. The controller connects to the PC via a USB-serial port, so it can communicate with the DAQ PC. It controls the temperature with 0.003°C precision.

The liquid flow is controlled by the water pump. The pump circulates the water at a speed of 300 ml/h. 20 ml liquid are used in total in the system. The circulating water from the pump goes to a water block, which is attached to Peltier units. The water block is the watercooling equivalent of a heatsink. It is usually used on the computer components. In this system, it can be used to deliver a controlled temperature from the Peltier to the test bench.

APD test bench

The APD test bench is the place to put the APDs during the measurement and to manage the temperature from the temperature controlling part. The test bench is made of copper. The copper has a thermal conductivity of 401 W/(m·K). This is second highest value in metal [PHL66]. The copper plate's length is 220 mm and has a thickness of 10 mm. It has two holes, which supply the setup with liquid. The flow of the liquid is shown by arrows in Figure 8.1 (right). 8 APDs can be tested in one group simultaneously. The temperature of the APDs at the edge of the test bench is read by NTC thermistor. The APDs are attached to the copper plate with a thermal pad to improve the thermal coupling. The APD test bench is covered with a plastic case to isolate it from the room temperature. The cover has 16 holes to get the input LED signal with optical fibers to the setup. Each hole is pointing to the active area of one APD (Fig. 8.2: right).

LED source

The LED source provides input signals for the APDs. The green LED, that has maximum wavelength of light emission at 520 nm, is chosen to mimic the signals of the CsI(Tl) crystal. The LED has a forward voltage (V_F) of 3.2 V with the forward current (I_F) of 20 mA. The luminous intensity is 9600 mcd. The radiation opening diffusing angle is 30°.

The LED signals are distributed by a diffusing material (opal glass, thickness: 2.5 ± 0.3 mm) through a 50 mm cylinder ($\oslash = 25$ mm) to reach the optical fibers. The optical fiber connects the APD test bench frame to a point of the active area of APDs. Each active area of APD has an individual input source to check the performance. The LED source is controlled by a voltage output signal from the pulse generator (BNC Pb-5) via a lemo connector.

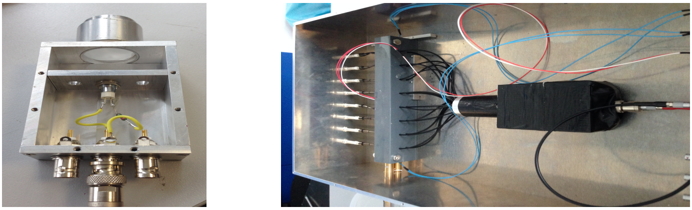

Fig. 8.2: Left panel: Interior of the LED box. The diameter of the diffusing glass is 25 mm. Right panel: View of the interior of the test stand. The black box is the LED source which is connected to the test bench via an optical fiber.

The uniformity of the LED source has been tested as a preparation measurement (section 8.2.1).

Temperature data

The on-line temperature information can be used as a starting signal for the temperature controller and is also recorded in the data base. It is necessary to convert the resistance of the thermistor to the temperature values.
The resistor value is converted using a resistivity to voltage converter (R2U box), which was developed at the electrics workshop at the IKP, TU Darmstadt. It produces a stable current and provides an output voltage signal. It has the voltage range 0 ∼ 1 V, which corresponds to the input range of FEBEX, and the values correspond to the temperatures 0 ∼ 30 °C. The converted values are recorded through a FEBEX board and are stored in a root tree with the gain values of each APD. There is a second R2U box in the system.
In this work a negative temperature coefficient (NTC) thermistor is used as thermal sensors of the system. The NTCs have several advantages: precision measurement, miniaturization, fast response and insensitivity to other factors (like pressure or magnetic fields). The temperature value is derived from the Steinhart-Hart equation [SH68]

$$\mathrm{R} = r_\infty e^{\frac{-B}{T}} \tag{8.1}$$

where, $r_\infty = R_0 e^{\frac{-B}{T_0}}$, R_0 is the resistance at T_0(298.15 K) and

$$T = \frac{B}{\ln(\frac{R}{r_\infty})} \tag{8.2}$$

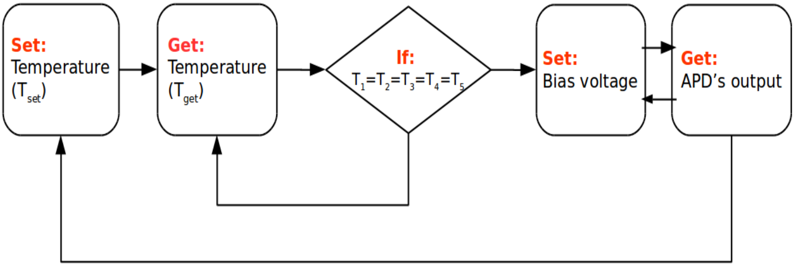

Fig. 8.3: Flow chart of the [work] process.

8.1.2 Working procedure

The CALIFA group declared that the operation temperature of the APDs is 18° ± 1°C and that the safe operation temperature range is from 15 to 30°C. Also, Hamamatsu APD have a reference value, tested at 25°C by the manufacturer. Hence, the target range of the test is designed to be between 15 °C and 25 °C. The APD test bench has to check the performance in the configured temperature range. The configured temperature range is divided in 11 steps with 1°C distance. To get the gain characterization, at each temperature step the gain is measured with increasing bias voltage. The bias voltage range is from 50 V to 375 V (25 V steps). The work flow is described Fig 8.3. The first step is to set a target temperature in the temperature controller. A Peltier unit starts heating/cooling to get the given value. The temperature value is read by the DAQ PC. The system reads the temperature values every 5 seconds. The next step is to estimate the temperature stabilize the system. It will make a decision once it has 5 samples of the temperature values. When they have the exact same value (with 0.1% precision), it declares the stable system temperature. When the system is stable, MPRB-32 supplies the bias voltages to the APDs and starts the measurement with the LED source. It will go higher up to a maximum value of 375 V. The last step is to ramp down the bias voltage and to set the next temperature.

The temperature controller, the preamplifier and the pulse generator are connected to the DAQ PC. It is possible to communicate via remote control bus. So, it can be controlled in one bash script file. The quality assurance test is therefore an automated process.

8.2 Quality assurance test of APDs

8.2.1 Preparation measurement

The quality assurance test stand is divided into two parts; the performance checking part and temperature controlling part. The performance check is tested with the LED signal. It has to prove the uniformity of the input source. The temperature controller has to check the operation of the temperature converter (R2U) and the performance of the temperature controlling parts.

Uniformity of the LED source

The LED source contains one LED unit, and the emitted light has a specific forward angle. First, the spacial uniformity of the LED light pulses was checked. The light coming from the point LED source is distributed with a diffusing opal glass. A special device was designed to check the uniformity at the connecting position of the optical fiber. It can move across the middle line of the surface with a precision in the order of millimeters. It measured 18 points (-9 mm to 9 mm). Each with three difference setups; without diffusing glass, one diffusing glass (right next to LED source) and two layers of diffusing glass (one diffusing glass; next to LED source, the other one in 25 mm distance from the first layer).

Figure 8.4 shows the device and the result of the uniformity measurement. The green dots show the case without diffuser, the red dots are with one layer of diffuser and the blue dots are with two diffusers. The results of each case are normalized using the maximum point of each data set. Except for the case without diffuser, it distributes the signal with only 10% variation.

Using this result, it is sufficient to use one layer of opal glass to make an uniformly distributed signal. The input pulser voltage has to be increased when two layers of opal glass are used. This situation restricts an input voltage and makes it hard to control an input signal at different temperatures with different gains.

Calibration of the R2U Box

The R2U box, produced at the electronic workshop at the IKP (TU Darmstadt), converts the resistance to a voltage value. These voltages simply correspond to temperature values. The thermistor has to be calibrated with the known resistors. 5000 kΩ, 6000 kΩ and 7000 kΩ, which correspond to 25.0°C, 21.0°C and 17.7°C, respectively. This formula is fitted to

$$\mathrm{T} = \frac{a_0}{\exp(b_0 \cdot x)}, \tag{8.3}$$

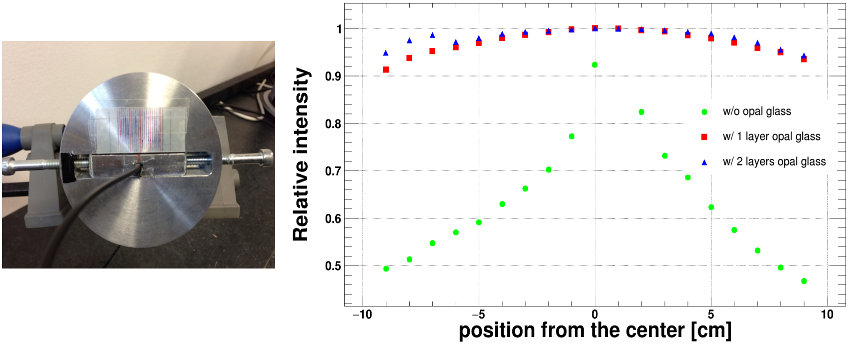

Fig. 8.4: Uniformity test with defusing material. The left side shows a picture of the device. The right side shows the result.

which is derived from the Steinhart-Hart equation [SH68].

Time consumption

The time consumption is an important property of the quality assurance test stand. It describes how fast a desired temperature can be reached and stabilized. The first measurement, which describes this process, is the time between each temperature step until the temperature is stabilized (Fig. 8.5: left panel). The second measurement is the time to change the temperature from the minimum (15°C) to the maximum (25°C) time until the temperature is stabilized (Fig. 8.5: Right panel). It is the case how fast after a complete measurement a new measurement can be started.

Decreasing the temperature needs twice as much time as increasing it. The temperature change from 14.9°C to 15.86°C needs 55 s to increase and 110 s to decrease. And the temperature change from 14.9°C to 24.58°C uses 148 s to increase and 291 s to decrease.

8.2.2 Gain measurement

The gain curve is another main characterization parameter of the APDs. The APD gain depends on the reverse-bias voltage and the internal properties of the photodetector [Eig+06]. In order to obtain the exact gain dependence, the APDs are tested in the APD test stand. Figure 8.6 shows one example of a gain curve of a APD. It is divided into two parts. The low-gain voltage range (75 - 150 V) is the

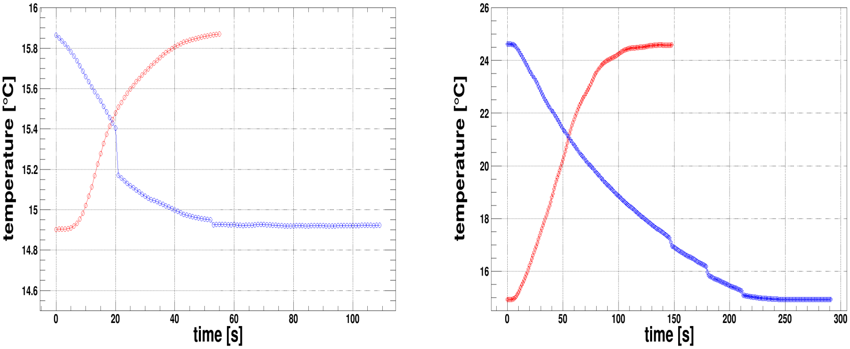

Fig. 8.5: Temperature units performance test. Left panel: Measured temperature stabilization set to 1°C step. Right panel: set to 11°C in one step.

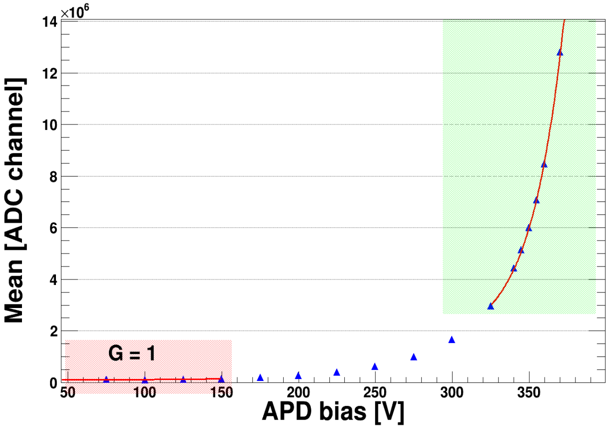

Fig. 8.6: The graph shows the output of APD and fit function which gives access to the parameter for gain determination.

plateau, approximately, when the gain value is $G=1$. On the contrary, the high gain range shows increasing gain in exponential order, that can be utilized to obtain a second gain value ($G = 50$). In this case, the gain curve fit comprises two parts. The APD gain is calculated with the formula [San14]:

$$\text{Mean}_{ADCch.} = c_0 + c_1 \cdot \exp(V/c_2) \tag{8.4}$$

The fit values are used to calculate the bias voltage for the specific gain.

8.2.3 Quality assurance test

In this section, a example data set from the quality assurance test is presented. Measuring over the full temperature range, the following information can be extracted: the gain value, the energy resolution and the calculated bias voltage for the respective gain (=30,40,50,60). It also provides possible temperature changes during the measurement. In the previous section (section 8.2.1), the speed of temperature changes has been shown. In addition, the stability of the temperature is an interesting point of the measurement. It can vouch for the reliability of measured data. The left panel of figure 8.7 shows the temperature data at 25°C. The absolute value has an offset. The important point here is that the temperature stays constant, i.e. within a range of 0.003°C during the measurement.

The next part, which is discussed, is the gain curve of each APD. The result in the center panel of Figure 8.7 shows the calculated gain value at 25°C. The gain parameter is extracted from Equation(8.4). The resolution (FWHM) of the APDs can be calculated simultaneously. The resolution is relatively bad until bias voltage reaches 200 V. This is because the APD gain is not high enough to distinguish LED signals from noise. After taking data for all temperature values, a relation connecting the gain value to the temperature can be made. The temperature coefficient of the APD is defined as the derivative of the bias voltage as function of temperature at gain $G = 50$ (Fig. 8.8). It can be utilized for the gain correction in case of an external temperature change.

8.3 Analysis of APDs

Separately from the previous section, the analyzed data of all APDs, which are tested with the Q.A. test stand, will be presented here.

It is interesting to compare the variance of the extracted nominal voltage of APDs to the value provided by the manufacturer. The nominal voltages are defined by the manufacturer and correspond to a gain of 50 at 25°C. Figure 8.9 shows the

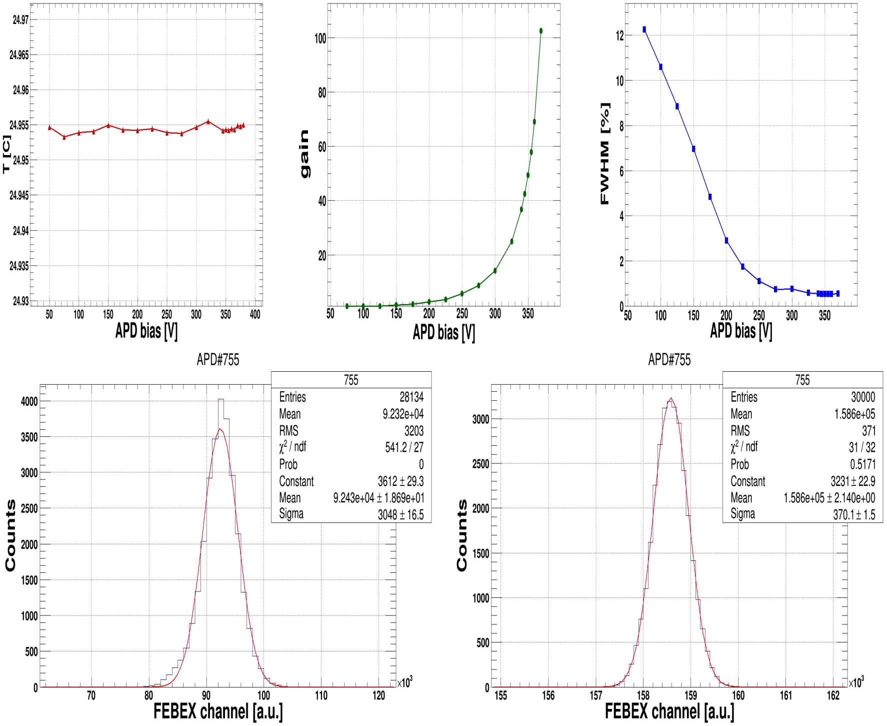

Fig. 8.7: Example spectrum of the Q.A. test. Upper panels: Recorded temperature. The nominal temperature is 25°C (left). Gain measurement (center). Energy resolution of APD over voltage (right). Lower panels: measured LED signal with bias voltage of 150 V (left) and 325 V (right).

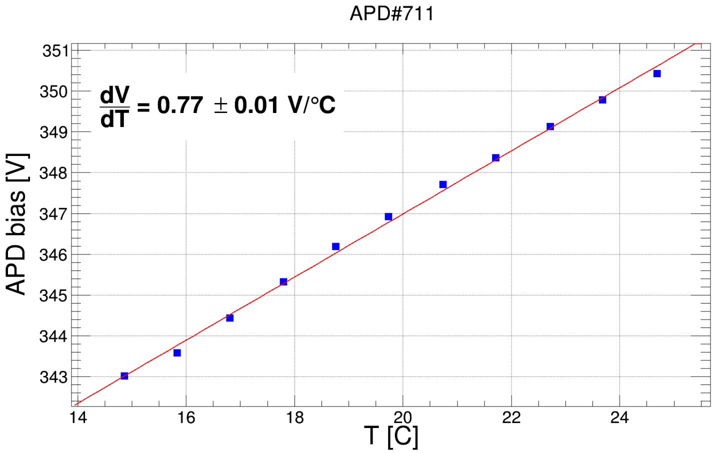

Fig. 8.8: Temperature coefficient for APD gain 50.

comparison of the nominal voltages. The measured data agree with the reference value. However, there is some offset visible in the graph. It is assumed that the difference comes from the precision of the temperature of the measurement environment.

It is one of the main purpose of this work to get the temperature coefficients of the APDs through the test. The temperature coefficient can be used to compensate the gain caused by a temperature change. So far, the CALIFA petal has only one unit to compensate the gain change caused by the preamplifier. Mesytec defines the optimum value of the temperature coefficient for the large area APD as 0.84 V/°C. Figure 8.10 shows the relation between temperature coefficient and nominal voltage. It also calculated the Pearson correlation coefficient (r_{xy}) to vouch the linear relation between the value. The coefficient is 0.895. The temperature coefficient of the APD correlates with the nominal voltage. And most of the coefficients, with a nominal voltage below 375 V, are within the optimum value by Mesytec and reference from manufacturer (0.78 V/°C, Hamamatsu S8664-1010 APD).

The tested APDs can be divided in 4 groups, depending on the nominal voltage range. The two groups, which have nominal voltage higher than 380 V, tend to be sensitive to temperature change.

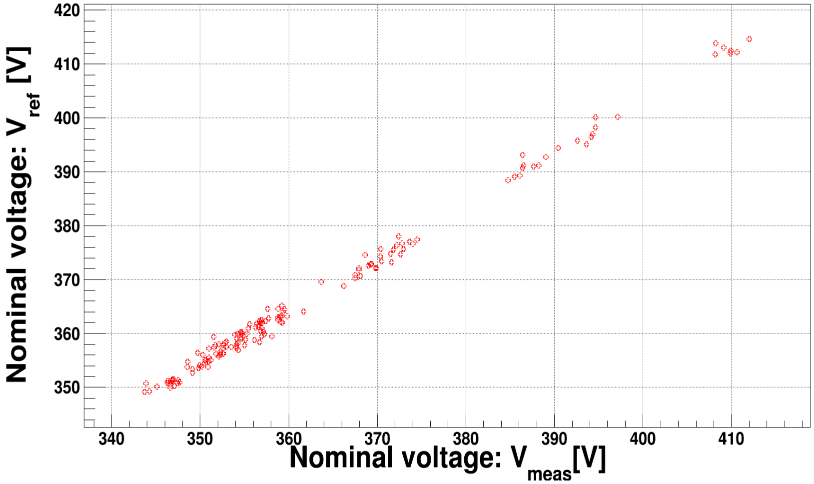

Fig. 8.9: The variance of the nominal voltage given by the manufacturer and the measured value.

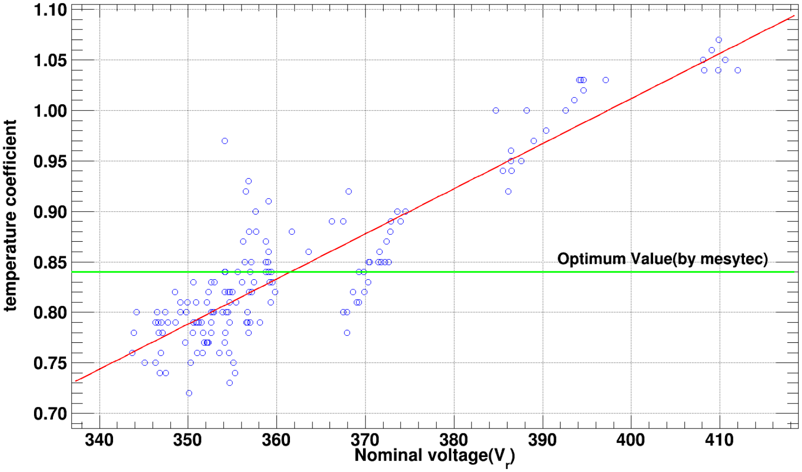

Fig. 8.10: Temperature coefficient versus the nominal voltage of the APDs.

8.4 Outlook

The first version of the quality assurance test stand was designed and its performance is proven. It has the capability to provide controlled temperature for the system within a short time (Δ °C/t = 1.05 °C/s) and keep it with a 0.003 degree precision during the measurement. The stable testing signal is provided by a pulsed LED signal. All procedures are operated automatically.

The system can obtain the important parameters of the APDs: nominal voltage and temperature coefficient. This information will be used in the later experiment. Especially, the temperature coefficient will be used to adjust the gain correction when a deviation of the temperature occurs during the experiment.

This progress is a milestone for the next version. In the future, first, the test program will be upgraded to do more precise measurements. Hamamatsu S12010 series APDs have two active detection areas. The equivalence of both areas has to be proven. The test signal generator will be modified to provide an individual test signal for each detection area. The first version reads a temperature of the testing bench of two APDs, which are placed in both edges of the testing bench. The second version will read all APDs on the test bench.

Second, the structure of the test stand will be modified to increase the number of simultaneously tested APDs. In this step, the size of the test bench will be increased to keep the speed of the controlling temperature.

After these upgrades, the test stand will be a key part to characterize all APDs of the CALIFA barrel and iPhos regions.

A Geant4 simulation

The Geant4 simulation aims to complement the simulation of the thermalized neutron physics done with R3BRoot. The physics models are already included in R3BRoot, but the main target physics of R3BRoot describes the reaction of particles, which have an energy from several tens of MeV up to GeV. The High Precision model (_HP) can be used to cover the low energy neutron physics (below 20 MeV). In addition to these physics lists, a special physics list is defined to achieve a more precise physics process description for thermal neutron energies.

Physics list

In order to achieve a precise physics description, I implemented a cross section data set for thermal scattering and a specific model. The user simply chooses the physics case dependent on the neutron energy (fast or thermal). The following box shows the main part of the physics list:

```
// neutronPhysicsList.cc
//cross sectin data set
 G4NeutronHPThermalScatteringData* dataSet1b =

 new G4NeutronHPThermalScatteringData();

 if(fThermal) process1->AddDataSet(dataSet1b);

// models
 G4NeutronHPThermalScattering* model1b = new G4NeutronHPThermalScattering();

 if (fThermal) model1a->SetMinEnergy(4*eV);

 if (fThermal) process1->RegisterMe(model1b);
```

Primary generator

In Geant4 the primary generator can be one of two different types of configurations; the Primary Generator and the General Particle Source (GPS). The Primary Generator defines the primary event in the source file (e.g. B1PrimaryGeneratorAction.cc in the basic example). The primary particles are then determined in the compile process of the simulation. On the other hand, GPS uses a macro file (e.g. run1.mac) to define the primary particles. So, the primary particles are determined during the execution of the simulation. Specifically, GPS allows to specify the specifications of the spectral, spatial and angular distribution of the primary source particles. It also allows to use the option to define an arbitrary point-wise energy spectrum (see below box). This option is used to simulate the AmBe source. The neutron energy and its intensity are defined in the macro file and the simulation is executed with this macro file.

```
/gps/ene/type Arb
/gps/hist/type arb
#                E (MeV) Rel. Yield

/gps/hist/point    0.11        0.905149
/gps/hist/point    0.33        0.848238
/gps/hist/point    0.54        0.761518
/gps/hist/point    0.75        0.677507
/gps/hist/point    0.97        0.579946
/gps/hist/point    1.18        0.536585
/gps/hist/point    1.40        0.474255
/gps/hist/point    1.61        0.520325
/gps/hist/point    1.82        0.604336
/gps/hist/point    2.04        0.582656
/gps/hist/point    2.25        0.609756
/gps/hist/point    2.47        0.617886
/gps/hist/point    2.68        0.799458
/gps/hist/point    2.90        0.964770
/gps/hist/point    3.11        1.000000
/gps/hist/point    3.32        0.937669
/gps/hist/point    3.54        0.831978
/gps/hist/point    3.75        0.813008
/gps/hist/point    3.97        0.728997
/gps/hist/point    4.18        0.775068
/gps/hist/point    4.39        0.861789
/gps/hist/point    4.61        0.831978
/gps/hist/point    4.82        0.902439
/gps/hist/point    5.04        0.823848
/gps/hist/point    5.25        0.742547
/gps/hist/point    5.47        0.631436
/gps/hist/point    5.68        0.558266
/gps/hist/point    5.89        0.493225
/gps/hist/point    6.11        0.479675
/gps/hist/point    6.32        0.552846
/gps/hist/point    6.54        0.495935
/gps/hist/point    6.75        0.441734
/gps/hist/point    6.96        0.455285
/gps/hist/point    7.18        0.455285
/gps/hist/point    7.39        0.509485
/gps/hist/point    7.61        0.498645
/gps/hist/point    7.82        0.457995
/gps/hist/point    8.03        0.390244
/gps/hist/point    8.25        0.262331
/gps/hist/point    8.46        0.176694
/gps/hist/point    8.68        0.115447
/gps/hist/point    8.89        0.099458
/gps/hist/point    9.11        0.103252
/gps/hist/point    9.32        0.137127
/gps/hist/point    9.53        0.169377
```

```
/gps/hist/point    9.75        0.149593
/gps/hist/point    9.96        0.126829
/gps/hist/point    10.2        0.100271
/gps/hist/point    10.4        0.075338
/gps/hist/point    10.6        0.040921
/gps/hist/point    10.8        0.009837
#
/gps/hist/inter Spline
```

Detector construction

For us the most interesting part is the physics process in the detector. The main goal of this simulation is the thermal neutron capture process in the area of the CALIFA PETAL.
First a simulation with a simple model of a CsI(Tl) crystal was done. In this model the detailed structure of the inside of the CALIFA PETAL is not necessary. The detector is just made of one CsI(Tl) crystal and the outer shape has the same dimension as the CALIFA PETAL. At the starting point of the generated particle a paraffin moderator with the same thickness as in the experiment is placed. The moderator uses the Geant4 material database ("G4_PARAFFIN"), where paraffin is already defined. The same is true for the nickel target, which has the same shape as in the measurement.

Result

The optimum thickness of the polyethylene bricks in the measurement setup is estimated by simulation. I simply changed the thickness of the moderator (detail geometry in Fig. 4.4) and checked the variation of the number of the detected 8.99 MeV gammas and the number of detected all energy gammas (Fig. A.1). According to the reference [Nei77], it needs at least a 10 cm thick moderator to thermalize 1 MeV neutrons. Around 40 % of the emitted neutron energies are lower than 3 MeV and 15 % of the neutron energies are below 1 MeV. On the other hand, the intensity of the detected γ is a negligible value when the moderator is thicker than 10 cm. Moreover, the moderator produces thermal neutrons and reduces the fast neutron energy simultaneously. The fast neutrons are needed for other physics processes. Figure A.2 shows the comparison of the two produced spectra using the different physics list. In the results, it is included the artificial energy resolution $\Delta E/E \approx 0.05$, which corresponds to the experimental result of a single crystal for the 4.44 MeV γ rays. It shows a similar spectrum using both models. The energy spectrum of the user-defined physics list can distinguish more details in the energy levels from 4 to 5 MeV. For energies from 6 to 7 MeV, it is the reverse situation. At energy 8.99 MeV, the same behavior is exhibited in both physics models. But the energy spectrum using the user-defined physics list has less

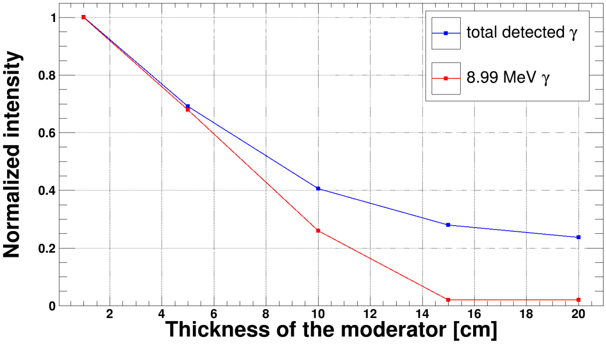

Fig. A.1: The number of detected gamma as a function of thickness of moderator. Blue lined graph shows detected all energy γs and red lined graph shows detected 8.99 MeV γs from thermal neutron capture

background and a higher intensity of the gamma peak.
Figure A.3 presents the dependence on the used targets. For the red-lined spectrum the simulation was done using a moderator and a nickel target. For the blue-lined spectrum only a moderator was used. This simulation aims to distinguish the source of the detected γ-rays. It is compared to experimental data in Chapter 6. In the experimental data many sources can smear out the signal. So it can be used to predict the different gamma energies of the main component of our interest. Based on this result, we can say that the most of the γ rays come from the neutron-induced reactions with the moderator and the scintillator itself. The only γ rays, which originate for neutron capture in the nickel target, are the γ rays with an energy of 8.99 MeV.
The other aim is to get the cross section for thermal neutron capture. The number of emitted gammas from the capture process can then be estimated. For this, I calculated the ratio between the total number of detected γ-rays in the PETAL area and the number of 8.99 MeV γ-rays after background subtraction,

$$\text{ratio} = \frac{\text{Number of 8.99 MeV } \gamma \text{ rays}}{\text{Number of } \gamma \text{ rays in Area}}. \tag{A.1}$$

The ratio obtained in the simulation is $1.348\times10^{-3} \pm 0.052\times10^{-3}$.

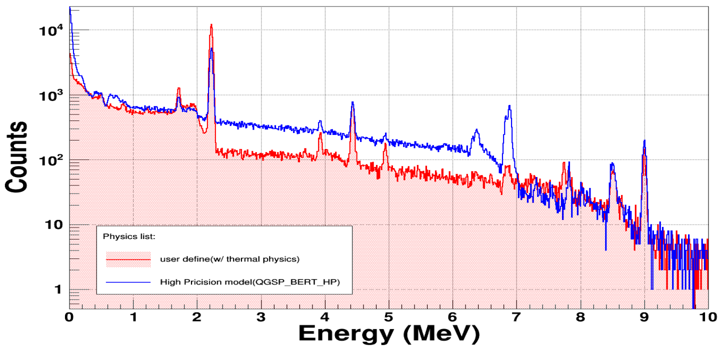

Fig. A.2: Comparison of the spectra produced using different physics lists. The γ-ray energy spectrum caused by neutrons coming from the AmBe source including a nickel target and the paraffin moderator. The red-lined spectrum shows the result using the user defined physics list, and the blue-lined spectrum shows the result using one of the standard Geant4 physics lists (QGSP_BERT_HP).

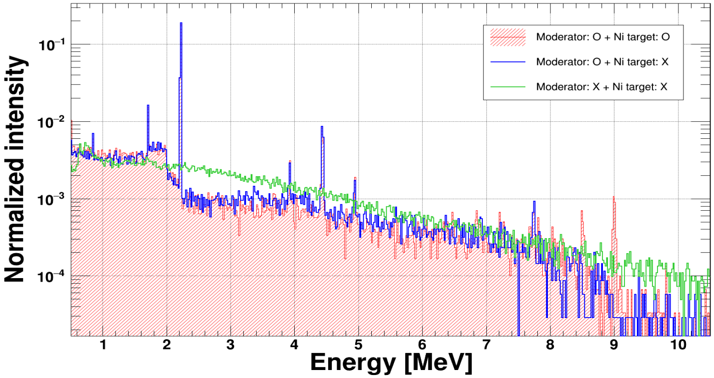

Fig. A.3: Comparison of the spectra produced using different target combinations. The red-lined spectrum shows the result using a nickel target and a moderator, and the blue-lined spectrum shows the result using a moderator without a nickel target. The green-lined spectrum shows the result without both moderator or nickel target.

Bibliography

[Abt+08] I. Abt et al. *Eur. Phys. J. A* 36 (2008), 139.

[Aka+01] E. Akaho et al. *App. Rad. and Iso.* 55 (2001), 175.

[AP+14] H. Alvarez-Pol et al. *Nucl.Instr. and Meth. A* 767 (2014), 453.

[AP11] H. Alvarez-Pol. *Report on CALIFA simulations:response to gammas using the 7.07+7.17 CsI Endcap and Barrel*. 2011. URL: `http://fpsalmon.usc.es/r3b/CALIFA_SimReport_0511.pdf`.

[Aum+14] T. Aumann et al. *Technical Report for the Design, Construction and Commissioning of the Tracking Detectors for* R^3B. Tech. rep. 2014. URL: `https://edms.cern.ch/ui/file/1865815/2/TDR_R3B_TrackingDetectors_public.pdf`.

[BA13] M. Bektasoglu and H. Arslan. *Pram. J Phys.* 80 (2013), 837.

[Bea+94] J. Bea et al. *Nucl. Instr. and Meth. A* 350 (1994), 184.

[Ben+13] M. Bendel et al. *Eur. Phys. J A* 49 (2013), 69.

[Ben10] M. Bendel. “Entwicklung und test einer digitalen Auslese für das CALIFA-Kalorimeter”. Master thesis. TU München, 2010.

[Ber+08] D. Bertini et al. *J. Phys.: Conf. Ser.* 119 (2008), 032011.

[Ber+12] J. Beringer et al. *Phys. Rev. D* 86 (2012), 010001.

[Ber11] D. Bertini. *J. Phys.: Conf. Ser* 331 (2011), 032036.

[Ble15] A. K. Blecher. *High energy calibration of scintillating detectors with thermal neutrons*. Bachelor Thesis, TU Darmstadt. 2015.

[Bor+63] I. Borbely et al. *2.6-MeV neutron-induced reactions in CsI*. Tech. rep. KFKI-1467/f. Hungary, 1963. URL: `https://www.osti.gov/servlets/purl/4008993`.

[BP14] E. Bonnet and M. Parlog. *NFS Workshop, GANIL* (2014).

[Bru+03] R. Brun et al. *Computing in High Energy and Nuclear Physics* (2003).

[Cas+14] E. Casarejos et al. *Eur. Phys. J Web of Conferences* 66 (2014), 11038.

[Che+07] J. Chen et al. *App* 65 (2007), 1318.

[CKR79] F. E. Cecil, K. Killian, and M. Rymes. *Phys. Rev. C* 19 (1979), 2414.

[Coh88] J. Cohen. *Statistical power analysis for the behavioral sciences*. 2nd ed. Hillsdale, NJ: Lawrence Erlbaum Associates., 1988.

[Cro89] S. Croft. *Nucl. Instr. and Meth. A* 281 (1989), 103.

[Eig+06] G. Eigen et al. *Nucl. Instr. and Meth. A* 564 (2006), 144.

[ES98] B. S. Everitt and A. Skrondal. *The Cambridge Dictionary of Statistics*. Cambridge, UK New York: Cambridge University Press, 1998.

[Gas+08] M. Gascon et al. *2008 IEEE Nuclear Science Symposium Conference Record* (2008), 1649.

[Gea13] Geant4collaboration. *Reference Physics Lists*. 2013. URL: `http://geant4.cern.ch/support/proc_mod_catalog/physics_lists/referencePL.shtml`.

[GGL94] A. Georgiev, W. Gast, and R. M. Lieder. *IEEE trans. nucl. sci* 41 (1994), 1116.

[Gro+00] D. Groom et al. *Eur. Phys. J C* 15 (2000), 1.

[HB99] R. C. Haight and C. M. Bartle. *Nucl. Instr. and Meth. A* 422 (1999), 54.

[Hen+01] W. Henning et al. *An International Accelerator Facility for Beams of Ions and Antiprotons*. Conceptual Design Report. GSI, 2001.

[Her16] E. Hergert. *The WITS$ guide to selecting a photodetector*. 2016. URL: `http://www.hamamatsu.com/jp/en/community/optical_sensors/articles/wits/index.html`.

[HLL81] D. A. Harrison, M. A. Lone, and R. A. Leavitt. *Atomic Data and Nuclear Data Tables* 26 (1981), 511.

[HLW07] C. A. Hagmann, D. J. Lange, and D. M. Wright. *Monte Carlo Simulation of Proton-induced Cosmic Ray Cascades in the Atmosphere (UCRL-TR–229452)*. Tech. rep. Lawrence Livermore National Lab. (LLNL), Livermore, CA (United States), 2007. URL: `http://www.llnl.gov/tid/lof/documents/pdf/345183.pdf`.

[Hub82] J. H. Hubbell. *Int. J. Appl. Radiat. Isot.* 33 (1982), 1269.

[Ish+77] A. F. M. Ishaq et al. *Z. Physik A* 281 (1977), 365.

[Jha04] D. K. Jha. *Elements of nuclear reactors*. 1st ed. Discovery Publishing House, New Delhi, 2004.

[JM66] G. Jacob and T. A. J. Maris. *Rev. Mod. Phys.* 38 (1966), 121.

[Jor+94] V. T. Jordanov et al. *Nucl. Instr. and Meth.* 353 (1994), 261.

[Jud63] A. M. Judd. *Nucl. Instr. and Meth.* 23 (1963), 29.

[KB03] J. Kempa and I. M. Brancus. *Nucl. Phys. B* 122 (2003), 279.

[Kle98] K. Kleinknecht. *Detectors for particle radiation*. 2nd ed. Cambridge University press, 1998.

[Kno00] G. F. Knoll. *Radiation Detection and Measurement*. 3rd ed. Wiley, New York, 2000.

[Kra15] M. Krammer. *Scintillators*. 2015. URL: `https://www.hephy.at/fileadmin/user_upload/VO-5-Scintillators.pdf`.

[Kre] D. Kresan. URL: `https://forum.gsi.de/index.php?t=tree&th=4916&start=0&rid=0#page_top`.

[Kur00] N. Kurz. *IEEE Transactions on Nuclear Science* 47 (2000), 336.

[Kur16] N. Kurz. *The General Purpose Data Acquisition System MBS at GSI (and elsewhere)*. 2016. URL: `https://indico.cern.ch/event/617177/attachments/1424870/2185375/mbs-febex.pdf`.

[Leo12] W. R. Leo. *Techniques for Nuclear and Particle Physics Experiments: A How-to Approach*. 2nd ed. Springer-Verlag GmbH, Berlin Heidelberg, 2012.

[Lut13] L. Luts. *Developement of a reconstruction algorithm for γ-ray detection in CALIFA*. Bachelor Thesis, TU Darmstadt. 2013.

[LZT07] L. Lebreton, A. Zimbal, and D. Thomas. *Rad. Prot. Dos.* 126 (2007), 3.

[Lé10] M.-C. Lépy. *Detection efficiency*. 2010. URL: `http://www.nucleide.org/ICRM_GSWG/Training/Efficiency.pdf`.

[Mat+89] T. Matulewicz et al. *Nucl. Instr. and Meth. A* 274 (1989), 501.

[MKF04] A. A. Mowlavi and R. Koohi-Fayegh. *App. Rad. and Iso.* 60 (2004), 959.

[Mos+02] M. Moszynski et al. *IEEE trans. nucl. sci* 49 (2002), 971.

[Mü91] J. W. Müller. *Nucl. Instr. and Meth. A* 301 (1991), 543.

[Nei77] W. J. Neils. *Am. J. Phys* 45 (1977), 443.

[Nes15] C. D. Nesaraja. *Nuclear Data Sheets* 130 (2015), 183.

[Nit] *Thermal Neutron Capture Gammas — Target Nucleus 58Ni*. URL: `https://www-nds.iaea.org/capgam/byn/page062.html`.

[Oli16] M. A. Oliván. “Design, scale-up and characterization of the data acquisition system for the ANAIS dark matter experiment”. PhD thesis. Loughborough University, 2016.

[Pau71] J. M. Paul. *Nucl. Instr. and Meth.* 96 (1971), 539.

[Ph.+04] Ph.Bourgeois et al. *Nucl. Instr. and Meth. A* 518 (2004), 15.

[PHL66] R. W. Powell, C. Y. Ho, and P. E. Liley. *Thermal conductivity of selected metals; National Standard Reference Data System (NSRDS)*. 1966.

[Pie+16] B. Pietras et al. *Nucl. Instr. and Meth. A* 814 (2016), 56.

[R3B11] R3BCollaboration. *Technical Report for the Design, Construction and Commissioning of The CALIFA Barrel:The R3B CALorimeter for In Flight detection of γ rays and high energy charged pArticles*. Tech. rep. 2011. URL: `https://edms.cern.ch/ui/file/1833500/2/TDR_R3B_CALIFA_BARREL_public.pdf`.

[R3B15] R3BCollaboration. *Technical Report for the Design, Construction and Commissioning of the CALIFA Endcap*. Tech. rep. 2015. URL: `https://edms.cern.ch/ui/file/1833748/2/TDR_R3B_CALIFA_ENDCAP_public.pdf`.

[Ram+04] S. Raman et al. *Phys. Rev. C* 70 (2004), 044318.

[Rus+13] I. Rusanov et al. *GSI Scientific Report* FG-CS-04 (2013), 374.

[San14] SantiagoCALIFAgroup. *LAAPD Characterization procedure*. Group report. 2014.

[SH68] J. S. Steinhart and S. R. Hart. *Deep-Sea Research* 15 (1968), 497.

[SJW58] R. S. STOREY, W. JACK, and A. WARD. *Proc. Phys. Soc.* 72 (1958), 1.

[SM01] W. Skulski and M. Momayezia. *Nucl. Instr. and Meth.A* 458 (2001), 759.

[TS08] R. A. Taylor and G. Solbrekken. *IEEE Trans. Components. Packag. Technol* 31 (2008), 23.

[Val+93] J. D. Valentine et al. *Nucl. Instr. and Meth.* 325 (1993), 147.

[Vav57] P. V. Vavilov. *Sov. Phys. JETP* 5 (1957), 749.

[WE14] J. G. Webster and H. Eren. *The Measurement, Instrumentation and Sensors Handbook*. 2nd ed. CRC Press, 2014.

[Zal14] N. J. Zaluzec. *Microsc. Miroanal.* 20 (2014), 1318.

List of Figures

List of Tables

Curriculum vitae

Personal Information

Name: Han-Bum Rhee
Address: Felsingstrasse 5 64285 Darmstadt
Date of Birth: 22. November 1981
Place of Birth: Seoul, Republic of Korea
Nationality: Korean
Marital status: Married

Education

2013- Doctoral student in physics

Technische Universität Darmstadt, Germany
Supervisor: Prof. Dr. Thorsten Kröll

2007 - 2010 Master student in physics

Korea University, Seoul, Republic of Korea
Degree: Master of Science
Title of master thesis: "Assembly and installation of RE 1/1 for CMS/LHC"
Supervisor: Byungsik Hong

2001 - 2007 Bachelor student in physics

Catholic University of Korea, Seoul, Republic of Korea
Degree: Bachelor of Science

1997 - 1999 High school

Dongsung High School, Seoul, Republic of korea

1994 - 1996 Middle school

Samsun Middle School, Seoul, Republic of Korea

1988 - 1993 Elementary school
Donam Elementary School, Seoul, Republic of Korea

Military service

June 2002 - July 2004

Employment

April, 2010-March, 2011 Intern researcher
Department of Physics, Korea University, Seoul, Republic of Korea

Publication

- H.C.Kim, S.Y. Bahk, B. Hong, S.J. Hong, R.J.Hu, M.H. Jo, C. Kim, Y.J. Kim, Y.U. Kim, K.S. Lee, S.J. Lee, S.J. Lee, S.K. Nam, S.K. Park, H.B. Rhee, J.T. Rhee and K.S. Sim, *Quantitative aging study with intense irradiation test for the CMS forward RPCs*, Nucl. Instr. Meth. A, 602, 771
- S.Park et al., *Development of RE1/1 RPCs for the CMS muon trigger system*, Nucl. Instr. Meth. A, 602, 665
- Kyoung Sei Lee, Byungsik Hong, Sung Keun Park, Han-Bum Rhee and Kwang-Souk Sim, *Monte-Carlo Simulations for Proton-beam-induced Prompt Radiations in Biological Tissue*, J Korean Phys. Soc.58,15